Methods of characterising the process of early biomineralisation

by

Adam John Anthony McGuinness

A thesis submitted to the University of Birmingham for the degree of

DOCTOR OF PHILOSOPHY WITH INTEGRATED STUDIES

School of Chemistry

College of Engineering and Physical Sciences

University of Birmingham

April 2023

Abstract

Mature bone is a highly ordered structure composed of hydroxyapatite crystals uniformly arranged within regularly spaced fibrils of collagen, populated with several cell types. This arrangement produces a material with a unique combination of strength and resistance to fracture, as well as the ability to remodel, repair and regenerate in response to injury or changing load. Intrafibrillar mineralisation present in mature bone is a thermodynamically unfavourable process, suggesting highly controlled processes during early mineralisation, current knowledge of which is poorly understood. Evidence suggests extracellular vesicles (EVs) are involved in this early mineralisation process, potentially acting as a nucleating and stabilising agent in mineralisation, but the heterogeneity and poor characterisation of these nanoparticles limits the understanding of their role.

Whilst the heterogeneity of EVs as a population is unquestioned, identification of the presence or absence of subgroups within these populations has not been adequately investigated. Interrogation of individual EVs would allow the construction of a highly resolved map of EV characteristics. Collecting this data is the first step in identifying distinct populations within the EV secretome. From there, identification of the impact of these distinct populations and their attendant molecular characteristics, upon mineralisation would be a significant boost to therapeutic treatments for mineralisation abnormalities, such as osteoporosis, non-union fractures, and heterotopic ossification.

This thesis investigates new techniques for investigating the biochemical and physical characterisation of EVs, as well as the early mineralisation stages of osteoblast like cells, and the role of EVs therein. Here we apply the methods of x ray fluorescence (XRF), Raman spectroscopy and transmission electron microscopy (TEM) to mineralising cell cultures and EVs to elucidate the processes and characteristics of the early mineralisation process.

We utilise XRF to detect the presence of elemental ions in control compounds, with signal strength reliably corresponding to the proportion of elements present. When applied to mineralising cell cultures, a changing elemental composition across time

points is observed. We have documented the presence of a calcium deficient, phosphorous dense material in early mineralisation, maturing towards an increased calcium presence in later time points. This suggests intermediate mineral phases are present in mineralising bone prior to the hydroxyapatite present in mature tissue. XRF was also used to quantify characteristics of mineralising cell culture, using automated image analysis to identify mineral nodule number and size, and observe the rapid mineralisation induced by coculture of osteoblasts with EVs.

In addition to these results, we have shown the correlation of Raman signal with the mineral content of bone, making it another potentially useful tool in the investigation of mineralisation. Attempts to incorporate molecular tweezers with Raman spectroscopy for the characterisation of individual osteoblast EVs were ultimately unsuccessful, however, lessons were identified for future application of both techniques.

Finally, improvements to current TEM techniques of EV imaging were demonstrated in this thesis, using gold nanoparticles to label exosome associated surface proteins, and a methylcellulose supporting film to maintain a spherical morphology.

The findings presented here offer insight into the early mineralisation process, as well as developing techniques to explore these findings further. Clarification of potential intermediate mineral stages can be further explored using the XRF and Raman spectroscopy techniques developed in this manuscript. The TEM protocols developed here may provide a more physiological insight into EVs, whilst the labelling process can be used to identify the presence of specific proteins. Automated imaging analysis techniques may be useful for high throughput imaging systems, identifying the impact of drugs or changes in conditions (e.g. hypoxia) upon mineralisation progression. Together, these techniques and results contribute to the current and future understanding of early mineralisation and may one day be exploited to improve medical outcomes for implants, cements, and diseases such as osteogenesis imperfecta.

Acknowledgements

Enormous thanks to Professor Liam Grover for his guidance, seemingly endless knowledge, and ability to find the interesting in everything. Additional thanks to Professor Andrew Devitt for giving me the opportunity to nurture a fledgling desire for research and lab work as an average undergraduate student at Aston University. Also, to Dr Zania Stamataki, for the infectious enthusiasm, knowledge and support.

My colleagues at the University of Birmingham who have helped and contributed in some way to my research, Mathieu Brunet, Sophie Louth, Ioannis Azoidis, Emma Buchan, Dr Meg Cooke, Emma Lardner, and anyone else who I may have forgotten.

The Sci-Phy cohort, for teaching me, making me laugh, and making this journey much less lonely.

Finally, and most importantly, my family, and their unlimited confidence in me. Kirthi, without whom I would be absolutely unable to do any of this, you are as patient as a saint and as wise as an extremely wise thing, I'll never be able to thank you enough. The little man, impending little man and the dog, the cause of, and solution to, all of life's problems. My mom and dad, who's love and support for me allowed me to grow into who I am today, and for which, I am very fortunate, and very grateful. To nan, other nan, grandad, my brothers, and the rest of my family, I hope I've made you proud.

You all can take some of the credit for this work, not all, but some of it.

Contents

List of Figures

List of Tables

Abbreviations

2D – Two-dimensional

3D – Three-dimensional

ACC – Amorphous calcium carbonate

ACP – Amorphous calcium phosphate

ADP – Adenosine diphosphate

AMP – Adenosine monophosphate

ATP – Adenosine triphosphate

ALPL – Alkaline phosphatase

AR – Alizarin red

A.U. – Arbitrary units

BSP – Bone sialoprotein

βTCP – Beta tricalcium phosphate

Ca Pyro – Calcium pyrophosphate

CaP – Calcium phosphate

CAT – Colloid assembly and transformation process

Col1A1/2 – Collagen type 1/2

CRISPR - Clustered regularly interspaced short palindromic repeats

CSF1 - Colony stimulating factor 1

DCPD – Dibasic calcium phosphate dihydrate

DLS – Dynamic light scattering

Dlx5 - Distal-less homeobox 5

DMP1 – Dentin matrix protein 1

DSPP – Dentin sialophosphoprotein

ECM – Extracellular matrix

ENPP1 - Ectonucleotide pyrophosphatase phosphodiesterase-1

EV – Extracellular vesicle

FGF23 – Fibroblast growth factor 23

GAG – Glycosylated group precipitation kit

HA – Hydroxyapatite

HDF – Human dermal fibroblasts

HSC – Hematopoietic stem cell

IFITM5 – Interferon induced transmembrane protein 5

INV – Polymer precipitation kit

kDa – kilodaltons

LC-MS/MS - Liquid chromatography mass spectrometry

MCPM – Monocalcium phosphate monohydrate

MEPE – Matrix extracellular phosphoglycoprotein

MHC I/II – Major histocompatibility complex class I/II

miRNA – micro ribonucleic acids

MiV – Micro vesicles

MPa - Megapascal

MSC – Mesenchymal stem cell

MV – Matrix vesicles

µXRF – Benchtop micro X-ray fluorescence

Na Poly – Sodium polyphosphate

OCN – Osteocalcin

OCP – Octacalcium phosphate

OPN – Osteopontin

Osx - Osterix

Pi – Inorganic phosphate

PILP – Polymer induced liquid precursor process

PTH – Parathyroid hormone

PolyAsp – Polyaspartic acid

PO_4 – Phosphate ion

PolyP - Polyphosphates

PPi – Pyrophosphate

RANKL – Rank ligand

RNA – Ribonucleic acid

Runx2 - Runt-related transcription factor 2

SEC – Size exclusion chromatography

SERPINF1 - Serpin Family F Member 1

SIBLING - Small integrin-binding ligand N-glycosylation

TNAP – Tissue nonspecific alkaline phosphatase

TRACP5b - Tartrate-resistant acid phosphatase

UC – Ultracentrifugation

XRF – X-ray fluorescence

Chapter 1 : Literature Review

1.1 Introduction

Human bone is a complex, living tissue that displays exceptional physical properties due to its unique composite structure, consisting of an organic component (largely collagen), and an inorganic component (largely hydroxyapatite). Individually, these two components are soft (collagen) or brittle (hydroxyapatite), however, when combined in the hierarchical structures seen in bone, can withstand compressive forces greater than concrete (100−150 MPa), whilst simultaneously displaying a resistance to flexural forces greater than some plastics (135−193 MPa) [1,2]. These properties make bone an effective structural material for the loads encountered by the human body, however they are arguably not the most impressive feature of bone as a structural material. This belongs to the ability of bone to undergo constant remodelling, regeneration, and repair throughout a lifetime, thanks to the living cell populations that exist within this remarkable organ (see Section 1.3: Bone Cells).

Whilst the self-repair ability of bone is impressive, it is limited. Significant trauma from injury or implants for structural repair may overcome the self-healing ability of resident tissue. This can be due to a loss of bone tissue and accompanying cellular machinery, resulting in an injury too large to be closed, or by pathogenic or opportunistic organism infection, inhibiting the function of the bone resident cells in their repair attempts. Dysfunction of the repair process at this macro scale is an increasing issue as populations age, particularly when combined with increasing likelihood of age-related osteoporosis.

Dysfunction in the formation of bone at the microstructural level can lead to a reduced ability of the bone to withstand these compressive and flexural forces, resulting in tremendous health issues, the classic example of this is osteogenesis imperfecta. This potentially fatal disease can be caused by autosomal mutations in type 1 collagen genes *COL1A1/COL1A2*, or mineralisation pathway involved *SERPINF1* or *IFITM5* genes, leading to weakened collagen or disordered mineralisation [3]. These mutations can result in skeletal deformity and weakness, membrane ossification, disordered tooth development, and in severe cases, perinatal death. Understanding the fundamental

processes behind early mineralisation may in turn inspire new treatments for such debilitating conditions.

Despite the clear importance of the microstructure of collagen and hydroxyapatite composite that makes up the majority of bone, it is only recently that these relationships are becoming well understood. The intrafibrillar mineralisation of collagen is vital to the remarkable mechanical properties of bone, the resistance to compression but brittle nature of the ceramic hydroxyapatite (HA) crystals is mitigated by the flexibility and load sharing ability of the collagen matrix. This method of mineralisation is however, a thermodynamically unfavourable reaction. Placing type 1 collagen fibres into a solution containing high concentrations of calcium and phosphate will not result in intrafibrillar mineralisation. Instead, mineral crystals form on the external surface of the fibre [4], forming irregularly shaped crystals with large variance in size and alignment. The highly regular size and order of HA crystals found in bone indicates there are undefined processes at work to enable these critical characteristics. There is extensive speculation on the processes involved in intrafibrillar mineralisation, with convincing theories suggesting the involvement of stabilising molecules [5]. Theories regarding the formation of the micro structuring of bone remain unproven and are the focus of significant ongoing research.

The discovery of nano sized nucleating particles in mineralised cartilage by Anderson in 1967 [6] led to the implication of matrix vesicles in early mineralisation, although this theory was controversial. The subsequent discovery in these matrix vesicle (MV) sites of proteins and membrane lipids common across extracellular vesicles (EVs) [7,8], may point to the involvement of EVs in the mineralisation process.

Though initially discovered in 1967 [6,9,10], EV research has undergone an extraordinary explosion in popularity in the last decade, as displayed in Figure 1.1. This increase in research publication coincides with increased interest in the involvement of EVs in tissue homeostasis, therapeutic potential, and in disease states such as cancer and autoimmune disease [11].

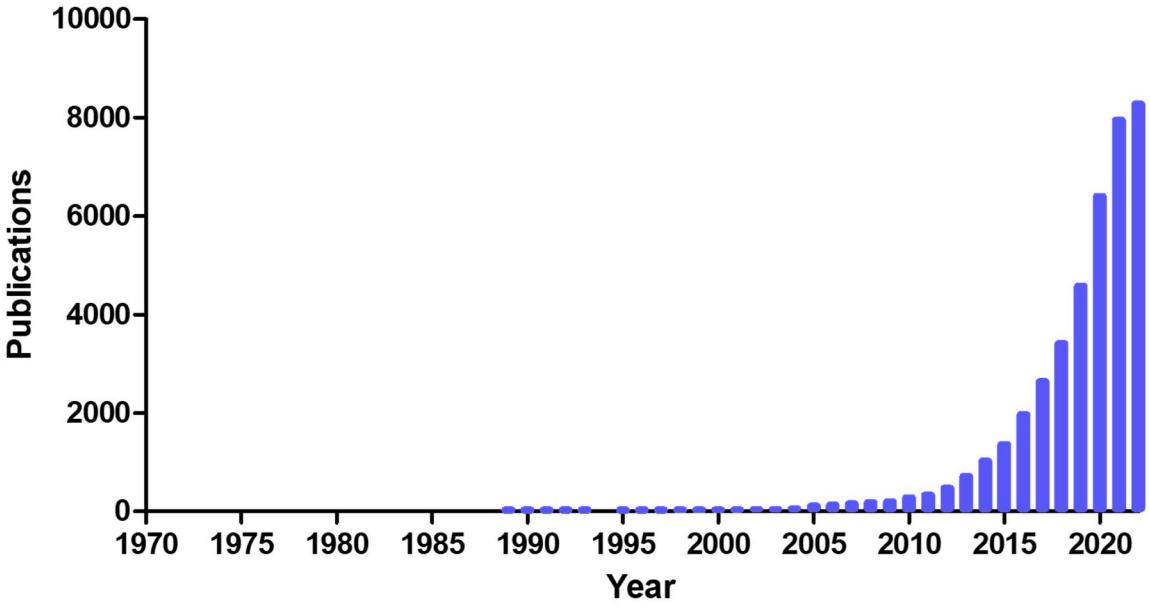

Figure 1.1: Publication trend for extracellular vesicles. Data obtained from PubMed using the criteria: "extracellular vesicles" or “exosomes” and publication date 1900/01/01-2022/12/31. Search performed 10/03/2023.

This explosion of research has been fuelled by the emergence of new technologies, and refinement of currently existing ones, permitting further detailed characterisation of EVs, previously limited due to the nano sizing of these particles. This thesis uses these technologies to build upon previous research and expand the field of knowledge surrounding the involvement of EVs in the early mineralisation processes in bone. It is hoped that the knowledge uncovered in these pages may in future contribute in some way towards the treatment of bone repair and dysfunction at the macro and micro structural level.

1.2 Functions of bone

Bone is a vital organ in the homeostasis of the human body. Whilst its importance in structure and support is obvious, less obvious is its essential role as a store of calcium and other minerals, as well as generation of new blood cells.

1.2.1 Protection

One of the more obvious roles of bone is the protection of organs that require a less rigid composition to function. An example of this would be the protection offered by the skull, to the brain within. The skull is capable of resisting forces between 340-6400 N depending on area of impact, far greater than the brain would be capable of resisting alone [12]. In addition to protecting the brain, bone also protects the lungs and heart via the ribcage, vertebrae provide protection to the spinal column, the pelvis to digestive and reproductive organs, and the long bones provide protection to bone marrow cells.

1.2.2 Support and movement

Bone provides attachment points for a multitude of organs, maintaining their position relative to each other, thus allowing proper function. The anchor points on bone for musculature permit movement of limbs via the specific structures of joints, whilst attachments for facial muscles permit communication both verbally and non-verbally. Alongside these functions, the cellular contingent within bone has the tremendous remodelling ability, adapting the structure of bone to changes in load and self-repair after injury.

1.2.3 Mineral storage

The skeletal system contains a vast reservoir of the minerals essential to homeostasis. Bones contain 99% of the calcium, 90% of the phosphate, 70-80% of the carbonate as well as significant proportions of the sodium and magnesium in the body [13]. These ions can be mobilised from storage by the actions of the endocrine system, in particular parathyroid hormone. This hormone stimulates one of the cell types involved in bone remodelling (osteoclasts, discussed later) to break down and digest bone tissue, by secreting acids and proteases onto the mineralised tissues, freeing calcium and phosphate ions for transportation and use elsewhere.

Phosphate plays a key role in the human body, it is essential in the formation of key biological structures, energy storage and transfer, signalling, and other fundamental biological functions. Structurally, phosphates (along with ribose sugars) form the backbone of the DNA and RNA helixes, as well as being a key component of the phospholipid bilayer that forms cell membranes. Phosphate groups are also a critical part of ATP (adenosine triphosphate), and the phosphorylation and dephosphorylation of molecules, forms the basis for energy transfer and metabolism within living cells. Phosphorylation and dephosphorylation of enzymes and other molecules are key processes in signalling pathways, including those regulating cell growth, migration, apoptosis (programmed cell death), endocytosis, and differentiation. The addition or removal of phosphate groups will often cause a conformational or electrostatic change, and is a key step in the activation or deactivation of most enzymes and receptors.

Levels of phosphate within the body are closely regulated by feedback loops across multiple organs, known as the parathyroid-kidney-intestine-bone axis. Parathyroid glands produce parathyroid hormone (PTH) in response to low calcium levels in the blood. Increased levels of PTH in the circulation results in upregulated osteoclast activity, and subsequent dissolution of bone mineral, resulting in calcium and phosphate ion release into the blood supply. Within the kidneys, PTH has the effect of increasing calcium ion reabsorption, whilst increasing phosphorous excretion, having an effect of reducing phosphate within the blood. In addition, PTH indirectly stimulates the synthesis of active vitamin D (calcitriol), a hormone that increases calcium and phosphorous absorption by the small intestine. Calcitriol completes the cycle by acting on the parathyroid glands to increase calcium sensor expression, and supress transcription of the gene responsible for PTH production. This cycle is complemented by fibroblast growth factor 23 (FGF23). Released by osteocytes, osteoblasts and osteoclasts when blood phosphate and calcitriol are increased, FGF23 activity reduces serum phosphate by decreasing phosphate reabsorption in the kidney and inhibiting calcitriol production. [14] Working in tandem, PTH and FGF23 play a significant and finely balanced role as part of the parathyroid-kidney-intestine-bone axis, maintaining the homeostasis of calcium and phosphate levels in the blood.

The tight regulation of phosphate and calcium described here is critical due to its involvement in a wide variety of vital cellular processes, and the need to maintain overall mineral balance and bone health. Understanding this regulation is crucial in order to treat various metabolic disorders and diseases related to bone density and mineralisation.

1.2.4 Blood cell production (haematopoiesis)

The bodies population of blood cells consists of a multitude of cell types, many with very short half-lives requiring constant replenishment. It is estimated that a healthy person replaces 100 billion cells daily, in a process called haematopoiesis. In this system, haematopoietic stem cells (HSCs) are encouraged to differentiate into monocytes, neutrophils, B cells, T cells, basophils, eosinophils, platelets, and red blood cells by cocktails of cytokines and growth factors attuned to the requirements of the body at that time. The HSC population is resident within the skeletal system, found inside the long bones, pelvis, breastbone, and spinal column.

1.3 Bone cells

The bone is an active, constantly remodelled organ, reacting to changes in load, endocrine influence, and injury. This remodelling capacity is provided by a synergistic interplay between the cell lineages that reside within and upon its surface. Here, we discuss the primary cells involved in this remodelling process.

1.3.1 Mesenchymal stem cells

Mesenchymal stem cells (MSCs) are pluripotent cells, that is, able to differentiate into multiple cell types, including osteoblasts, adipocytes and chondrocytes and are resident in the bone marrow. For an MSC to differentiate, specific genes are activated or deactivated in a tightly temporally controlled manner, those key in osteoblastogenesis include Runt-related transcription factor 2 (*Runx2*), Distal-less homeobox 5 (*Dlx5*) and Osterix (*Osx*). These genes in turn activate downstream pathways that upregulate osteoblast activity related genes, increasing production of collagen 1 (Col1A1) and alkaline phosphatase (ALPL) proteins, amongst others [15].

1.3.2 Osteoblasts

Osteoblasts are the principal cell involved in the deposition of bone. Beginning with matrix synthesis, osteoblasts secrete collagen, osteocalcin (OCN), osteopontin (OPN) and other non-collagenous proteins into the extracellular space. The collagen these cells produce will form the organic scaffold upon which the non-collagenous proteins are believed to encourage mineral formation, resulting in new bone formation.

1.3.3 Osteoclasts

Osteoclasts are multinucleate cells which differentiate from the monocyte/macrophage lineage via activation of the RANK Ligand (RANKL) and colony stimulating factor 1 (CSF1) pathways [16,17]. Primarily responsible for digesting and subsequent resorption of bone, this is done by attachment of the osteoclast to the bone surface, formation of a sealed compartment, and secretion of hydrogen ions [18] to acidify this compartment and subsequently dissolve HA. Acid resistant enzymes such as tartrate-resistant acid phosphatase (TRACP5b) are also released to break down the organic component of bone. Communication and competition with osteoblasts form the basis of the remodelling process of bone [19].

1.3.4 Osteocytes

Osteocytes are derived from osteoblasts and are the most numerous cell type within bone. They are found within mineralised bone, enclosed within small niches with multiple extending dendritic processes that spread throughout an interconnecting network of canaliculi. It is believed that osteocytes can detect mechanical signals such as loading and unloading of the bone, and can signal, via the canaliculi, other osteocytes and even osteoblasts on the surface of the bone, inducing modulation of mineral in response to physical load [20,21].

1.4 Bone structure

As previously mentioned, human bone is predominantly formed from aligned, ordered HA crystals, organised regularly within the intrafibrillar spaces of collagen fibres. These 300 nm fibres are ordered in 67 nm intervals, with non-reducible bonds between [22], into micrometre sized fibres which are in turn assembled into bundles called lamellae. These lamellae, grouped together, form an osteon, a cylindrical structure 100-200 µm in diameter, through the centre of which runs the haversian canal, providing the blood supply for the osteon unit (see Figure 1.2).

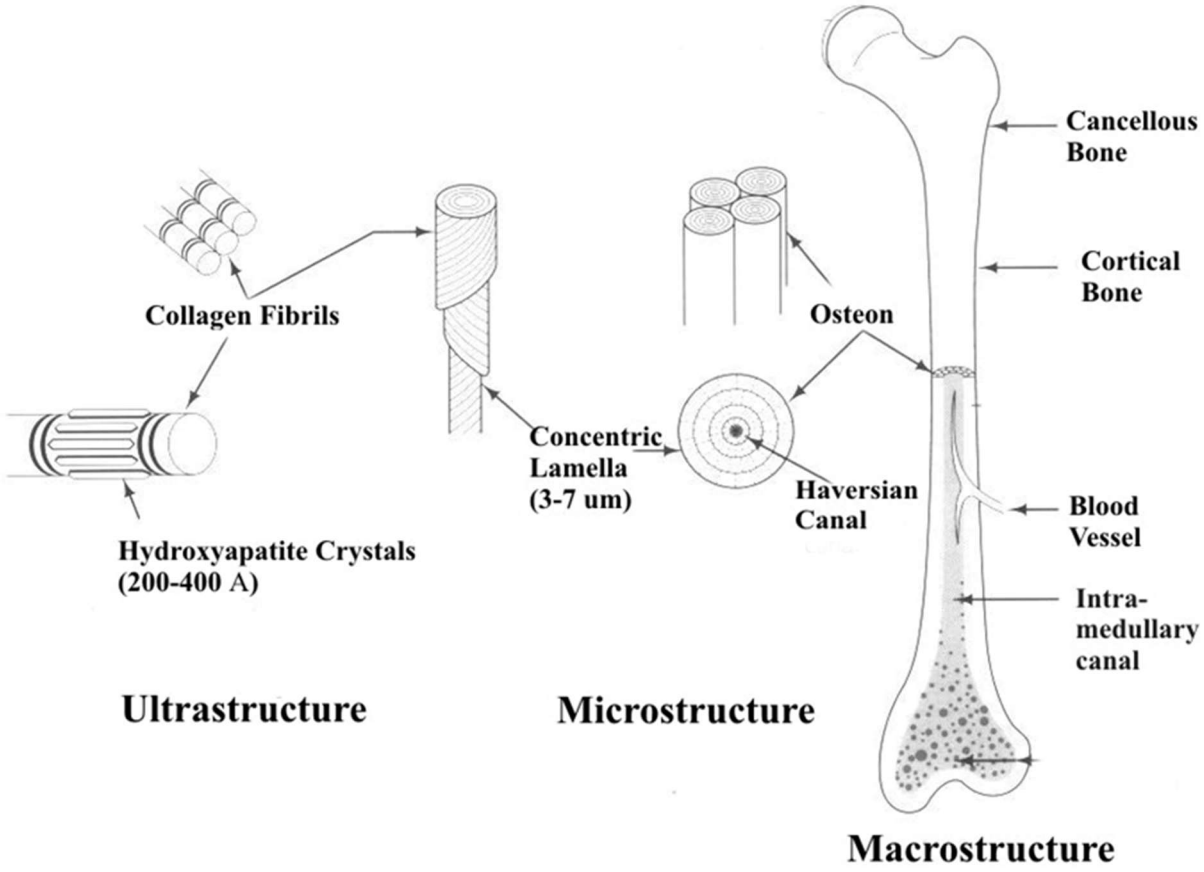

Figure 1.2: Diagram displaying the hierarchical structure of bone from the ultrastructure to macrostructure. Hydroxyapatite crystals form within collagen fibres, which are grouped into fibrils, organised into concentric lamella, formed around a haversian canal in a structure called an osteon. Multiple osteons form the macrostructure of cortical bone. Image reproduced from Tencer and Johnson, 1994 [23].

1.5 Types of bone

1.5.1 Cortical bone

Cortical bone is typically much denser than cancellous bone and found predominantly in areas of the skeleton that tend to bear load in a single plane. This type of bone consists of tightly packed osteons aligned in the direction of force transfer, offering a significant resistance to compression vital in the long bones. This polarity results in a strength in the loading direction, but weakness in the transverse direction. Blood supply to cortical bone runs through the Haversian canals and connecting Volkmann's canals.

1.5.2 Cancellous bone

Cancellous bone is typically less dense, and as a result lighter but less resistant to load. It is typically found in areas that are not loaded from a singular direction, such as the skull and vertebrae. It is formed from interconnecting thin struts, named trabeculae, that are not highly ordered in their directionality like osteons in cortical bone. This open structure allows it to be more metabolically active, housing bone marrow, thus playing a key role in haematopoiesis.

1.6 Bone development

1.6.1 Long bone development

The formation of long bone occurs primarily through the process of endochondral mineralisation. This process begins with the differentiation of MSCs into chondrocytes in the embryonic limb bud, which form a largely cartilaginous structure called the growth plate. Cycles of proliferation, hypertrophy, maturation and apoptosis of the chondrocytes leave a structure of collagen, which is subsequently mineralised by osteoblasts, creating an elongated bone structure, found in long bones such as the femur and tibia. [24]

1.6.2 Flat bone development

Flat bones, such as the skull, are formed via an alternative method, known as intramembranous ossification. During this method, MSCs form localised clusters and subsequently differentiate, some into endothelial cells, and others into osteoblasts. The endothelial cell population form capillaries, whilst the osteoblasts migrate out from the MSC clusters, secrete collagen, and ultimately, mineralise this collagenous framework to form the large, flat bones that form the skull and pelvis.[25]

1.6.3 Chemistry of bone formation

The formation of human bone is not yet fully understood. It is known that bone is structured hierarchically at the nano and macro scales, suggesting that biological construction is tightly controlled. This begins with osteoid structure formation from extracellular matrix proteins, mainly collagen type 1. Mineralisation of this structure by HA crystals increases its strength, leading to the formation of mature bone, this exact mechanism of HA deposition is still debated [26].

1.6.4 Transition from amorphous to crystalline HA

Hydroxyapatite formation has been replicated *in vitro* using high concentrations of calcium and phosphorous ions, which encourages the formation of amorphous calcium carbonate and phosphate globules (ACC and ACP respectively) [27]. These unstable globules can then transform to the more thermodynamically stable crystalline HA [28], the mechanism for which is still debated, but may occur in a step wise formation from Posner's clusters [29]. In mature bone, thin, aligned plates of HA are present within

collagen fibrils, producing a rigid, strong structure of mineralised collagen [30] (see Figure 1.3). This relationship between the small, stiff crystalline elements, and softer matrix results in a hierarchical, composite material with significantly greater ability to withstand fracture and deformation than either element individually. Gupta, *et al.* [31] suggest that the fracture strain of apatite alone is half that of bone, likely due to defect insensitivity and load sharing between subunits in the hierarchical formation that is bone *in vivo*.

The relationship between amorphous calcium phases and rigid, crystalline HA remains unclear, some posit that this may occur in a single step [32,33] . These *in vitro* findings, however, occurred in tightly controlled conditions, not representative of the wider milieu of biological components present *in vivo*.

Other evidence may suggest that intermediate phases of calcium phosphates are involved, such as dibasic calcium phosphate dihydrate ($CaHPO_4 \cdot 2H_2O$, DCPD), also known as brushite, and octacalcium triphosphate ($Ca_8(HPO_4)_2(PO_4)_4 \cdot 5H_2O$, OCP) [34,35]. More recent TEM studies of biological bone by Xin, Leng and Wang [36] have detected structures consistent with the presence of OCP, whilst Raman spectroscopy of *in vivo* murine calvarial tissue performed by Crane *et al* also detected the presence of OCP in fracture repair [37]. These studies may point to the involvement of multiple phases of calcium phosphate containing compounds.

1.6.5 Biological composition of mineralised bone

Biological bone mineral is not 100% HA, the Ca^{2+} ion is commonly substituted with alternative cations, such as MG^{2+} and Na^{+}, additionally, carbonate ions CO_3^{2-} may be substituted in place of phosphate (PO_4) or hydroxyl groups. These substitutions have been shown to have a significant impact upon the crystallinity, morphology and solubility of bone mineral, which can have an effect upon the biological properties displayed. These substitutions are more pronounced in certain diseases, commonly resulting in altered crystal sizes, potentially affecting properties such as fracture resistance.[38]

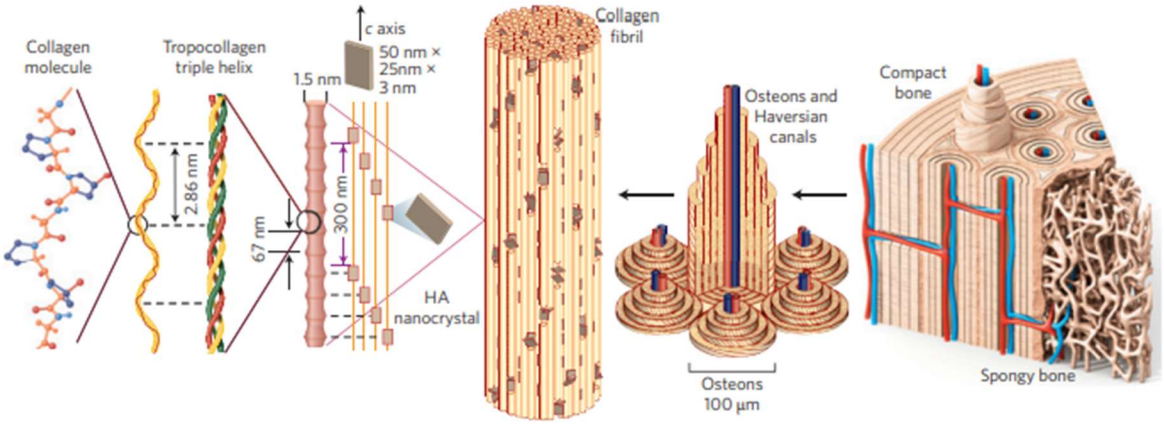

Figure 1.3: Diagram displaying relative sizes of the structures involved in the various structures of bone from the nano to the macro scale. Nano sized collagen molecules form a triple helix collagen fibre, highly structured organisation of these fibres form fibrils with regular HA crystal incorporation are organised into osteons of approximately 100-300 µm in size. Reproduced from Wegst *et al*. 2014 [39].

1.6.6 How does intrafibrillar mineralisation occur?

Placing type 1 collagen fibres into supersaturated calcium and phosphate solutions *in vitro* does not produce intrafibrillar mineralisation, instead causing mineral crystallisation on the surface of the fibres [4], suggesting the presence of additional modulating factors *in vivo*. Research suggests that including negatively charged or acidic molecules can induce intrafibrillar mineralisation in the presence of calcium and phosphate. It is theorised that these acidic and phosphorylated residues act to stabilise the amorphous molecules, inhibiting crystallisation, this allows the amorphous stages to enter between collagen subunits, perhaps by capillary action [40,41]. Within these intrafibrillar gaps, which exclude proteins larger than 40 kDa [42], the absence of these inhibitors permits crystallisation, spatially directed and oriented by the confines and charges of these gaps, resulting in the crystal polarity we see in bone *in vivo*. This process was initially termed the polymer-induced liquid precursor (PILP) process [43], which has recently been updated to the colloid assembly and transformation (CAT) process [5], acknowledging that the precursor molecules are not liquid, but more likely have a remnant colloidal or nanogranular texture [44]. It must be noted, however, that the above colloidal infiltration theory is based upon optical investigation of $CaCO_3$ mineralisation, and not calcium phosphate (CaP) precursors, which, due to their insolubility and smaller size, cannot be investigated in the same way. Having said this, the similarity of the intrafibrillar outcomes from both $CaCO_3$ and CaP in the presence of polyAspartic acid (pAsp) [45], may suggest that similar processes are occurring.

1.6.7 Roles of non-collagenous proteins in the CAT process

The requirement of a nucleating or stabilising molecule has become clear in the process of intrafibrillar mineralisation, and it appears that many molecules can take on this role in the process. There have been multiple papers published highlighting different molecules, such as pAsp [40,46,47], polycarboxylic acid [48], polyacryilic acid [49], and orthosilic acid [50]. These molecules are unlikely to play a role *in vivo*, but more complex, non-collagenous proteins with similar negatively charged areas have also shown the ability to stabilise ACP, these include dentin matrix protein 1 (DMP1) [51], osteopontin [52,53], osteocalcin [54] and fetuin A [42,55]. These proteins are commonly associated with bone and/or dentin, and, in the case of DMP1 [56] and osteopontin [57], bound directly to collagen, supporting their potential importance in the early mineral formation

processes. It is perhaps unsurprising that several patents exist for bioengineered recombinant proteins that mimic these organic proteins, in an effort to manufacture mineralised collagen on a larger scale [58–60].

1.6.8 Practical usage of intrafibrillar mineralisation

The PILP/CAT process has since been used to successfully promote mineralisation *in vivo*. Wang *et al*. [61] adapted Gower's PILP process, mineralising wet collagen scaffolds and utilising the protein carboxymethyl chitosan as an ACP stabilising agent. Collagen scaffolds mineralised in this manner showed reduced mechanical weakness and rapid degradation that currently reduce the *in vivo* usefulness of unmineralized or non-stabilised mineralised collagen. These scaffolds also showed improved cellular proliferation during cell culture, possibly due to the additional rigidity maintaining pore openings and therefore greater surface area for cell adhesion. Once implanted into critical defects in non-load bearing areas of rat calvaria, the CAT mineralised collagen resulted in markedly increased bone formation within 4 weeks, and displaying osteoid and capillary formation at 8 weeks. Further work by the same group [62] suggests that careful manipulation of the stiffness of these biomimetic collagen membranes can induce differentiation of mesenchymal stem cells towards an osteogenic phenotype.

1.7 Are extracellular vesicles involved in bone mineralisation?

The concentration of phosphate and calcium ions necessary for collagen mineralisation has been linked to the presence of matrix bound nanoparticles, initially identified using transmission electron microscopy as electron dense regions in cartilaginous matrix. [6,10]. These particles, typically around 300nm or less, are described as matrix vesicles (MVs), and are thought to play an important role as nucleation sites for the deposition of ACP, and subsequent endochondral bone formation.

More recently, these MVs have been shown to share common proteins and membrane lipids [63] with another group of nano-sized vesicles, termed extracellular vesicles (EVs), suggesting EVs and MVs are intrinsically linked.

1.7.1 Extracellular vesicles

The term EV covers a heterogeneous population of phospholipid enclosed, nano-sized particles, and have been found to be released by almost all cell types. EVs have been shown to contain proteins and ribonucleic acids (RNA) [64–66], there is evidence that EVs are able to act as messengers and transfer these molecules between cells [67–69], pointing to a role in cellular communication. Initially discovered in 1967 from platelet derived plasma [9] and termed platelet dust, EVs are now known to be ubiquitous within the body [70–72] with many varied roles, dependent upon the cellular source and environment. EVs are a promising avenue of research in several disciplines, in recent years their potential to drive regenerative therapies is being explored in various fields such as oxidative stress [73], regenerative medicine [74,75], respiratory medicine [76,77] and angiogenesis [78] to name a few.

EVs are typically divided into three classes, based on biogenesis (Table 1.1). Exosomes, between 30-150 nm in size, are formed within multivesicular bodies in the cell cytoplasm, and released via fusion with the outer plasma membrane. In contrast, microvesicles (50-1000 nm) are formed through budding of the cell plasma membrane, whilst apoptotic bodies (500-2000 nm) form via blebbing of apoptotic cell surfaces.

1.7.2 Matrix vesicles

Matrix vesicles can be found within the extracellular matrix of developing bone and cartilage and remain poorly defined. Typically sized below 300 nm with a phospholipid

bilayer membrane, they are often found colocalised with calcium phosphate [79]. The biogenesis of matrix vesicles is debated, with membrane budding from mineralising cells thought to be most likely, however unique markers for MVs have not yet been identified [80]. Evidence linking MVs and exosomes within a murine osteoblastic cell line (KUSA-A1) has been proposed by Iwayama *et al.* [81]. Using scanning electron-assisted dielectric microscopy and Raman spectroscopy, they found phosphate and calcium containing exosomes within acidic multi vesicular bodies, as well as extracellular MV like bodies positive in calcium and phosphate. CRISPR-Cas9 knock out of ALPL, a protein strongly associated with osteoblast exosomes, also inhibited the formation of the MVs, as did inhibiting lysosomal exocytosis.

Table 1.1 : Types of microparticle found in the size range of extracellular vesicles, their identifying surface markers and contents. Selected microparticle characteristics. Illustration of key differences between microparticles, as well as overlaps in size and cargo that make purification and identification difficult. Adapted from Greening et al. 2017 [82]

Microparticle	Biogenesis	Size (nm)	Surface markers	Contents
Exosomes	Endosomal, intracellular budding within vesicles	30-150	CD63[83] CD81[84] Various integrins[64]	RNAs [85] DNAs [86] Cytoplasmic and membrane proteins[64]
Microvesicles	Cell surface budding of plasma membrane	100-1500	KIF23[87] RACGAP[87]	RNAs [66] DNAs [88] Cytoplasmic and membrane proteins [64]
Apoptotic bodies	Apoptotic cell surface blebbing	500-2000	Phosphatidylserine [89] Histones [90] Cytochrome C [91]	Nuclear DNAs [92] Cell organelles [93]
Matrix vesicles	Unconfirmed but thought to be budding from mineralising cell surface	<300	TNAP [94] ENPP[94]	Calcium phosphate[94]

1.7.3 Supporting evidence for EVs involvement in mineralisation

There is strong evidence linking EVs to the mineralisation process. The translocation of calcium and phosphate containing vesicles from within osteoblasts to the extracellular environment has been documented [95]. These same calcium and phosphate compounds have also been observed in zebrafish fin models of mineralisation, where submicron globules were found colocalised with mineral nucleation sites on collagenous matrix, in a manner similar to osteoid formation[96]. Furthermore, mesenchymal stem cells have been shown to mineralise when co-incubated with EVs isolated from mineralising osteoblasts, whereas non mineralising osteoblast EVs were much less effective [97], again supporting a role for EVs in the mineralisation of tissues.

1.7.4 EV related proteins in mineralisation

The annexin family of proteins consist of calcium-dependent, phospholipid binding proteins, and several members of this family (annexins II, V and VI) have been associated with osteoblast derived EVs [97]. These specific annexins have been reported to facilitate binding interactions between collagen, calcium, and phospholipids found

in EV membranes [98]. Taken together, the binding of Ca^{2+} ions, EV phospholipids, and collagen suggest that osteoblast derived EVs may provide a function of increasing Ca^{2+} ion concentration in the immediate vicinity of collagen in newly mineralising bone.

Phosphorous releasing enzymes, such as TNAP and ectonucleotide pyrophosphatase phosphodiesterase-1 (ENPP1) have also been associated with extracellular vesicles [94]. The primary substrate of ENPP1 is adenosine triphosphate (ATP), which is cleaved to form adenosine monophosphate (AMP) and pyrophosphate ($P_2O_7^{4-}$) (PPi) [99]. Whilst PPi is a known potent inhibitor of the conversion of ACP to HA[100,101], tissue nonspecific alkaline phosphatase (TNAP) enzymatically catalyses the conversion of PPi to inorganic phosphate (PO_4^{3-}) (Pi) [102]. TNAP therefore provides a twin role in mineralisation, by catalysing the hydrolysis of PPi, an inhibitory molecule is removed, and replaced with Pi, a substrate for the formation of ACP and subsequent mineralisation (Figure 1.4). The expression of these two enzymes must be a closely regulated relationship during mineralisation, increased expression of ENPP1 results in an excess of PPi, and an inhibition of mineralisation, whereas increased TNAP expression reduces the concentration of inhibitory PPi and provides Pi for ACP formation. Fine regulation of this PPi : Pi ratio is therefore key in mineralisation processes.

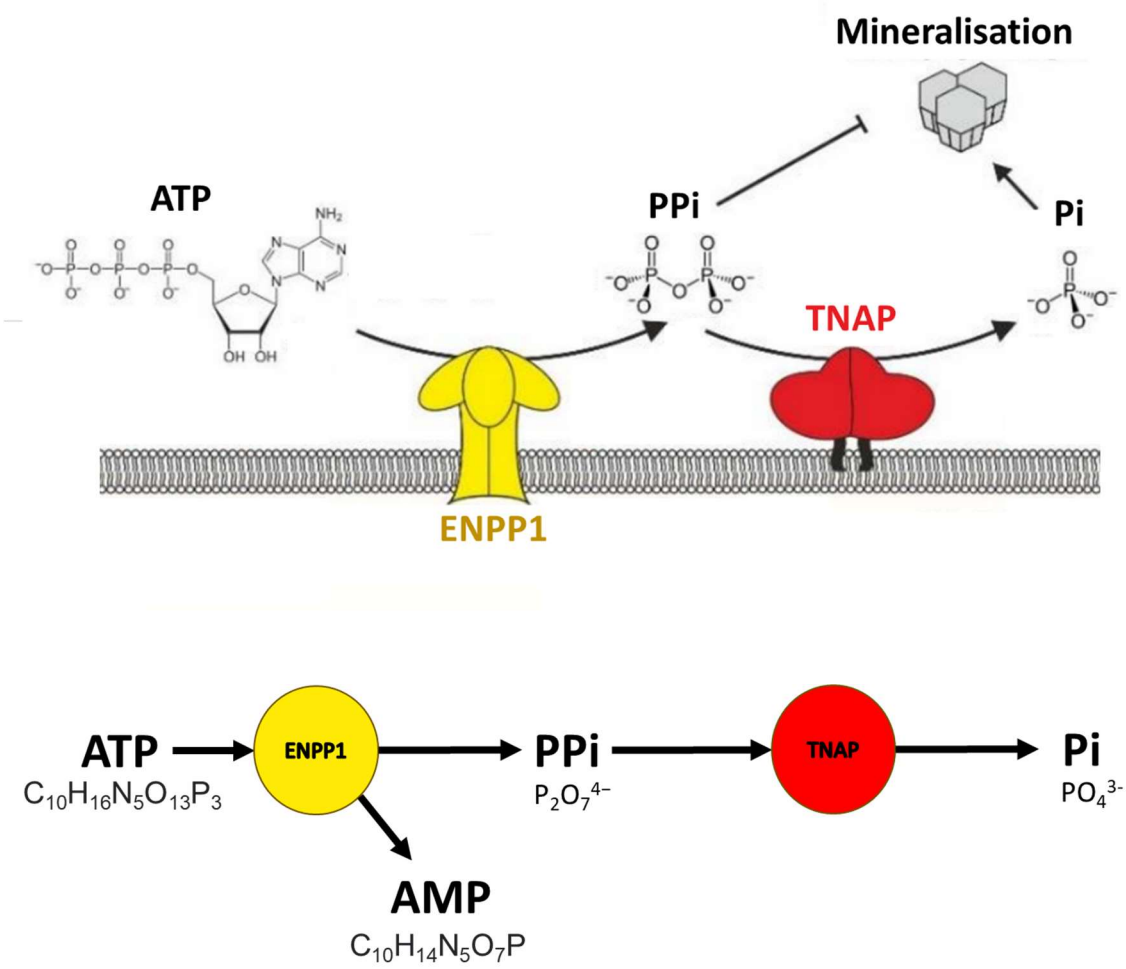

$C_{10}H_{16}N_5O_{13}P_3 + H_2O \rightarrow C_{10}H_{14}N_5O_7P + P_2O_7^{4-} + 4H^+$ $P_2O_7^{4-} + H_2O \rightarrow 2HPO_4^{2-}$

Figure 1.4: Schematic model of the potential roles of extracellular vesicle membrane bound Tissue nonspecific alkaline phosphatase (TNAP) and ectonucleotide pyrophosphatase phosphodiesterase-1 (ENPP1). Adenosine triphosphate (ATP) is hydrolysed by ENPP1, producing adenosine monophosphate (AMP) and pyrophosphate (PPi). PPi is subsequently broken down into inorganic phosphate (Pi) by TNAP. Increased local concentration of Pi favours the formation of ACP. Adapted from Liedke *et al.* [103]

Another protein upregulated in the mineralising EV proteome, osteopontin (OPN) [104], is considered essential in collagen biomineralisation [105]. One theory for its role in mineralisation is due to its highly negatively charged polyAspartic acid motif (polyAsp), which, as mentioned previously, may play a role in stabilising the amorphous mineral phase, permitting entry between collagen subunits. Additionally, OPN, and other small integrin-binding ligand N-glycosylation (SIBLING) family proteins (DMP1, bone sialoprotein (BSP), dentin sialophosphoprotein (DSPP) and matrix extracellular

phosphoglycoprotein (MEPE)), have the capacity to bind to collagen in a site-specific manner, whilst being able to form interactions with or accumulate calcium ions [106].

Finally, the acidic phospholipid bilayer membrane of EVs has also been hypothesised to provide a negatively charged environment conducive to the stability of intermediate phosphate stages in the formation of HA, such as octacalcium phosphate [97], which are more stable at lower pH.

The fine balance of these molecules may maintain a thermodynamically favourable environment for ACP in the extra fibrillar space, whilst exclusion of molecules larger than 40 kDa from intrafibrillar gaps in collagen fibrils [42] permits crystal formation, critical in new bone formation. Understanding the proportions and interactions that occur between them *in vivo* should provide critical knowledge on the early stages of bone formation.

The association of EVs with calcium and phosphate ions, proteins capable of phosphate catalysis, collagen binding, and ACP stabilisation strongly support the theory that they are instrumental in mineralisation of collagen, and early bone synthesis [107]. It is also believed that EVs may play important roles in regulating cells involved in bone homeostasis, increasing osteoblast mineralisation [97], osteoblast-osteoclast communication [108], and delivery of miRNA to osteoblasts [109]. Mineralising EVs have also been suggested as an important factor in plaque calcification, a key factor in atherosclerotic disease [110], an aberrant and potentially fatal mineralisation process. Decoding the apparent ability of EVs to stimulate host processes key in mineralisation may present a tremendous therapeutic opportunity.

1.7.5 Are EVs alone capable of fuelling mineralisation?

The means by which calcium and phosphate is concentrated at the site of new bone formation is currently unclear, whether vesicles are solely capable of delivering the phosphate (PO_4) required to construct ACP is debated. Some of these raw materials are certainly contained within EVs, here we calculate the maximum weight of PO_4 that could potentially be delivered by EVs, should they contain only PO_4 ions, an extremely unlikely condition. Human adult femoral lamellar bone is typically constructed from 11.1% PO_4,[111]with a molecular weight of 94.97 g/mol, this suggests there are 0.00117 moles of PO_4 per gram of bone. Avogadro's number instructs there are approximately

$7.04x10^{20}$ molecules of phosphate in a typical gram of bone. Vesicle sizes range between 30-2000 nm in diameter, but reported mean values vary depending upon the collection and measurement method used. Our previous data from vesicles isolated using multi step ultracentrifugation and measured using Dynamic Light Scattering (DLS) technique (Zetasizer Nano ZS, Malvern Panalytical Ltd, UK) suggests the weighted mean diameter of a mineralising osteoblast vesicle is approximately 127 nm, providing a volume of $1.06x10^6$ nm^3. The polar surface area of a PO_4 molecule is given as 0.86 nm^2 [112] making the volume of a tetrahedral PO_4 approximately 0.041 nm^3. In the theoretical event that the average vesicle contains only PO_4 molecules, it would contain approximately $2.59x10^7$ phosphate ions, discounting the charge interactions between molecules. This suggests that to construct 1 g of bone, $2.72x10^{13}$ vesicles consisting of solely PO^4 would be required.

We were able to isolate 1.5 $x10^{12}$ vesicles from a mineralising culture of 1.72 $x10^7$ MC3T3 cells (conservative estimate), a murine osteoblast-like cell, across two-weeks. Using the above figures, our culture of 17 million osteoblasts would provide enough PO_4 to create 4 mg of new bone per day, thus, a single gram of femoral lamellar bone would require the daily EV output of 437 million osteoblasts. This is true only if each osteoblast produced vesicle contains only phosphate molecules, likely impossible, as many other types of molecules are regularly found associated with EVs, such as proteins, RNA, and other ionic species.

Table 1.2 Calculations of possible mineral content of osteoblast EVs. Estimations of maximum possible phosphate content delivered by osteoblast EVs if phosphate ions were the only cargo.

Measurement	**Value**
Mean EV diameter (own data)	127 nm
Mean EV volume	1.06 x10^6 nm^3
Phosphate ion polar surface area	0.86 nm^2
Phosphate ion volume	0.041 nm^3
Maximum number of phosphate ions/EV	2.59x10^7
Phosphate percentage of human adult femoral lamellar bone [111]	11.1%
Molecular weight of phosphate ion	94.97 g/mol
Phosphate moles/gram bone	0.00117 m/g
Number of phosphate molecules/gram bone	7.04x10^{20}
Number of EVs required for 1 gram of bone	2.72x10^{13}
Number of EVs produced per day by approximately 1.72x10^7 osteoblasts in culture (own data)	1.07 x10^{11}
Potential weight of bone produced from 1.72 x10^7 osteoblasts/day	3.938 mg
Number of osteoblast cells to produce 1g of bone	4.37x10^9

1.7.6 Platelets as a potential source of mineralising components

As previously stated, we believe it is unlikely for EVs to be the only source of phosphate for new bone formation, therefore we must look for other potential sources. An interesting potential source could well be platelets and their releasate. Platelets can promote wound healing, and consequently the growth of new tissue, becoming activated at the site of injury which causes the release of internal cargo, a process called degranulation. Previous animal studies have shown that the resulting platelet releasate and platelet products can have a significant positive impact upon bone growth [113,114]. Dense granules within mammalian platelets are known to contain long chain polyphosphates (polyP) [115], at a concentration 10-20-fold higher than in major organs [116], as well as ATP [117], both known substrates for EV related enzymes and a potential source of phosphate for ACP and bone mineralisation. Storage of phosphate in these long chains also permits the simultaneous storage of divalent cations, such as calcium, at high concentrations [118].

Platelets are known to aggregate in the presence of adenosine diphosphate (ADP) [119], whilst AMP has been shown to trigger ATP release from platelets. Both ADP and AMP are likely to be present at the site of new bone growth due to the activity of osteoblast EV derived transmembrane ENPP1 and membrane bound TNAP. These enzymes catalyse the cleavage of ATP to AMP and ADP respectively [99], which would in turn cause aggregation and degranulation of platelets, and the release of their phosphate containing cargo in the immediate vicinity of mineralising collagen, potentially providing raw materials for new bone formation (Figure 1.5).

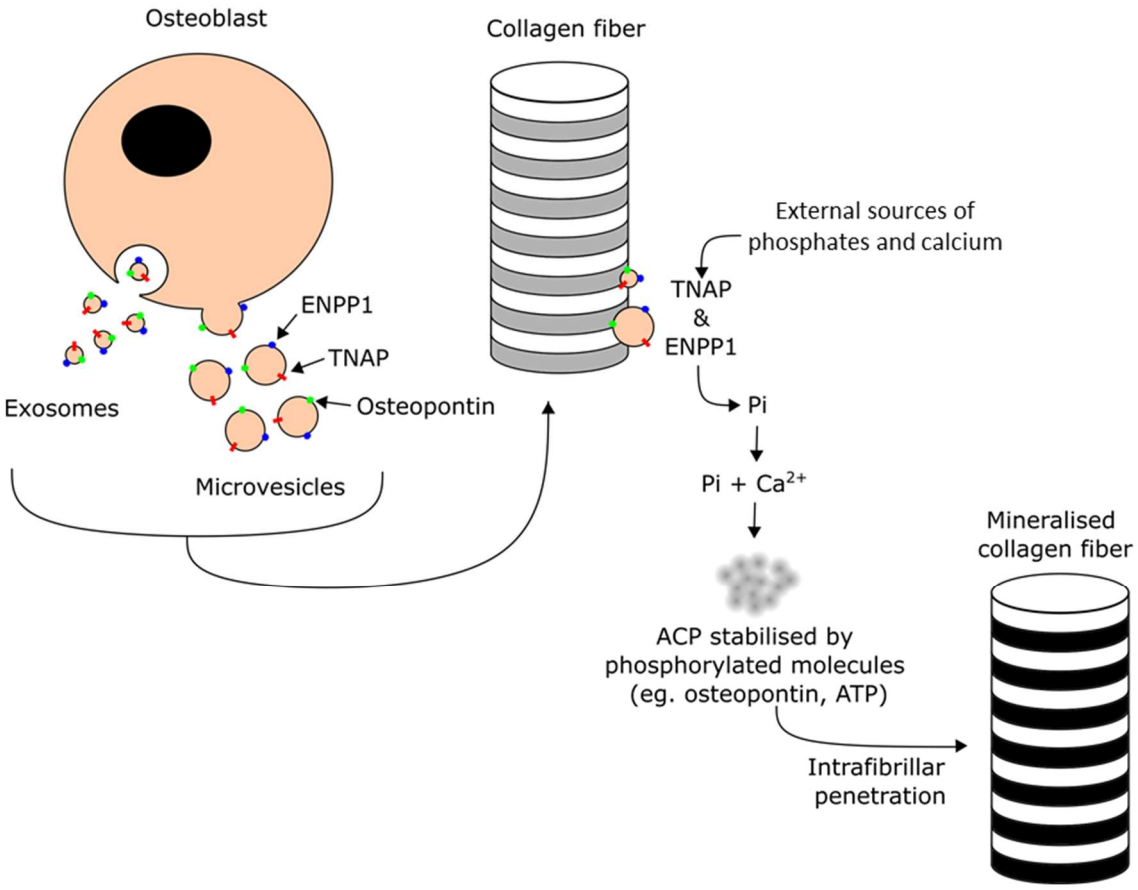

Figure 1.5 Theory of intrafibrillar mineralisation. Mineralising osteoblasts release extracellular vesicles (EV) near newly forming bone. Vesicles adhere to collagen fibrils in newly developed osteons, via osteopontin and related proteins. EV cargo increases local concentrations of calcium (Ca^{2+}) and inorganic phosphate (Pi) molecules. Levels are increased further by EV borne tissue nonspecific alkaline phosphatase (TNAP) and ectonucleotide pyrophosphatase phosphodiesterase-1 (ENPP1) dependent enzymatic breakdown of polyphosphates from external sources. High concentrations of Ca^{2+} and Pi favour the formation of amorphous calcium phosphate, which is stabilised by phosphorylated molecules such as ATP and Osteopontin, this permits small ACP molecules to penetrate gaps within the collagen fibrils, and subsequent crystallisation to more thermodynamically favourable hydroxyapatite.

1.7.7 Heterogeneity of EVs

The existence of extracellular vesicles was discovered more than 50 years ago, but appreciation of the diversity and heterogeneity of EV populations has accelerated rapidly in the last decade. Research published in 2013 by Tauro *et al*. [120] used anti-A33 or anti-EpCAM magnetic beads to isolate two populations of exosomes from the carcinoma cell line LIM1863, and analysed the proteome using gel based liquid chromatography mass spectrometry (LC-MS/MS). The two populations demonstrated a marked difference in proteins found within the two differentially isolated populations, 684 proteins were common to both exosomal datasets, whilst 340 and 214 proteins were found only in A33- and EpCAM isolated populations, respectively. An interesting detail in this data was that there was an absence of major histocompatibility complex (MHC) class I or II proteins in the EpCAM isolated population. In 2015 Keerthikumar *et al*. [121] published work demonstrating a significant difference in protein expression, using label-free quantitative proteomics, for neuroblastoma cell (SH-SY5Y) EVs separated on a size basis. The EV population typically larger than 150 nm contained 770 different proteins at twofold or greater higher abundance, and 693 at half the abundance or less, when compared to EVs smaller than 150 nm. Additionally, they found bioactivity differences, with the smaller sized population inducing significantly greater cell proliferation and migration in SK-N-BE2 neuroblastoma cells. A review by Vagner *et al*. [122] provides an excellent summary of recent knowledge of protein variability; highlighting heterogeneity between different sizes of EVs taken from the same cell [87,123], similar sized EVs from different cell sources, with only 3.5% of proteins present in all EV samples taken from 60 cell lines [124], and even EVs released from different sides of the same polarised epithelial cells displayed [120,125,126].

In addition to protein cargoes, RNA profiles of EVs from different cell lines have been shown to reflect a similar pattern [92], with ribosomal RNA present in the larger apoptotic bodies, no RNA found in microvesicles (MiV), whilst exosomes contained smaller RNA fragments, and no ribosomal RNA. However, this pattern was not the same for all cell lines investigated, with one cell line (TF-1) showing ribosomal RNA in the MiV population, although it cannot be guaranteed that this is not simply contamination of the MiV population by apoptotic bodies.

In addition to differences in EV composition based on the donor cell type, there is evidence of cell culture architecture impacting EV output too. Cells cultured in three-dimensional (3D) culture conditions have been shown to produce significantly more EVs per cell than two-dimensional (2D) cultures, with lower protein content and upregulated miRNA content [127]. Furthermore, EV RNA profiles from 3D systems appear to mimic that of the donor patient plasma more closely (96%) than that of 2D culture EVs (80%) [128].

Cells grown in 3D cell culture are presented with a varied topography, offering a diverse range of adhesion and interaction angles with the growing surface, as well as other cells within the culture. This is likely to be more mechanically and physiologically representative of *in vivo* conditions than simple 2D culture, which offers a simple, rigid growth surface. The current techniques involved in the manufacture of micro scaled 3D scaffolds include solvent casting, freeze drying and gas foaming. These techniques are not yet capable of producing scaffolds with reliable, repeatable parameters [129], limiting the repeatability of EV populations obtained when using them. Alternative materials used to create 3D culture structures such as hydrogels often present difficulty in collecting the EVs, requiring additional processing steps, affecting EV yield and functionality in unknown ways [130].

Promising results from Man *et al.* [131] produced controlled titanium scaffold architecture using surface layer additive manufacturing. They demonstrated that 3D printed titanium scaffolds coated with hydroxyapatite produced significantly different EV yields dependent upon pore size and shape. Triangular shaped pores demonstrated an increased EV yield, and these EVs also demonstrated increased ability to induce mineralisation in osteoblasts when compared to square pores. Data on the comparison of the EVs produced by these 3D grown osteoblasts compared to 2D grown osteoblasts does not appear to have been collected.

The heterogeneity discussed here has been shown to be affected by the method of isolation utilised in the EV collection process, work carried out by Azkagorta *et al*. [132], compared proteomes obtained from human blood samples using 4 different isolation methods, ultracentrifugation (UC), size exclusion chromatography (SEC), and two commercial kits, one for polymer precipitation (INV) and the other for glycosylated

group precipitation (GAG). Comparatively, the proteome from EVs enriched using UC was much larger, and included mitochondrial and ribosome related proteins, a potential indicator for contamination from cell debris. SEC showed evidence of lipoprotein associated proteins, again, showing evidence for lipoprotein contamination. The INV kit had more affinity for proteins associated with granules of platelets. The precipitation kit that targets glycosylation molecules enrich differentially protein harbouring glycosylation sites, including immunoglobulins and proteins of the membrane attack complex. This study suggests that whilst EV populations are unquestionably diverse, we must take care to notice that some of this diversity may be due to collection methods employed.

EVs have been shown to treat disease states in animal models [133,134], however, the overwhelming evidence of EV heterogeneity makes it necessary to obtain high resolution methods of characterising the huge diversity in content of EVs. In doing so, we hope to identify the most important bioactive components, moving towards further usage in the clinical setting.

1.8 Thesis aims

This thesis aims to further understand the early mineralisation process and determine the roles that extracellular vesicles play in this using an established *in vitro* model of mineralisation. To provide an insight into this poorly understood process we have undertaken work to:

1. Determine the changing stoichiometry of mineral deposited by differentiated MC3T3 murine pre-osteoblast cells, observing changes that occur with maturation of mineral nodules, and how this relates to mature bone, which is predominantly HA.
2. Determine whether Raman spectroscopy can be used to probe the composition of vesicles to investigate the theorised link between vesicle secretion and mineral composition.
3. Use both methods to explore how vesicles influence the progression of mineralisation and the characteristics therein.

By performing the above investigations, we aim to provide novel insights into the biochemical processes occurring during very early mineralisation. This is a field that is currently underdeveloped, with multiple unknowns. Clarifying the presence and progression of calcium phosphate species during mineralisation will contribute to better understanding of this early process. Improving the methods of characterising extracellular vesicles, will facilitate the identification of subset populations within the EV secretome, allowing more effective investigations into the methods of action of EVs. Finally, combining the two methods, will highlight ways to obtain additional data on the mineralisation process, contributing to the drive to understand these processes better.

Chapter 2 : Evaluating the chemical evolution of mineral formation using XRF

2.1 Introduction

The current "gold standard" in the field for evaluating the mineralisation process *in vitro* is in 2D cultures of mineralising osteoblast-like cells. Currently, mineralisation is quantified using the amount of calcium present, via the stain alizarin red or von Kossa staining. Notably, these methods only indicate whether there is the localisation of calcium or phosphate in solid form in the culture. Whilst they are rapid and simple, providing a useful indication of total mineralisation, they do not offer information regarding the biochemical processes or the structural and chemical evolutions that occur within the culture.

X-ray fluorescence (XRF) is an analysis technique that is used to obtain information on the elemental composition of a target material, it is traditionally used to interrogate glasses, metals and ceramics, however, it also has uses in biological research. The technique involves bombarding a sample with an x ray beam, which is absorbed by an atom within the sample, transferring the energy held by the x ray photon to the atom. If the total energy transferred to the atom is greater than the binding energy of the electrons in the low energy, inner orbital shells (known as K or L shells), this transferred energy will cause one of these electrons to be ejected (see Figure 2.1). An atom missing an electron in an inner orbital shell is unstable, and this vacancy will be filled by a high energy, outer shell electron, which will drop down to the lower energy orbital shell. As these high energy electrons move to the lower energy shell, they emit the additional energy in the form of an x ray photon. The energy of this ejected photon is highly predictable, as the electromagnetic force that holds the electron in each orbital shell is dependent upon the number of protons and neutrons within the nucleus. Proton number is unique to each element; therefore, the energy of each electron orbital shell is also unique, making it possible to calculate the energy emitted when electrons move between shells, and thus, the atom's energy fingerprint. An XRF machine will bombard samples with x ray energy and simultaneously detect the energy of emitted x rays, obtaining the unique energy fingerprint for all the atoms it detects. These energies are collected into a spectrum, where the energies identify the elements

present, and the intensities of signal at these energies correspond to the concentration of that element.

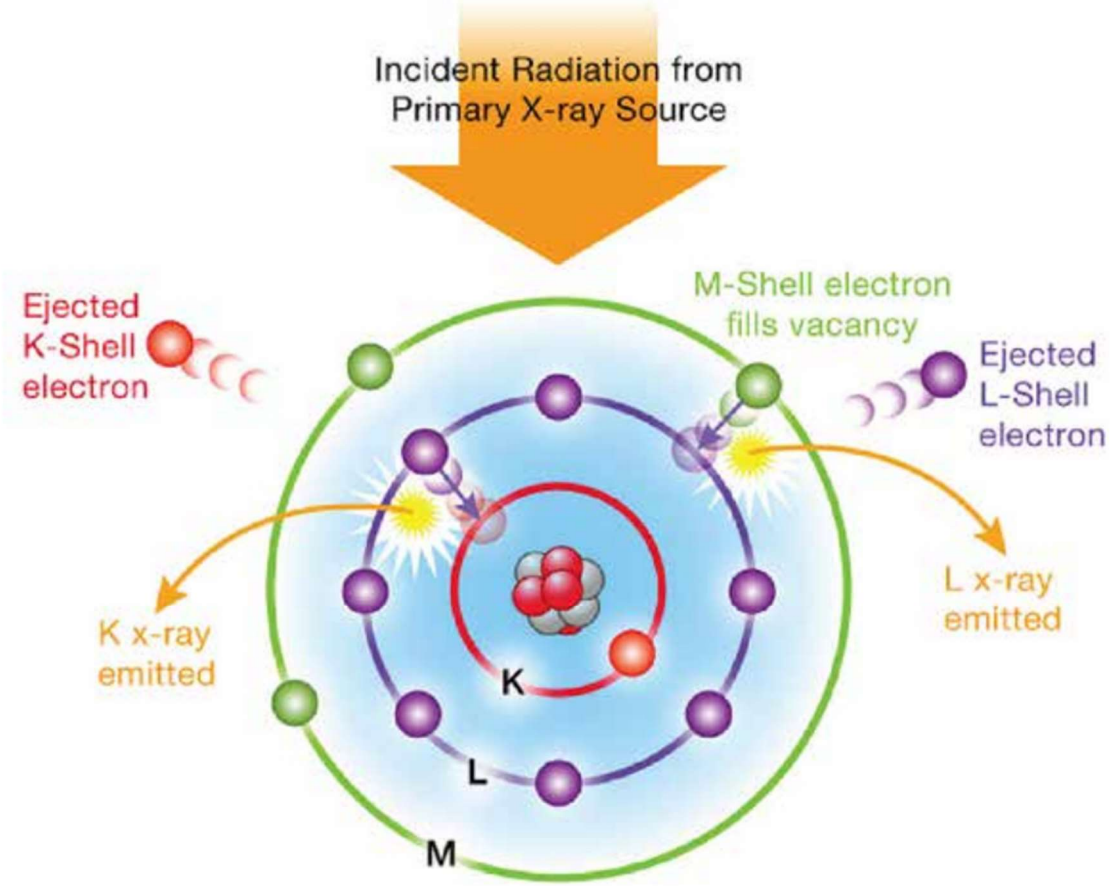

Figure 2.1: Diagram explaining the unique elemental energy levels detected by an XRF. Incoming x ray energy is absorbed by an atom, and if sufficient to overcome the binding energy of an inner shell electron, will cause the ejection of an electron. Outer shell electrons will shed energy in the form of an x ray of predictable energy to move down into the lower energy shells to stabilise the atom. Reproduced from XRF Technology in the field. ThermoFisher Scientific, 2021[135]

Such detailed information regarding the elemental composition of a sample can be utilised to provide a unique insight into stoichiometry of early mineralisation. The ability to obtain this data without requiring extensive sample preparation or large and/or technically demanding equipment such as a synchrotron, electron or multi photon microscope, may help us to further determine the processes that occur during early bone formation. Benchtop micro X-ray fluorescence (μXRF) allows this, with penetration of samples in the tens of microns making it highly suitable for cell culture analysis.

Potential drawbacks include the ability of air to scatter the weaker x rays used in this machine, this can be solved by imaging the samples under vacuum or very low air density, however, this requires the samples to be fixed and dried. Additionally, μXRF is also unable to detect elements below an atomic number of 6. Beyond fixation and drying, μXRF testing is non-destructive, allowing the possibility of further interrogating the samples used to obtain additional characteristics. The data obtained from μXRF analysis may be very useful in elucidating the early changes occurring in mineralisation, coupling μXRF analysis with Fourier transform infrared spectroscopy or Raman spectroscopy, may offer a promising amount of data on the chemistry involved in early mineralisation.

This chapter focusses on the evaluation of mineral stoichiometry during cell culture using μXRF, identifying the structural and chemical evolution of the mineral phase *in vitro*.

2.2 Methods

2.2.1 Micro-XRF

Maps of elemental composition across various sample types were acquired using a Tornado M4 micro-XRF system (Bruker Nano, Germany) fitted with a Rhodium micro focus X-Ray tube and a polycapillary lens, with the X-ray tube set to 50 kV voltage and 400 µA current. The chamber pressure was lowered to 20 mbar to maximise sensitivity of signal. The system was programmed to acquire a map across the sample by rastering the microfocus beam over the slide with a pixel size of 20 µm and a time per pixel of 10 ms, this process was repeated five times. An XRF spectrum was collected at each pixel and elemental maps generated progressively in real time, creating an image where pixel intensity represented X-Ray detector pulses per eV at each measurement point on the sample. Intensities were normalised to rhodium peaks to allow comparison between samples.

2.2.2 Calcium phosphate standards

A selection of calcium phosphate compounds was used to produce reference standards for the µXRF. These compounds were; monocalcium phosphate monohydrate (Sigma-Aldrich, UK), calcium pyrophosphate (Sigma-Aldrich, UK), β tricalcium phosphate (Sigma-Aldrich, UK), hydroxyapatite and brushite (both synthesised by Dr. Erik Hughes, University of Birmingham). A small amount of each powder was placed into a polystyrene 6 well plate, the upper surface flattened to provide stable focus for the µXRF, and placed in the chamber, atmospheric pressure within the chamber was reduced to 20 mbar to reduce absorbance of emitted x ray beams by air molecules. A 2mm^2 area of each sample was interrogated by x ray beams and subsequent emission spectra obtained, spectra were normalised to the rhodium peaks as this is an artifact of the x ray emitter and constant dependent upon the power of the beam. A ratio of the signal intensities corresponding to calcium and phosphate was produced and a scatter plot created for signal ratio against elemental ratio. These known standard compounds produced a standard curve which provided a conversion factor that can be applied to µXRF Ca:P signal ratio to estimate elemental Ca:P ratio in other materials.

2.2.3 MC3T3 cell culture

MC3T3 murine pre-osteoblasts were purchased from American Type Culture Collection (ATCC, UK). Growth culture media consisted of minimal essential medium (α-MEM; Sigma-Aldrich, UK), 10% fetal bovine serum (FBS), 1% penicillin/streptomycin (Sigma-Aldrich, UK) and L-glutamine (Sigma-Aldrich, UK). MC3T3s were cultured at scale in T175 culture flasks (Nunc, UK) and the medium collected and refreshed three times weekly. Cells were grown in either growth culture medium described above, or osteogenic medium for a total period of 21 days. Osteogenic medium comprised of growth culture media supplemented with 10 mM β-glycerophosphate (Sigma-Aldrich, UK) and 50 µg/ml L-ascorbic acid (Sigma-Aldrich, UK).

2.2.4 Alkaline phosphatase activity

Alkaline phosphatase activity was quantified using 4-nitrophenyl colourimetric phosphate liquid assay (pNPP, Sigma-Aldrich, United Kingdom). Cells were cultured in Corning Costar 48 well plates for the appropriate length of time according to experimental design. Cell monolayers were scraped and lysed in 0.1% Triton™ X-100, and added to 90 µL of pNPP and incubated for 60 min at 37°C. The absorbance at 405 nm was read on a SPARK spectrophotometer (TECAN, Switzerland).

2.2.5 Alizarin red calcium quantification

Alizarin red staining was used to quantify overall calcium deposition. Cells were cultured in Corning Costar 48 well plates for the appropriate length of time according to experimental design. Cell monolayers were washed twice in PBS and fixed in 10% neutral buffered formalin for 30 min. Once fixed, cells were washed in distilled water and then incubated with alizarin red solution (Sigma-Aldrich, United Kingdom) for 10 minutes. Samples were washed with distilled water again to remove unbound dye. Stained samples were eluted with 10% cetylpyridinium chloride (Sigma-Aldrich, United Kingdom) for 1 h. Following this, absorbance was obtained at 550 nm using the SPARK spectrophotometer (TECAN, Switzerland).

2.2.6 Computer analysis of mineral nodules

Comparison of nodule area and number across treatment types was carried out via MATLAB analysis of XRF elemental maps. Elemental maps across all timepoint samples

were taken in a single image, obtained using the Tornado M4 micro-XRF system (Bruker Nano, Germany), where X ray fluorescence spectra were obtained from each 20µm pixel. The data obtained provided a multispectral datacube of elemental signal/concentration from each 20µm pixel (repeated 3 times for accuracy), providing maximum and minimum calcium levels across every sample. This data was converted into a greyscale image, with maximum concentration of Ca displaying as white, and minimum as black, with points in between displaying as a greyscale. The Otsu method was used to define a threshold of significant Ca signal, defining areas of the image as having significantly increased Ca presence, or non-significant Ca presence. Visual comparison of these locations of increased calcium and phosphorous concentration co-located exactly with visible depositions of white material when viewed with 10x magnification under brightfield conditions. These areas were defined as mineral nodule locations. This analysis was repeated for phosphorous signal. This provided a reliable, repeatable method that could be applied across samples of varying levels of mineralisation. These locations of increased Ca & P concentration were counted, and mean area was then obtained for these nodule objects, and compared across timepoints. Code attached below.

2.2.7 Nodule analysis code

The following Matlab code was used to enable the analysis of the mineral nodules that were formed in MC3T3 cell mineralisation, this code produces a quantifiable value for nodule size and number, permitting comparison between cultures.

```
clear; close all; clc; %housekeeping

%read in all files with a .jpg ending
cd Images %name of subfolder where pictures are kept
jpgFiles = dir('*.jpg'); %Structure variable with each cell containing an
image
numpics = length(jpgFiles);

rgb = cell(1,numpics);
binaryimg = cell(1,numpics);
num_circle = 10;
orderedcircles = cell(1,num_circle); %cell array for the ordered circles

Percent_array = zeros(num_circle,numpics);
ObjNum_array = zeros(num_circle,numpics);
AvgSize_array = zeros(num_circle,numpics);
Range_array = zeros(num_circle,numpics);


%reading in and saving all pics
for k = 1:numpics
    rgb{k} = imread(jpgFiles(k).name);
end
```

```
cd ..\ %exiting out of the subfolder

for k = 1:numpics
    gs = rgb2gray(rgb{k}); %converting first to a greyscale image for the
thresholding method
    gs_adj = histeq(gs); %enhancing contrast with histogram equalization
    x = otsu_m(gs_adj);
    binaryimg{k} = imbinarize(gs,x);
    circles = imbinarize(gs,0.05); %value found subjectively
    circles = bwpropfilt(circles,'area',num_circle);
    circles_cleaned = imfill(circles,'holes');



    %We need to organsie the circles currently goes from left to right but
    %top to bottom is seemingly random
    L = bwlabel(circles_cleaned); %Each circle is labeled from 1-10
    s = regionprops(L, 'Centroid'); %The corresponding centre for each label
is given


    centre = extractfield(s,'Centroid');
    %data is in a singel column vector in order of x coord, y coord for
    %each object
    centrey = centre(2:2:end);
    avgy = mean(centrey);
    bottomrow = find(centrey>avgy);
    %bottomrow is greater than as y axis is flipped
    toprow = find(centrey<avgy);

    for orderindex = 1:5
        orderedcircles{orderindex} = (L == toprow(orderindex));
        orderedcircles{orderindex+5} = (L ==bottomrow(orderindex));
    end


    %Finding boundaries of the circles to be analysed
    boundaries = bwboundaries(circles_cleaned);

    for count = 1:num_circle
        %cropping to a particular circle
        b = bwboundaries(orderedcircles{count});
        b = b{:};
        xb = b(:,2);
        yb = b(:,1);
        rect = [min(xb),min(yb),(max(xb)-min(xb)),(max(yb)-min(yb))]; %need
coordinates of the top left corner and the length in the x and y direction
        crop_circle = imcrop(circles_cleaned,rect);
        crop_binary = imcrop(binaryimg{k},rect);

        %disp([min(xb),min(yb),count]);

        %Finding % area
        Percentarea = percentareafinder(crop_circle,crop_binary);
        %Finding size and number of objects
        [obj_number, avg_size, range] = sizefinder(crop_binary);

        %Storing results in arrays
        Percent_array(count,k) = Percentarea;
        ObjNum_array(count,k) = obj_number;
        AvgSize_array(count,k) = avg_size;
        Range_array(count,k) = range;
    end

end


circle_no = [17.1:0.1:17.5, 21.1:0.1:21.5]';

%Calcium table
Ca_Results = [Percent_array(:,1),...
    ObjNum_array(:,1),...
    AvgSize_array(:,1),...
```

```
    Range_array(:,1)];
TCa = array2table([circle_no,Ca_Results],'VariableNames',{'Day'...
    'Percentage Calcium'...
    'Number of objects'...
    'Average area of objects (Pixels)'...
    'Range in area of objects (Pixels)'});

%Phosphorus table
P_Results = [Percent_array(:,2),...
    ObjNum_array(:,2),...
    AvgSize_array(:,2),...
    Range_array(:,2)];
TP = array2table([circle_no,P_Results],'VariableNames',{'Day'...
    'Percentage Phosphorus (%)'...
    'Number of objects'...
    'Average area of objects (Pixels)'...
    'Range in area of objects (Pixels)'});

disp('Calcium:');
disp(TCa);
disp('Phosphorus:');
disp(TP);

%Exporting tables to an excel file called 'Results'
writetable(TCa,'Results.xlsx','Sheet',1);
writetable(TP,'Results.xlsx','Sheet',2);

montage({rgb{:},binaryimg{:}});
```

2.2.8 Statistics

All statistical analysis was performed using GraphPad Prism version 5.03 for Windows, GraphPad Software, San Diego California USA, www.graphpad.com.

2.3 Results

2.3.1 Optimising the Tornado M4 micro-XRF system

Optimising the Tornado M4 micro-XRF system for use on cell culture samples involved a compromise between spatial resolution, detection limits, and acquisition time. Increasing resolution was essential to attempt location of mineral differences within micrometer sized mineral nodules present in the samples, whilst repeated interrogation of the sample was also necessary to reduce signal-to-noise ratio. These competing requirements necessitated systematic adjustments to the X-ray spot size, dwell time per pixel, and repeats per pixel with extensive trials performed on cell culture samples to determine the optimal configuration.

Firstly, working under a vacuum was essential to improve the signal-to-noise ratio by removing air attenuation, this added complexity by necessitating additional sample preparation steps. It also removed the possibility of observing nodule deposition and mapping in real time across the time periods.

Following this, focal size was reduced to the smallest reasonable size to maximize spatial resolution, though this resulted in a larger number of readings per micrometer, necessitating longer acquisition times. This increase in data collected had a correlating effect on file sizes, which, when too large, would overwhelm the memory capability of the associated software resulting in software crashes.

Eventually, an effective compromise between all competing factors was reached wherein a pixel size of 20 µm, time per pixel of 10 ms, and 5 repeats per pixel allowed sufficiently high-resolution imaging of the samples while keeping acquisition time and file sizes manageable.

2.3.2 Obtaining XRF standards

To use XRF as a quantitative measure of elemental composition, it must first be shown that the technique can show a proportional signal response to differing amounts of the elements we are quantifying. To do this, compounds with varying proportions of calcium and phosphorous were analysed, and the relative ratio of calcium to phosphorous plotted against the elemental ratio in the chemical formulae (Figure 2.2). Samples of monocalcium phosphate monohydrate ($CaH_4P_2O_8$), brushite

($CaHPO_4 \cdot 2H_2O$), calcium pyrophosphate ($Ca_2P_2O_7$), β tricalcium phosphate ($Ca_3(PO_4)_2$) and hydroxyapatite ($Ca_{10}(PO_4)_6(OH)_2$) were analysed, with sodium polyphosphate ($Na_5P_3O_{10}$) used as a negative control. A rastering scan obtained XRF spectra from 15,625, 20 micrometer pixels, taking 10 milliseconds per pixel across a $2mm^2$ area of each powdered sample. This was repeated 5 times, a mean calculated and plotted in Figure 2.2. Results showed a reliable positive correlation ($R^2 = 0.984$), suggesting XRF can be reliably used to interpret calcium and phosphorous signal as a proportion of the elemental presence.

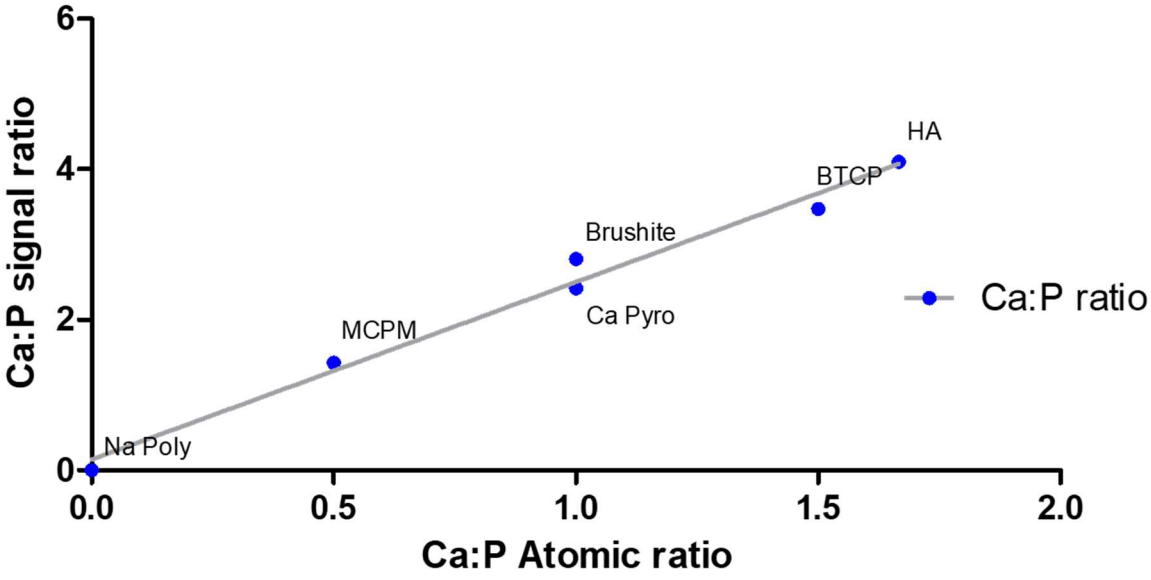

Compound	Ca:P elemental ratio	Ca:P signal ratio
Sodium polyphosphate	0	0.001
Monocalcium phosphate monohydrate	0.500	1.426
Brushite	1.000	2.805
Calcium pyrophosphate	1.000	2.420
B tricalcium phosphate	1.500	3.471
Hydroxyapatite	1.666	4.098

Figure 2.2: XRF standards of calcium phosphate compounds. Powdered forms of monocalcium phosphate monohydrate (MCPM), brushite, calcium pyrophosphate (Ca Pyro), β tricalcium phosphate (βTCP) and hydroxyapatite (HA) were analysed using the XRF, with sodium polyphosphate (Na Poly) used as a negative control. Signal peaks that corresponded to calcium and phosphate were obtained and presented as a ratio, compared to the atomic ratio of calcium : phosphate (Ca:P) according to their chemical formula. Calcium to phosphate XRF signal ratio correlated strongly with the atomic Ca:P ratio, with an R^2 value of 0.984.

2.3.3 Changing stoichiometry of calcium:phosphate ratios in mineralising cells

The previous data suggests that XRF can be relied upon to give an accurate picture of the elemental makeup of a highly uniform sample. For XRF to be used in mineralisation studies, we must observe it's use in characterising cell culture samples, and the organic, irregular patterns that mineralisation produces *in vitro*.

Murine pre osteoblast MC3T3 cells were cultured as described in the methodology section, and mineralisation induced via the introduction of 10 mM β glycerophosphate and 50 µg/ml L-ascorbic acid. Cultures were characterised using light microscopy (Figure 2.3i), alizarin red (Figure 2.3ii) and ALP activity assays (Figure 2.3iii) twice weekly, until day 21. Visual inspection showed that cells grown in mineralising media displayed dark areas without alizarin red stain at day 14, but significant alizarin red staining at days 17 and 21. MC3T3s grown without the mineralising components (Control) displayed no calcium staining, and a non-mineralising cell type (human dermal fibroblasts (HDFs)), showed no mineralisation, even when β glycerophosphate and L-ascorbic acid were present. Quantification of calcium obtained via alizarin red (AR) assay results (n=5) suggest that calcium deposition occurs gradually across the early time points, until a significant increase at day 17 Mann-Whitney test $p=0.0079$, whilst alkaline phosphatase assay showed continuously increasing activity from day 7. The control cells grown in growth media show very little alizarin red staining, whilst HDF cells grown in mineralising media show a significant lack of alizarin red staining confirming that the mineralisation was a biologically driven process specific to osteoblast-like cells.

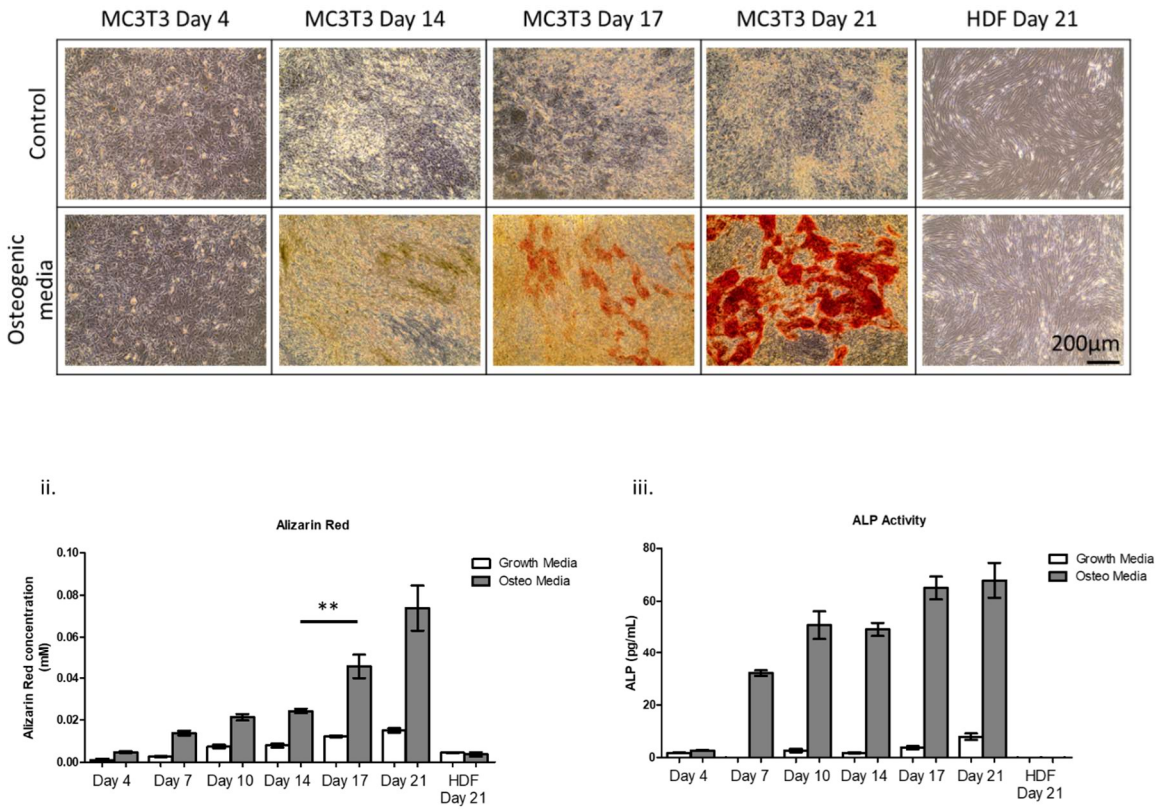

Figure 2.3: Alizarin red and ALP activity assays. (i) Example microscopy images taken at 10x magnification illustrating mineralisation (red stain) of MC3T3 cells grown in osteogenic media at days 17 and 21, and non-mineralisation of negative controls, human dermal fibroblasts (HDFs) and MC3T3s in non-osteogenic media (control). (ii + iii) Alizarin red (AR) assay results (n=5) indicate calcium deposition occurs gradually across the time points in cells grown in osteogenic media, but increases significantly at day 17 (Mann Whitney test p=0.0079). Alizarin red stain is greatly reduced in cells grown in growth media. Alkaline phosphatase activity assay (ALP) shows consistent activity of ALPL through the time points, peaking at days 17-21 quantification of mineralisation status of MC3T3 and HDF cells. ** indicates $p \leq 0.01$.

Following successful mineralisation, cells were fixed using formalin, and n=5 circular disks (9 mm diameter) were cored from the bottom of the cell culture plates for each condition (growth or osteogenic media) and time point (days 4-21), then assessed on the μXRF. All samples were imaged simultaneously to aid comparison and normalisation. A rastering scan obtained XRF spectra from across all samples, acquiring spectra from 1,189,500 pixels, each sized at 100 micrometers, taking 5 milliseconds per pixel, two spectra per pixel due to limits on file size. Mean signal across each disk was calculated for calcium (Figure 2.4i) and phosphorous (Figure 2.4ii) and a ratio obtained (Figure 2.4iii & Table 2.1) for comparison to the calcium phosphate compound standards obtained in Figure 2.2. Detected levels of calcium were extremely low until day 17, whilst detection of a small phosphorous signal at days 7 to 14 are relatively minor when compared to days 17 and 21.

Transforming these calcium and phosphate signals into a Ca:P ratio indicated a marked increase in the later time points (Figure 2.4iii), quantified in Table 2.1 as 0.352 and 0.500 respectively, which, when cross referenced with the standards in Figure 2.2 suggests that the mineral being deposited has an elemental ratio similar to that of one calcium ion to every two phosphorous ions, as seen in monocalcium phosphate monohydrate. This elemental signal taken is an average across the whole cell culture disk, and will include areas of minimal mineralisation, and therefore does not necessarily suggest that the mineral present is MCPM. This data does suggest, however, that the mineral that was deposited within the culture deviated from the stoichiometry that one might expect through the formation of HA. Of note is the increase in the phosphate content of the sample precedes the localised increase in calcium, suggesting a precursor stage. Further work was therefore carried out to characterise the elemental makeup of highly mineralised areas, also referred to as mineral nodules.

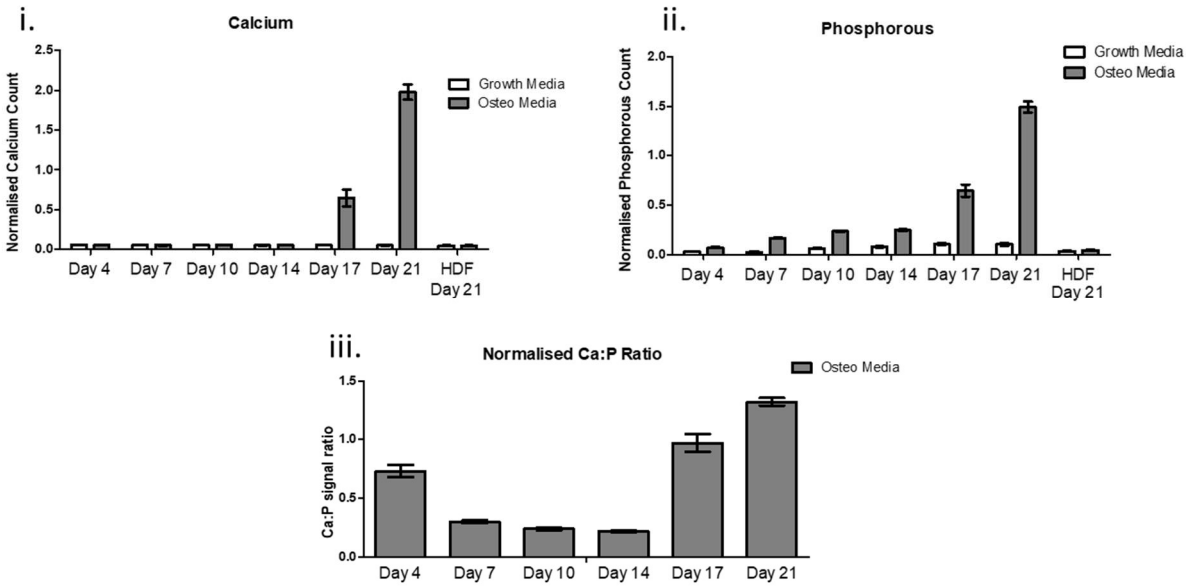

Figure 2.4: Normalised XRF signal for calcium and phosphate levels in mineralising cell cultures. Mean XRF data (n=5) shown in (i) indicate that the majority of calcium deposited by the MC3T3 cells occurred after day 14. (ii) Phosphorous is deposited in small amounts prior to a significant increase post day 17. The changing Ca:P ratio illustrated in (iii) shows that the deposition of calcium is occurring at a greater rate than that of phosphorous in days 17 and 21. This suggests a change in the stoichiometry of the mineral present in the later stages of mineralisation. Only cells grown in osteogenic media displayed significant levels of calcium or phosphate, those in growth media did not.

Time point	Ca:P signal ratio	Extrapolated Ca:P elemental ratio
Day 14	0.218 (±0.008)	0.032168
Day 17	0.972 (±0.075)	0.351727
Day 21	1.322 (±0.033)	0.500064

Table 2.1 Conversion of calcium and phosphate signal ratios to extrapolated elemental ratio. Conversion of the μXRF spectral signal for calcium and phosphate into an extrapolated elemental ratio utilising the relationship discovered in Figure 2.2 suggests that the mineral being formed in these cultures is calcium deficient in the earlier stages, moving towards an increased calcium presence in the final timepoint of 21 days. The figure at day 4 relies upon very low levels of phosphorous and calcium and may not be reliable.

2.3.4 XRF of mineralised cell nodules

Previous measurements have taken the average of the elemental signal across an entire punched disk with a diameter of 9 mm, including cells and extracellular matrix on areas that are not mineralised. Here, we refine our spectral acquisition using light microscopy at 100x zoom, allowing us to obtain five spectra from points that appear mineralised, and five spectra from points that appear non mineralised from a cell culture mineralised for 21 days (Figure 2.5i). By focussing on these individual areas, we can obtain spectra that more accurately represent the mineral being deposited, however it must be noted that even the mineral area spectra will still include signal from extracellular matrix and cells. A series of point scans obtained XRF spectra from five mineralised locations, and five non-mineralised locations, from a single pixel of 5 µm, taking 20 milliseconds per pixel, five spectra per pixel to reduce anomalies.

Signal ratios obtained from these areas are visualised in Figure 2.5ii, whilst signal from a range of biologically important elements are visualised in Figure 2.5iii. These graphs offer a quantification of the stark difference between cellular areas and nodule areas with regards to elemental deposition, with Ca:P ratio significantly increased in the mineralised area when compared using Mann-Whitney testing ($p=0.008$). When compared to data gathered from control HDF cells cultured in mineralising media, HDF cells demonstrate a greater Ca:P ratio than the osteoblast cell area, but less than that of the mineralised nodule. The normalised signal readings detailed in the table in Figure 2.5 iii Indicate that the total amount of Ca and P deposited in HDF cell culture is vastly reduced in comparison to osteoblast culture, and likely not reflective of significant mineral deposition. This ability of benchtop µXRF to differentiate between deposited mineral and non-mineralised areas should prove invaluable in the attempt to clarify the chemistry occurring in the very early stages of mineralisation.

Healthy adult bone consists of approximately 70% hydroxyapatite [136], with an atomic elemental ratio of 1.66, or 5 calcium ions to 3 phosphorous ions. Upon comparison to the Ca:P standard curve created in Figure 2.2, the mineralised area of these mature cell cultures display a signal ratio that correlates with an elemental Ca:P ratio of 0.65, or approximately 2 calcium ions for 3 phosphorous ions (Figure 2.6). This indicates that the area is more calcium dense than pure monocalcium phosphate monohydrate. Further to this, Figure 2.7 plots the Ca:P ratio across a mineral nodule present in a 21

day mineralised culture, where as expected, areas that appear visibly mineralised to light microscopy (100x) have higher Ca:P ratio to that of cellular areas. It appears that calcium increases in relation to phosphorous at areas near the edges of the nodule, in areas that are likely to contain newly formed or forming mineral deposits.

i.

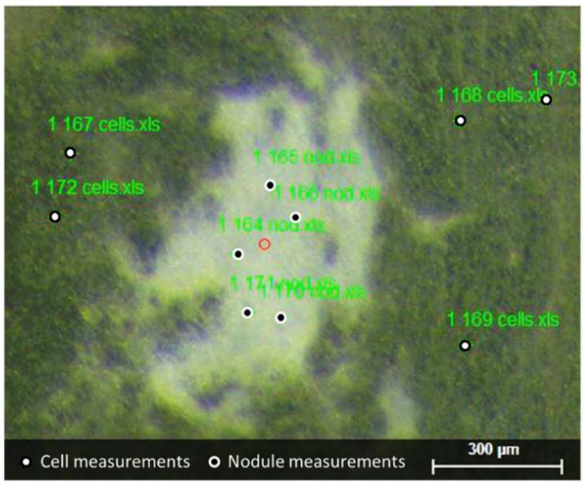

ii.

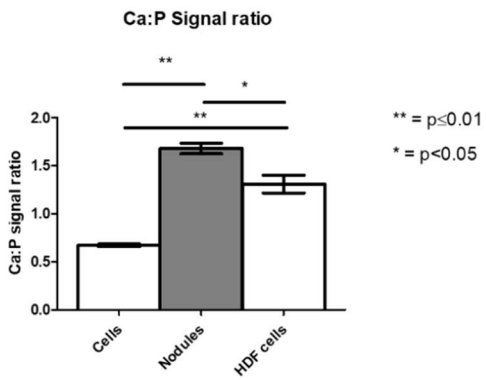

iii.

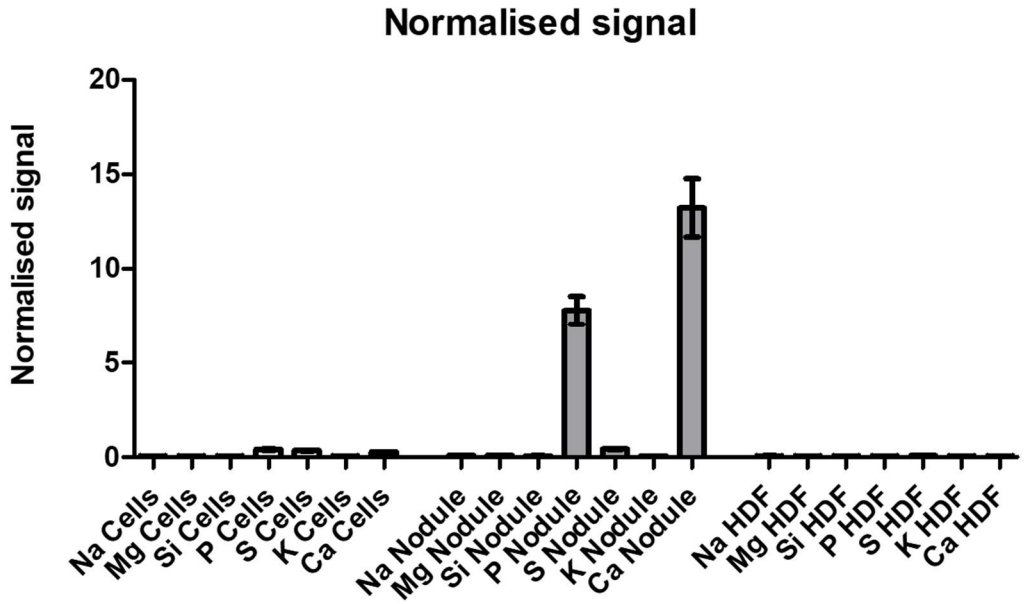

	Na	Mg	Si	P	S	K	Ca1
Cells average	0.06	0.06	0.03	0.40	0.34	0.04	0.27
Nodule average	0.09	0.09	0.07	7.78	0.42	0.06	13.22
HDF average	0.07	0.05	0.02	0.04	0.07	0.05	0.05

Figure 2.5: XRF of visibly mineralised nodules. Image shows a day 21 mineralised osteoblast cell culture nodule (light area) under light microscopy. Five spot measurements were taken within the mineralised area (black spots) and 5 taken in the unmineralised cell area (white spots). Measurements were normalised and calcium : phosphate ratio calculated. These ratios show that the Ca:P signal ratio was significantly greater (Mann Whitney test p=0.008) in the nodule area when compared to the cell area, whilst iii. shows that the calcium and phosphorous levels were also larger in these areas, as expected in mineralisation. Both graphs also include data taken from HDF cells cultured in mineralising media for 21 days (images not shown). These cells demonstrated significantly increased Ca:P ratio compared to unmineralized cell area (Mann Whitney p=0.0079) but significantly lower than mineralised nodule (Mann Whitney p=0.0159). Normalised XRF signal analysis shows reduced Ca and P signal, when compared to both mineralised and unmineralized areas.

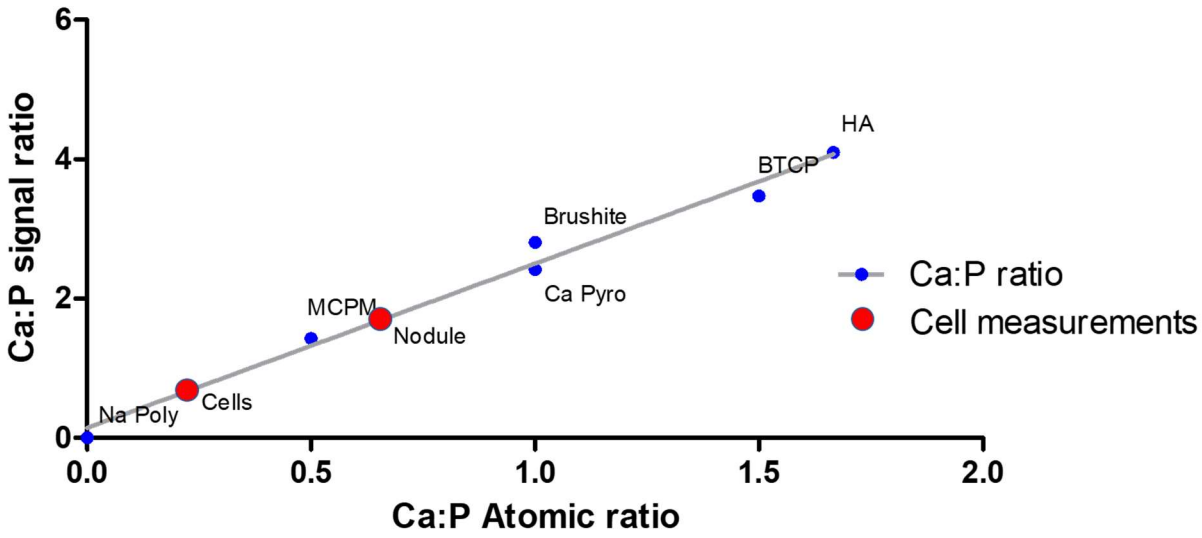

Figure 2.6: Mineralised areas show an increasing Ca:P ratio. The mean Ca:P signal ratio obtained from the cell area (0.67) and the mineralised area (1.68) suggest an elemental atomic ratio of 0.22 and 0.65 respectively (red spots), illustrating a clear change in stoichiometry of the material present, from a less calcium dense to a more calcium dense material, as mineralisation occurs.

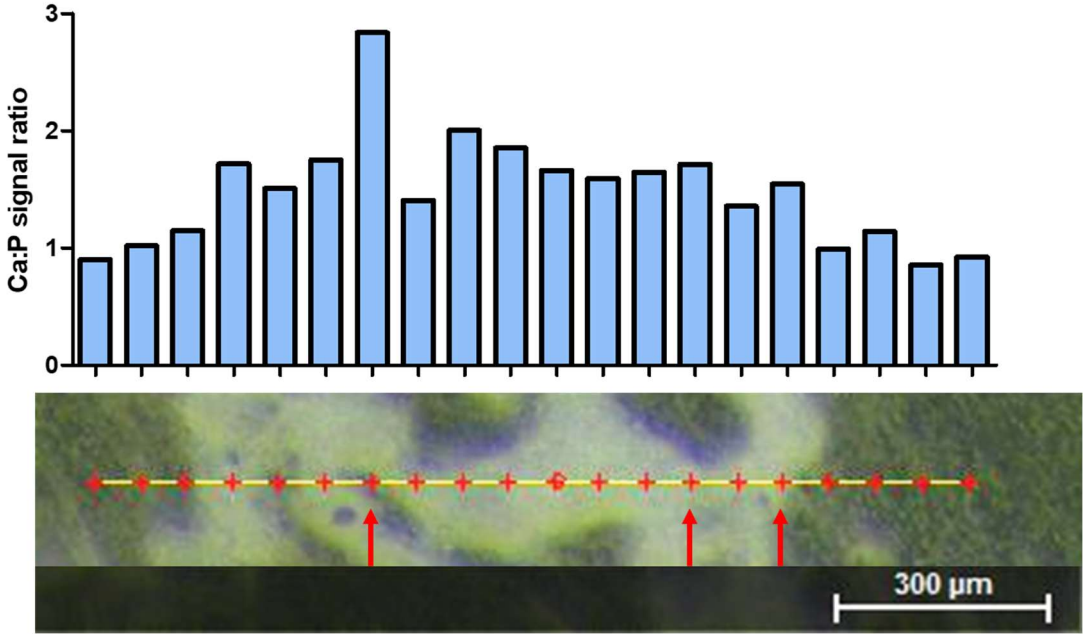

Figure 2.7: Ca:P ratio changes across a nodule. Multipoint scan taken across a mineralising nodule that looked to be partially formed at 21 days. Areas that were visibly mineralised (white areas) displayed increased Ca:P ratio compared to less visibly mineralised areas. There is an apparent increase in Ca:P ratio towards the edges of visible mineral, likely to be the site of youngest mineral. These areas are highlighted with red arrows and show an increased ratio, when compared to the more mature mineral deeper in the nodule. The highest point reached a signal ratio of 2.8, which when converted to elemental ratio, suggests an elemental ratio of 1, similar to brushite, or 1 calcium ion for every 1 phosphorous ion.

2.3.5 MATLAB™ image analysis of nodule number and area

Using the μXRF it is possible to scan an area, obtain thousands of spectra, identify peaks that correspond to specific elements and then use this data to draw an elemental map (Figure 2.8i). These maps can be subjected to further image analysis, offering yet more useful data from cell culture samples that are lost when using more simplistic characterisation techniques such as alizarin red staining. Here we demonstrate the further characterisation of early mineralisation *in vitro* using MATLAB™ (The Mathworks Inc., USA) to calculate the mean area, and total number of nodules formed in our mineralising culture samples.

The samples used in Figure 2.4 were used to provide elemental maps for calcium and phosphorous (Figure2.8i), these maps exported as .png files, and image analysis carried out using Otsu thresholding. In brief, the maps were converted to greyscale, and contrast enhanced to emphasise the difference between high mineral concentration in nodules against background. A subjective cut-off threshold was chosen to differentiate between background and nodule, and following this, individual objects (or mineralised nodules) were quantified and characterised. This was performed on n=5 cell culture samples for mineralised cells at days 17 and 21.

Results visualised in Figure 2.8ii illustrate a larger number of calcium and phosphorous containing nodules witnessed at day 21 when compared to day 17, as well as the significantly larger mean area of said nodules (calcium change day 17 to day 21 Mann Whitney test $p = 0.0079$, phosphorous change day 17 to day 21 Mann Whitney $p = 0.0119$). The increase in nodule area at day 21 suggests a pattern of continued expansion of nodule from focal points, but the increase in nodule number from day 17 to 21 also suggests that new nodule formation is ongoing during the later stages of mineralisation. This methodology shows the usefulness of XRF in early mineralisation characterisation and may be of use in future for assessing the impact of drug treatments on the process of mineralisation.

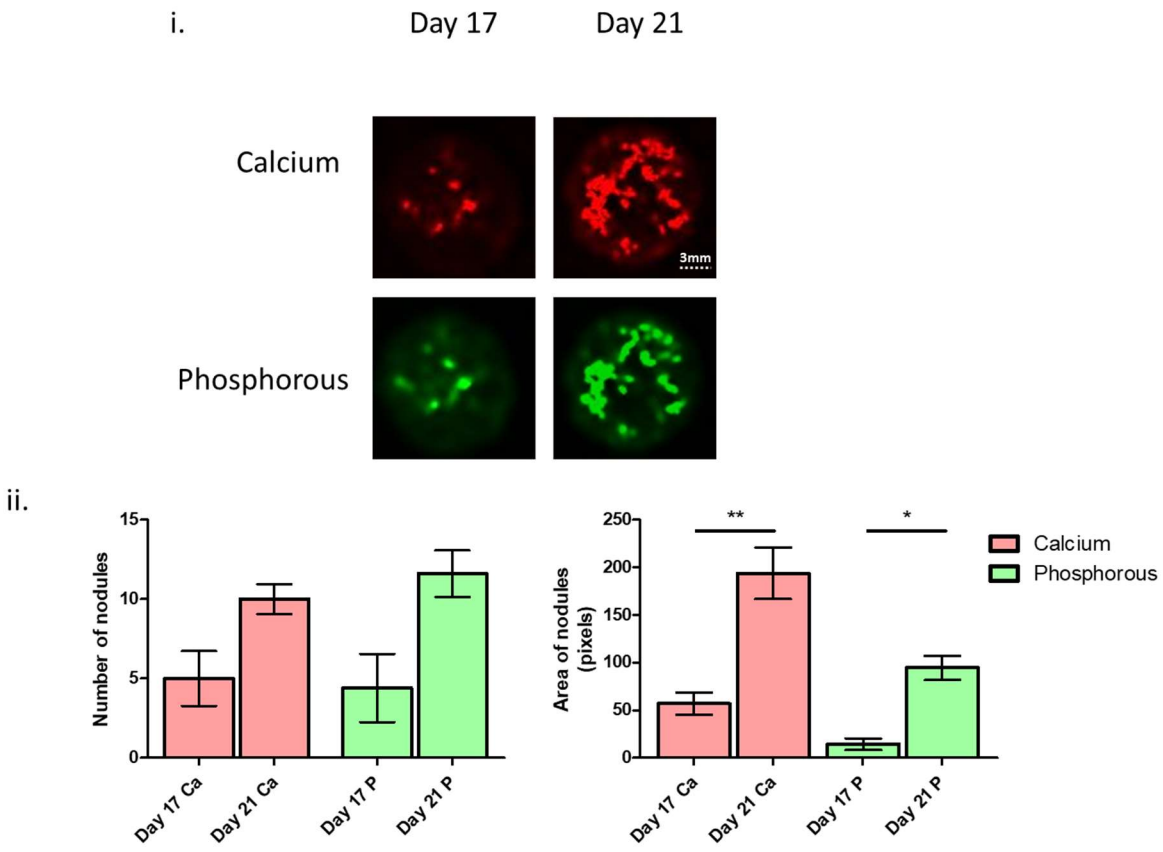

Figure 2.8: MATLAB™ image analysis of nodule number and area. (i) An example of the images produced by XRF analysis of mineralising MC3T3 cell cultures in 48 well plates. For each time point (days 17 and 21), five samples were obtained by punching the bottom out of a 48 well plate, producing a disk 9 mm in diameter. Each disk was scanned using XRF to produce a false colour image detailing elemental presence. Brighter areas represent higher concentrations (nodules) of calcium (red) and phosphorous (green) respectively. These images were imported and processed in MATLAB, quantifying number and area of nodules formed at the different time points (day 17 and 21). (ii) Number and mean area of nodules increased with increasing mineralisation, in similar proportions for both calcium and phosphorous. Increase in nodule area from day 17 to day 21 is significant for both calcium and phosphate, Mann Whitney test $p = 0.0079$ and $p = 0.0119$ for calcium and phosphate respectively. Scale bar is 3mm. ** indicates $p \leq 0.01$. * indicates $p \leq 0.05$.

2.4 Discussion

Establishing the chemistry of early bone formation may be extremely useful in determining the exact processes occurring, and so inform future treatments and research. Here, we show data from benchtop µXRF measurements that suggest it may be an effective tool in interpreting these processes, in specific, cell culture mineralisation *in vitro*. Our work presented in Figure 2.2 shows a strong positive correlation (R^2 = 0.984) between elemental ratio and the µXRF elemental signal spectra, indicating elemental ratio of Ca:P is responsible for 98.4% of the change seen in the µXRF signal ratio. This indicates that the µXRF may be a very useful tool in probing elemental ratios found in unknown samples, providing the sample is suitable for analysis, i.e., dried and fixed, with a relatively flat surface area.

To study stoichiometric changes in mineral across timepoints, it is first necessary to successfully induce mineralisation in our cell lines. The conventional method of assessing mineralisation is to check for differentiation into an osteoblast phenotype via the upregulated expression of ALP, and to assess total mineral deposition via Alizarin red stain assay. The results in Figure 2.3 confirm successful mineralisation of the MC3T3 cell line, with upregulation of ALPL and a marked increase in Alizarin red staining over the baseline non-mineralising cultures. The control HDF cells showed minimal mineralisation, indicating that *in vitro* mineralisation is an active process, guided by osteoblasts, and not simply a passive process caused when increased mineral ions precipitate out of solution in the presence of extracellular matrix.

Analysing these cultures with µXRF showed that detected levels of calcium were extremely low until day 17, this reflects evidence observed via light microscopy (Figure 2.3i) showing absence of alizarin red until day 17. This does, however, conflict with the information obtained in the alizarin red quantification experiment (Figure 2.3ii), which suggested a gradual build-up of calcium across all time points. This may be explained by the rarely discussed ability of alizarin red to interact with additional metallic ions, such as magnesium [137], manganese [138], iron [139], barium and strontium, as per manufacturers information [140]. This information raises the possibility that previous alizarin red detection at earlier time points may not be due to calcium deposition, but increased presence of alternative metallic ions in the developing extracellular matrix. Detection of a small phosphorous signal at days 7 to 14 are small, but larger than that

found at day 4, when coupled with the darker, but not visibly red areas seen in Figure 2.3i Day 14, this may indicate that the darker patches could be caused by accumulation of a phosphorous containing compound. This raises the interesting possibility that these phosphorous ions may be initially bound to the previously mentioned metallic ions, and in turn, produce an alizarin red signal. The ratio of calcium to phosphorous detected by μXRF remains low until the final 2 timepoints assessed, suggesting a deficiency of calcium initially, but increasing to reach a signal ratio high at day 21 of 1.322. When converted this corresponds to an elemental ratio of 1 calcium to 2 phosphate ions, similar to pure monocalcium phosphate monohydrate (signal ratio 1.426), and significantly different to the mineral commonly found in mature mineralised bone, HA (signal ratio 4.098). This may suggest that mineralisation occurs in progressive phases, beginning calcium deficient, and maturing towards HA. It must also be noted that these results do not necessarily suggest that the mineral present consists of a 1:2 Ca:P ratio, as calcium and phosphate may be present but not incorporated into the mineral but into cells or proteins in the extracellular matrix. Taking this analysis from the millimetre scale of cell culture to the micrometer scale, we performed elemental ratio analysis across individual mineralising nodules, measuring approximately 500 μm in diameter. At these locations we observe highly variable elemental ratios, with particular increases in Ca:P ratio near the edges of the nodule, in areas that are likely to contain newly formed or forming mineral. An explanation for this occurrence may be due to the proposed role of ACP in early collagen mineralisation[40]. ACP has been reported to have a Ca:P ratio of 1.50, however this ratio can be altered, going as high as 2.19 when ACP is in the presence of zirconium [141]. Skrtic hypothesises that this alteration may be due to PO_4 forming a soluble complex with zirconium, and subsequently washing away, thus increasing the relative calcium concentration. Whilst zirconium is unlikely to be present in sufficient quantities to affect mineralisation in these cell cultures, it opens the possibility that another ion is performing a similar role. This would connect back to the alizarin red findings in Figure 2.3ii, where we hypothesised that increased stain detection was due to alternative metal ion binding, bearing in mind that an important part of the assay is to dissolve the alizarin red stain. This is not the only possible explanation for these results, not least because this is n=1 data and further replicates must be obtained

before resources are committed to investigate this fully, however, it is an intriguing finding.

It is interesting to relate these findings back to established literature on biological mineralisation. It has been theorised that HA (Ca:P ratio 1.66) may crystallise directly from ACP [32,33] (potential Ca:P ratio 1.5-2.19). The readings observed in the newly forming nodule areas of approximately Ca:P = 1 would not appear to support this theory.

Alternative studies suggest the competing theory that intermediate phases such as brushite ($CaHPO_4 \cdot 2H_2O$, DCPD) and octacalcium phosphate ($Ca_8(HPO_4)_2(PO_4)_4 \cdot 5H_2O$, OCP) with CaP ratios of 1 and 1.33 respectively, occur *in vivo* [35,142]. Work from Bannerman *et al.* [143] map out the kinetically favourable theoretical phase changes from ACP, through the less thermodynamically stable and more soluble phases of DCPD and OCP, before resulting in the final, most stable phase, of HA. These phase changes have been demonstrated *in vitro*, multiple times [144–148], adding weight to the theory that this may be a physiologically relevant pathway for mineralisation in bone. Further support for these transient stages may be found in the remarkable TEM work done by Simon *et al.*[149] who display evidence of OCP interaction with osteocalcin within bone formation sites. Similarly, *ex vivo* minipig mandible studies from Vyalikh *et al.* [150] indicated the presence, using NMR, of ßTCP and DCPD-like structures at sites of earlier stages of bone healing. The presence of these intermediate phases of CaP, with lower Ca:P elemental ratios may offer some explanation for the findings here, where material of Ca:P ratio of 1 and lower was witnessed in newly forming mineral nodule sites.

Regardless, the mineralised nodules investigated in osteoblast cell cultures in this thesis do not display Ca:P ratio similar to the final stage of mineral in mature bone, hydroxyapatite (Ca:P ratio 1.66). Whether this difference in elemental ratio is an indicator of the presence of an intermediate CaP phase, a combination of species, or mature hydroxyapatite crystals alongside non calcium phosphate compounds, such as ATP, or simply an artifact introduced by the weaknesses of this particular methodology cannot be established from this data alone. Further iteration on these methodologies may offer up support for the theories discussed here.

Due to a lack of resolution offered by the current standard method (alizarin red staining) of visualising nodule formation, it is very difficult to reliably automate finer details of mineral deposition, such as whether a treatment results in many smaller sized nodules, or a small number of large nodules. The µXRF provides a potentially valuable avenue towards automating image analysis of culture mineralisation, thanks to the ability to output detailed maps of mineral ion location. Using image analysis scripts, it would be possible for researchers to visualise currently unquantifiable data from current culture techniques.

There are methods that may unlock the locations of calcium and phosphate build up locations. Wolf *et al.* 2017 [151] have demonstrated the ability to locate and identify amorphous granules of calcium and phosphate within mitochondria, using the technique of cryo-scanning transmission electron tomography (CSTET). This technique couples the ability to visualise biological samples at the nano scale, in 3 dimensions, whilst also utilising x ray dispersal to characterise the elemental makeup of the material present. Performing this technique on mineralising osteoblast cultures may reveal valuable insights into the precise location of mineral nodule formation, and therefore how these nodules form in relation to the extracellular matrix.

2.5 Conclusion

This chapter presents evidence for the progressive maturation of mineralised cell cultures from a calcium deficient, phosphorous dense material in early mineralisation, maturing towards an increased calcium presence in later time points. Investigation of defined mature mineral nodules showed increased calcium proportions, but still short of that expected from pure hydroxyapatite, whether this points to intermediate species, or the presence of significant, non-HA phosphorous compound(s) is not yet clear. These data illustrate the effectiveness of µXRF to enhance the amount and quality of data that can be obtained from cell culture experiments and may help to elucidate unresolved questions about the early stages of mineral formation.

Chapter 3 : Raman spectroscopy to probe the composition of bone mineral

3.1 Introduction

Mineralising osteoblast EVs often appear electron dense in TEM images [97] , which can suggest either the presence of molecules containing elements with heavier nuclei, or an increase in binding of the contrast stain. If the theory that EVs are transporters of raw materials essential for mineral deposition is true, the electron dense EVs may indicate a cargo of elements with heavier nuclei such as calcium and phosphorous. As previously discussed, the nucleoside phosphates - ATP, ADP and AMP can have inhibitory or stimulatory effects on various biological activities, such as platelet aggregation [119], mineralisation and TNAP activity [152]. A fine balance of these phosphorous containing compounds is evidently important in the development of bone, potentially impacting the formation of ACP, and subsequent collagen mineralisation. Characterisation and quantification of molecular species present within EVs would be an incredibly useful tool in the understanding of the environment of early mineralisation. It may also offer the possibility of mimicking these conditions more faithfully in cell culture experiments or future therapies.

Raman spectroscopy is an effective, label free method of determining molecules present in samples by detecting the vibrational energies present in covalent bonds, it has been previously used to distinguish between nucleoside phosphates [153]. Originally observed in 1928 [154], Raman spectroscopy is a technique whereby the energy, and thus wavelength of an incident light photon, is altered due to interaction with a molecule. Raman spectroscopy uses a high intensity, single wavelength laser light source to bombard a sample with photons of uniform energy, these photons are absorbed by the target molecules in the sample, and re-emitted with an altered energy, and thus wavelength. When photons are absorbed by molecules, this distorts the electron cloud surrounding the nuclei, forming a short lived ‘virtual state’ which is unstable, causing the photon to be re-emitted almost immediately. The energy lost in this process is extremely small, due to the very low weight of an electron, therefore this process is known as elastic or Rayleigh scattering. A small proportion [155], approximately 1 in 10^6–10^8 of the incident photons will transfer some energy to the nucleus, resulting in

promotion to a higher vibrational state. As nuclei are considerably heavier than electrons, the energy of the emitted photon is significantly altered, known as inelastic or Stokes Raman scattering (Figure 3.1).

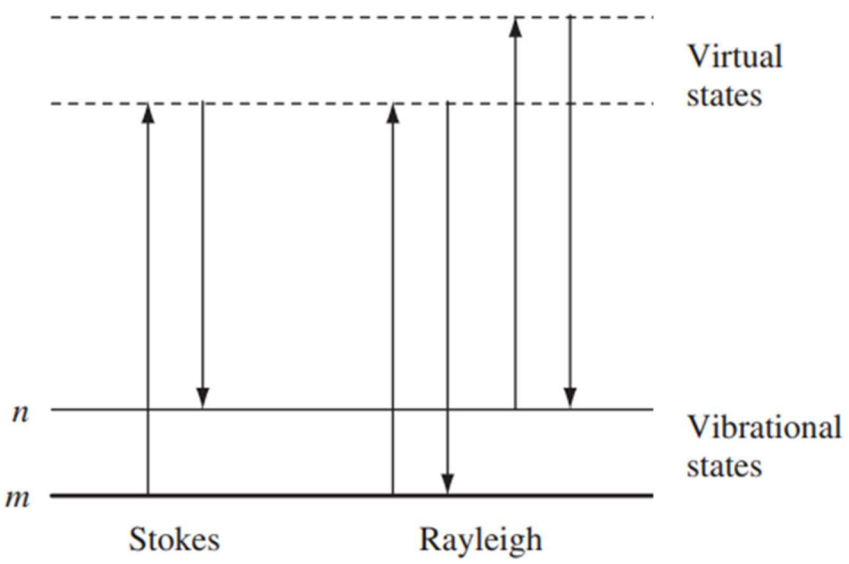

Figure 3.1: Diagram of Rayleigh and Raman scattering processes in Raman spectroscopy. The baseline energy vibrational state *m* represents the lowest energy state of the nucleus, with possible increased vibrational energy state at *n*. Incoming photons impart energy (up arrows) causing the nucleus to enter an unstable virtual state much higher than the more stable vibrational states. To return to a stable state, energy is shed in the form of a photon (down arrow). Rayleigh scattering is the most common method to do this, and results in emission of a nearly identical energy photon to that which entered. Rarely, some energy will be transferred the nucleus, and upon exiting the virtual state it returns to a higher vibrational state than it began with, creating motion, and the emitted photon is therefore of a lower energy, a process known as Stokes Raman scattering. Figure adapted from Modern Raman Spectroscopy – A Practical Approach. Smith and Dent, 2019 [155].

The higher vibrational state occupied by the molecule causes nuclear motion, depending on the number of atoms and the respective chemical bonds present in the molecule, the energy absorbed to induce this motion is predictable. This predictable energy requirement means that individual molecules have a reliable Raman spectrum 'fingerprint', allowing Raman spectroscopy to be used to identify the presence of certain molecules, and the bonds they form. Though Raman scattering is a rare occurrence, the ability of modern equipment to deliver high photon densities, modern spectrometers to detect and resolve small changes in wavelength, and effective filters to ignore Rayleigh scattering make this possible. Raman spectroscopy measures the change in energy across the incoming and outgoing photon, referred to as Δ cm^{-1}, typically referred to by the field as cm^{-1} for ease.

In this chapter, we detail the investigation into the sensitivity of Raman spectroscopy for the principal covalent bonds present in bone. To achieve this, we first produced progressively demineralised bone samples, and then performed several characterisation techniques, including ashing, Raman spectroscopy, XRF and thermogravimetric analysis (TGA). Finally, these characterisation methods were compared.

3.2 Methodology

3.2.1 Demineralisation

Human bone sections of approximately 1 cm^3 containing both trabecular and cortical bone types were removed from a donated human tibial plateau (Ethics Reference Number 11/ES/1044) using bone rongeurs. These sections were then additionally trimmed to within 0.1 g of each other. Sheep bone sections were taken from sheep tibia in 1 cm x 2 cm cylinders, these sections were washed in water for 5 minutes at room temperature to reduce excess non-bony tissues and fats as much as possible. Sections were then incubated for 0, 2, 7, 14, 21 or 28 days, in 10% EDTA in PBS at 4 °C, constantly stirred on a roller, as per Greenbaum *et al.* [156]. Following this, excess EDTA was removed by blotting and washing for 5 minutes in distilled H_2O, bone tissue weighed, then stored at -20 °C for further examination.

3.2.2 Bone powdering

Bone tissue was cooled then milled to a fine powder using liquid nitrogen and a SPEX SamplePrep Freezer/Mill 6770 (New Jersey, USA) as per manufacturer's instructions, and returned to -80 °C storage until further use.

3.2.3 Raman spectroscopy - Powdered bone

Raman spectroscopy was carried out on demineralised, powdered human bone using an inVia Renishaw Qontor Confocal Raman microscope (Renishaw plc., UK) using a 785 nm laser in the main fingerprint region of 700-1700 cm^{-1} centred around 1200 cm^{-1}, at 100% power for 1 second, with 10 accumulations per point, and a mean obtained, to improve signal:noise ratio. Multiple spectra were taken from different locations from a single, flattened powder sample, at each location the mean of 25 measurements across a 10 μm^2 grid were taken. Background signal was removed, intensities normalized, mean obtained, data was then normalised against phenylalanine, a common amino acid found in protein. Peak intensities and wavenumbers were identified using the data cursor in the WiRE software (Renishaw plc, UK).

3.2.4 Ashing

Human bone samples were weighed before ashing in a heatproof crucible, using a Carbolite CWF 1300 furnace (Carbolite Gero, USA), by heating at 10 °C per minute to a maximum of 600 °C, for a period of 13 hours. Powdered mineral was collected and weighed again, post ashing, before being characterised.

3.2.5 Micro-XRF

Maps of elemental composition across various sample types were acquired using a Tornado M4 micro-XRF system (Bruker Nano, Germany) fitted with a Rhodium micro focus X-Ray tube and a polycapillary lens, with the X-ray tube set to 50 kV voltage and 200 µA current. The chamber pressure was lowered to 20 mbar to maximise sensitivity of signal. The system was programmed to acquire a map across the sample by rastering the microfocus beam over the slide with a pixel size of 20 µm and a time per pixel of 10 ms. An XRF spectrum was collected at each pixel and elemental maps generated progressively in real time, creating an image where pixel intensity represented X-Ray detector pulses per eV at each measurement point on the sample. Intensities were normalised to rhodium peaks to allow comparison between samples.

3.2.6 Thermogravimetric Analysis

20 mg of powdered sheep bone sample was inserted to the carousel of a TA Instruments Discovery TGA (Delaware, USA) heated at 10 °C per minute up to 600 °C, and sensitive weight measurements were taken every 10 seconds.

3.2.7 Statistics

All statistical analysis was performed using GraphPad Prism version 5.03 for Windows, GraphPad Software, San Diego California USA, www.graphpad.com.

3.3 Results

3.3.1 Raman signal from powdered, demineralised sheep tibia

Samples of bone taken from donated human tissue were demineralised as per methodology section for multiple time points between 0 and 28 days. The intensity at wavenumber 960 cm^{-1}, which corresponds to PO_4^{3-} ion bond stretching [157,158] was increased at day 0, indicating presence of phosphate bonds, likely hydroxyapatite, and this intensity was reduced until very little signal remained at day 28 (Figure 3.2 & 3.3). The signal at 1064 cm^{-1} corresponds to CO_3^{2-} ion bond stretching [159,160], was also higher at day 0 than any other time point, suggesting this too was removed during the CLARITY process. The assignment for the hydroxyproline band found in the ubiquitous bone protein collagen (876 cm^{-1}) [161] was consistent across timepoints, as expected, due to the normalisation against another protein assignment, phenylalanine, with the exception of day 4, suggesting an anomaly at this timepoint. Further inspection of the raw spectra shows that day 4 had a very large phenylalanine signal, reasons for this are unclear.

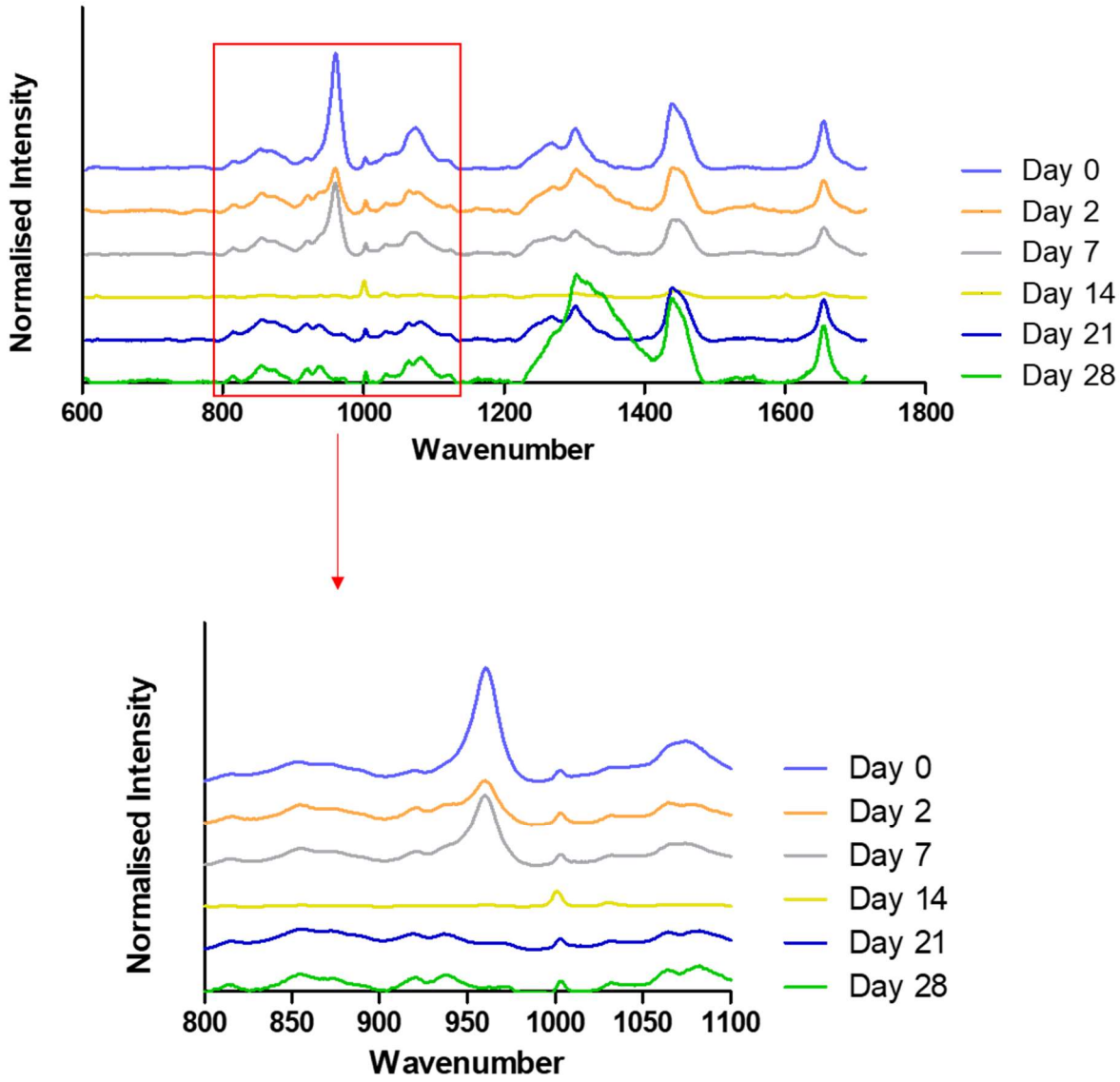

Figure 3.2: Raman spectra of human bone demineralised for up to 28 days. The Raman spectra for demineralised powdered bone samples, with a focus on the regions relevant to bone mineral, CO_3^{2-} carbonate ion bond stretching (1064 cm^{-1}) and PO_4^{3-} phosphate ion bond stretching (960 cm^{-1}). The presence of phosphate is significantly greater at baseline (day 0), and reduces with further exposure to demineralisation, appearing absent at day 21. Carbonate signal is greatest at day 0 before reducing following demineralisation.

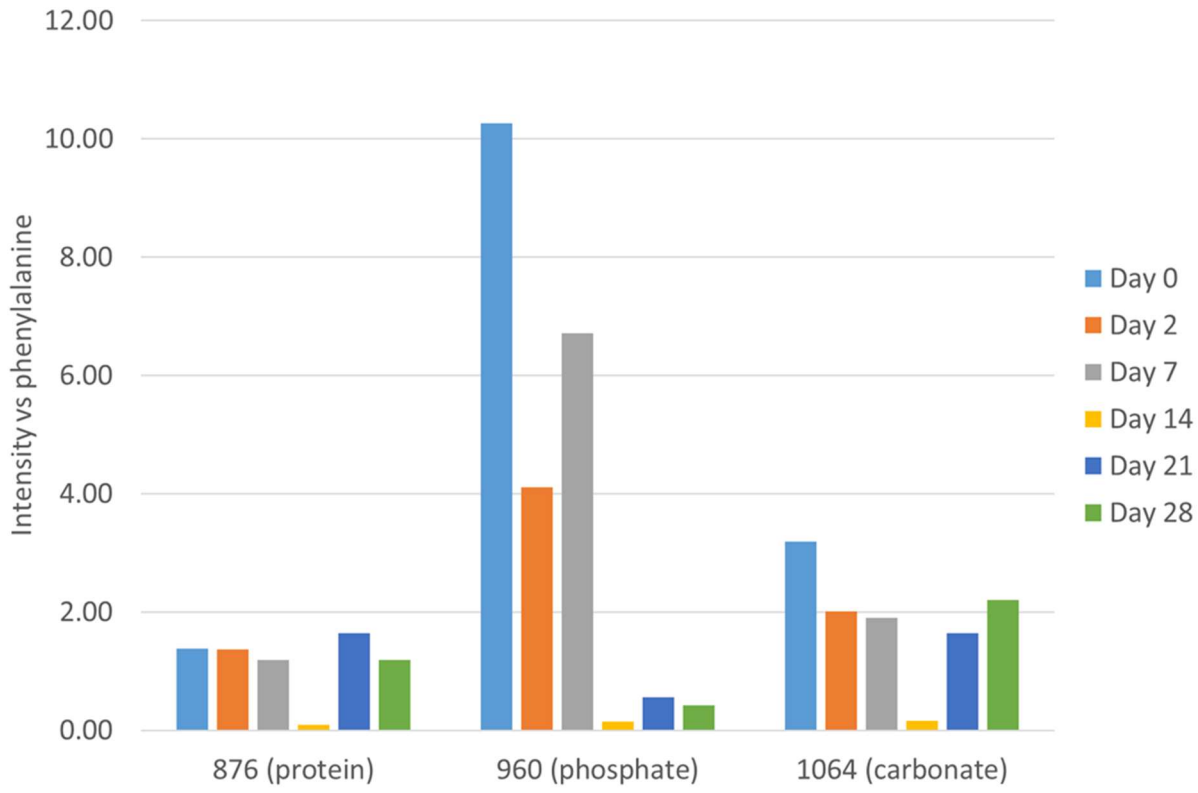

Figure 3.3: Raman from human powdered bone. Raman signal corresponding to protein (876 cm^{-1}) remains consistent across time points (excepting Day 14 which appears anomalous), phosphate reduces in a time dependent manner whilst carbonate appears to be absent by day 2, suggesting rapid removal by demineralisation media. Raman signal intensity was normalised to phenylalanine peak (1003 cm^{-1}) as this should remain consistent regardless of demineralisation status but appears anomalous at day 14.

3.3.2 Mass loss from human bone after demineralisation and ashing

The results presented in Figure 3.3 suggest that mineral was present in decreasing proportion as time increased, one method of confirming this was to assess total remaining inorganic mass, which would be done by ashing the samples (see methodology). The above samples were weighed, ashed, and re-weighed. Ashing involved incinerating the bone samples at 600 °C for 13 hours and had the effect of burning away organic matter such as lipid and protein, leaving only the inorganic mineral. These results, indicated visually in Figure 3.4 and graphically in Figure 3.5, indicated no mineral remaining at day 21, further supporting data obtained by Raman spectroscopy (Figure 3.3).

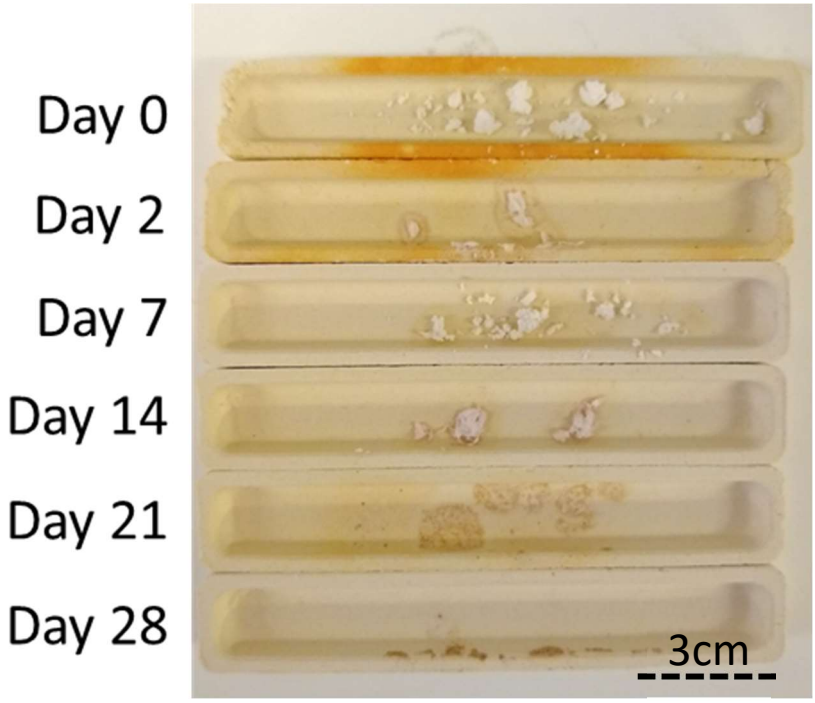

Figure 3.4: Remains of human bone sample post demineralisation and ashing. Image shows ceramic crucibles containing remaining inorganic component of demineralised bone samples following the ashing process, which involved heating at 10 °C per minute to a maximum of 600 °C, for a period of 13 hours.

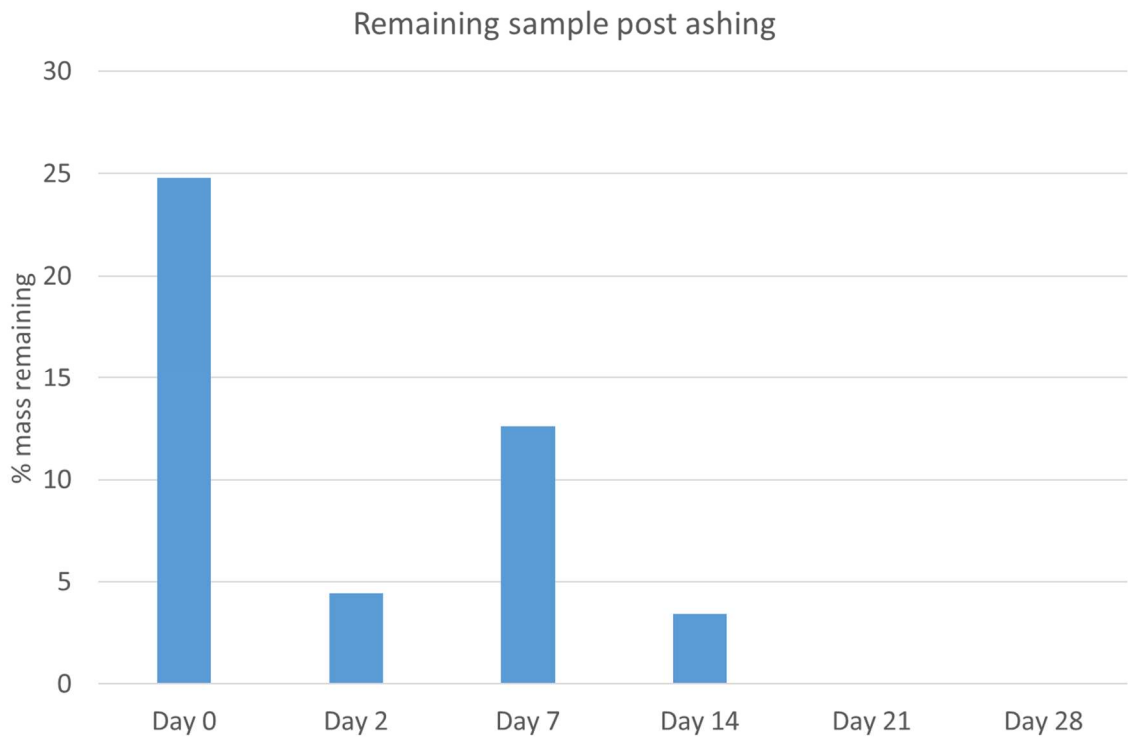

Figure 3.5: Mass remaining of demineralised human bone samples. Proportion of mass remaining following the ashing of bone samples which had been demineralised for up to 28 days. n=1 per time point. No sample remained following 21 days of demineralisation.

3.3.3 Correlation between Raman phosphate signal and mineral mass remaining post ashing

To assess whether Raman signal intensity correlates with the amount of mineral in a sample, the Raman signal peak associated with phosphate stretching (960 cm^{-1}) was normalised to phenylalanine, and plotted against the weight of the remaining mineral present in the sample (Figure 3.6). Whilst the data shows a trend of phosphate signal increasing with mineral proportion of the sample (R^2 = 0.956), it does not appear to increase proportionally. Potential reasons for this may be due to inaccuracies of measurement, as these bone samples were very small (0.36-0.55 g) due to limited source material, these small samples had variable surface area exposed to demineralisation solution, potentially affecting the rate of demineralisation. Additionally, these measurements were from n=1 bone sample. Further experiments utilising larger bone samples, and sample numbers, were needed to establish a more reliable relationship between the two measurements.

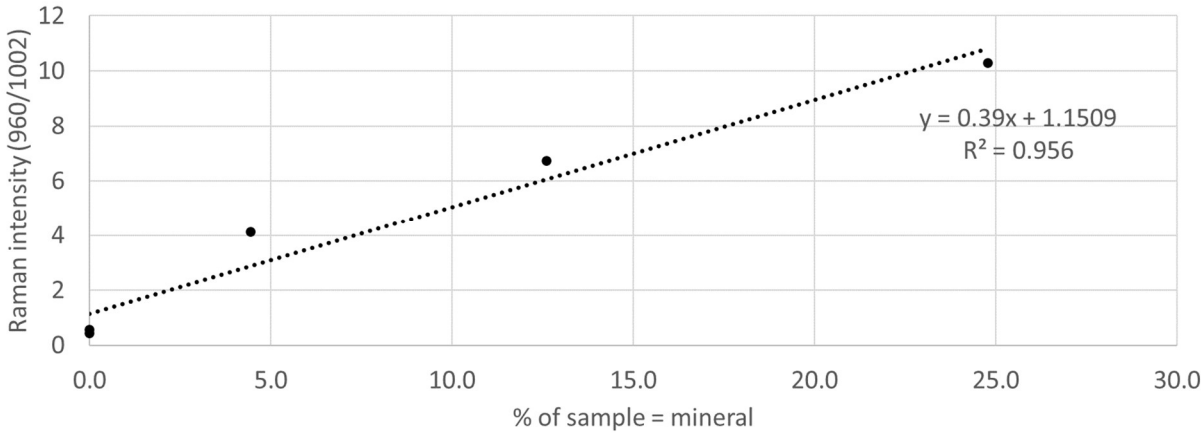

Figure 3.6: Relationship between mass remaining and Raman signal. Raman spectral intensity at the wavenumber corresponding to phosphate present in the sample (960/1002) plotted against mineral remaining in the sample assessed by ashing. Results show a correlation with increasing signal corresponding with increased mineral presence, however, increase does not appear proportional.

3.3.4 Characterisation of larger bone samples

Whilst Figure 3.6 showed a correlation between Raman signal intensity and mineral remaining in sample, small tissue sample size and uncontrolled surface area/volume ratio may have been responsible for the anomalous result seen at day 14. A further refinement of the experiment was therefore undertaken. Demineralisation was repeated over 28 days with significantly larger bone samples, three samples per time point weighing between 1.7 and 3.4 g, of more consistent shape, and therefore surface area/volume ratio, consisting of the cortical bone from sheep tibia. These samples were again demineralised as described previously, and then interrogated using Raman spectroscopy (Figure 3.7) and μXRF (Figure 3.8) as per methods section. The Raman spectra obtained at each time point showed a decreasing phosphate signal correlating with increased time of demineralisation. Whilst this trend appears consistent, it is statistically non-significant, as variability (standard error) increases as signal intensity decreased. μXRF measurements were taken from the same bone samples, with signal for calcium and phosphorous obtained relative to rhodium, as per previous work in Chapter 2 (Figure 2.4). These results also suggest a time-based decrease in mineral presence, with calcium and phosphorous signals falling by >50% (calcium Day 0 92.6 (±1.639) arbitrary units (A.U.), Day 14 45.9 (±0.8) A.U.) over the first 14 days, after which, decline in signal was greatly reduced. Variability in the XRF results appears much less in comparison to that seen in Raman.

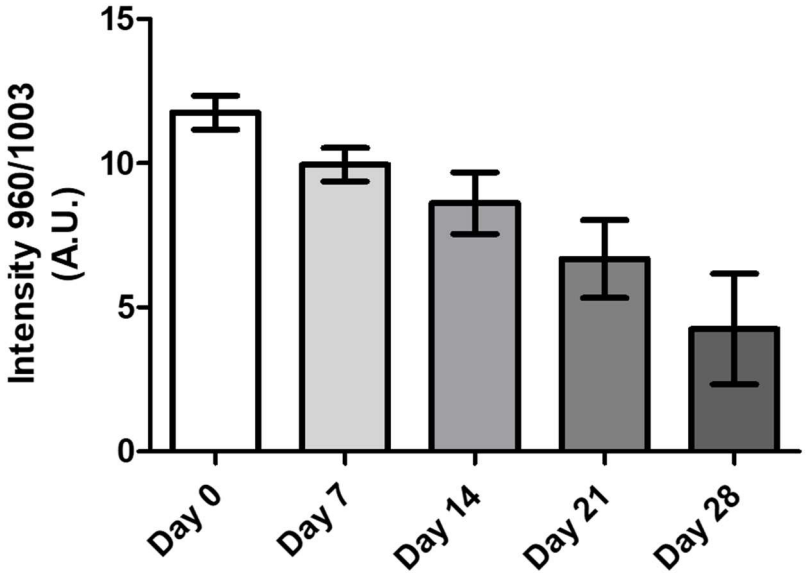

Figure 3.7: Raman spectroscopy characterisation of phosphate bond vibration in demineralised, powdered sheep bone sample. Sheep tibia samples were demineralised for up to 28 days. Samples were then milled to a fine powder and interrogated using Raman spectroscopy. Mean spectra were taken from 5x5 grid pattern, from n=3 samples. Raman signal intensity corresponding to phosphate P-O bond stretching at wavenumber 960 cm^{-1}, normalised to phenylalanine (1003 cm^{-1}) were obtained, mean and standard error plotted.

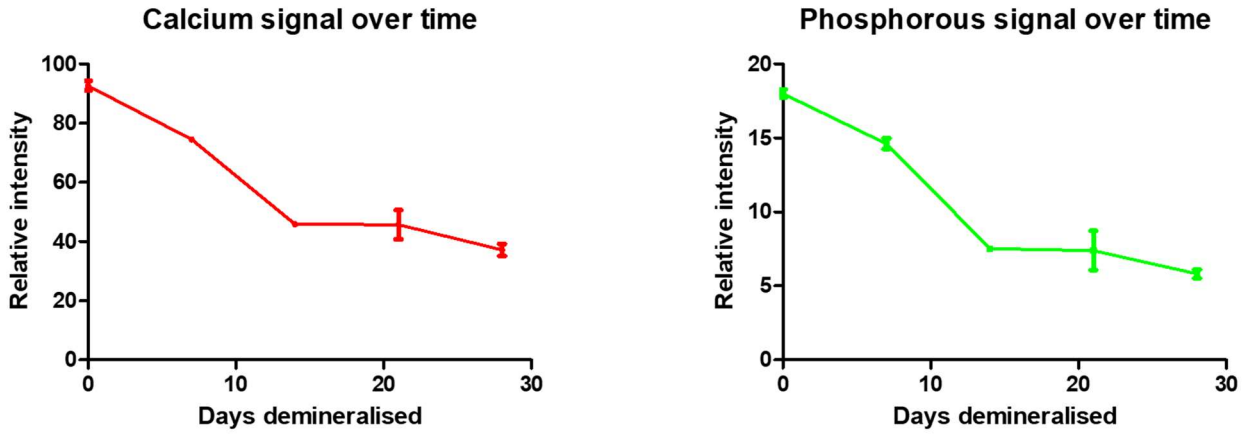

Figure 3.8: µXRF from powdered sheep bone. At each timepoint, n=3 µXRF scans showed reduced calcium and phosphorous signal as time progresses, with strongest loss in initial 14 days. The trend of reduction in calcium and phosphorous signals were very closely linked.

3.3.5 Thermogravimetric analysis of demineralised and powdered sheep bone

Ashing and manual weighing of bone samples is a method that is better suited to larger samples, where inaccuracies in weighing samples have less of an impact. Thermogravimetric analysis is a more sensitive measurement process, offering insight into the organic makeup of the sample. Twenty milligrams of each sample of demineralised sheep tibia characterised in Figure 3.7 and Figure 3.8, was heated at 10 °C per minute up to 600 °C, with weight measured every 10 seconds. All samples show a similar rate of weight loss in the initial 0-150 °C range, indicative of water evaporation [162] . Little loss occurs between 150-250 °C, after which a notable reduction in weight is observed, linked to the combustion of organic components. It is at this point that major deviation occurs between the demineralised samples, with the samples exposed to EDTA for the shortest time (0 and 7 days) displaying a substantially smaller loss in total mass compared to those exposed for the longest times (14-28 days). Beyond 450 °C the rate of mass loss is reduced for all time points, as most organic components have been removed (Figure 3.9). Mean total mass remaining for the time points were as follows; Day 0 = 70.3%, Day 7 = 67.2%, Day 14 = 53.3%, Day 21 = 48.2%, Day 28 = 50.3%.

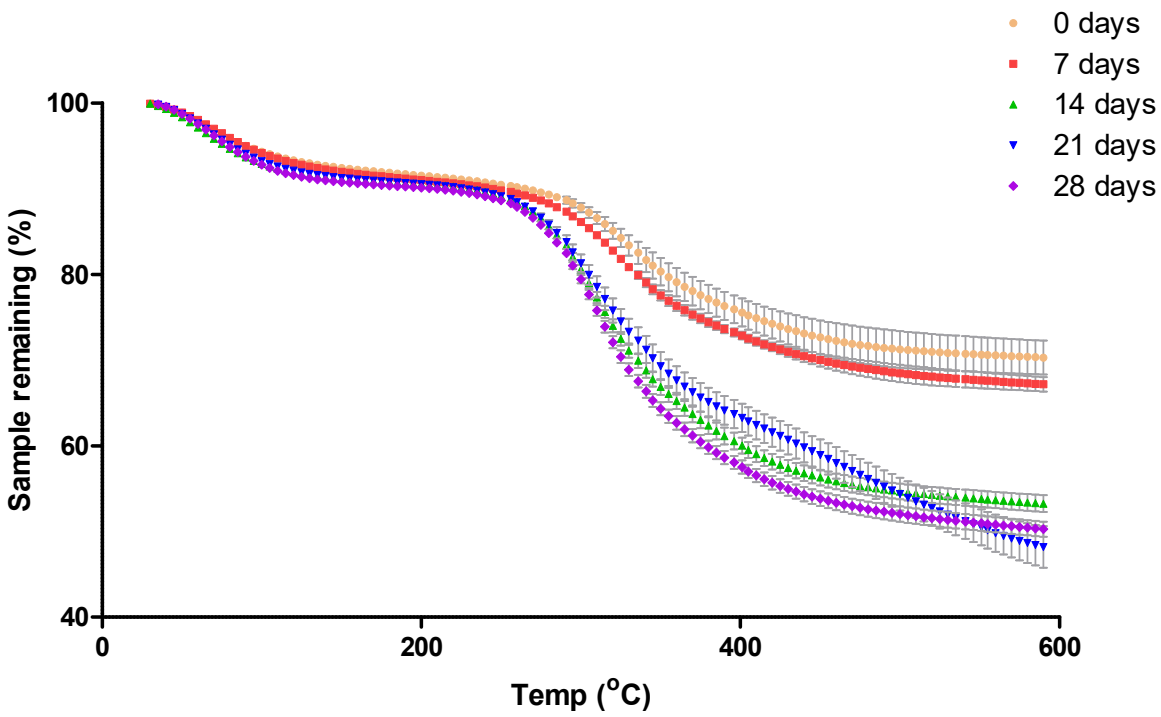

	Day 0	Day 7	Day 14	Day 21	Day 28
Final mass remaining	70.3% (±1.97)	67.2% (±0.83)	53.3% (±0.98)	48.2% (±2.43)	50.3% (±0.89)

Figure 3.9: Thermogravimetric analysis of sheep bone. Thermogravimetric analysis of sheep tibia demineralised between 0-28 days, 0 & 7 days have a greater amount of mass remaining (70.3% and 67.2% respectively) after heating to 600°C, when compared with Day 14 (53.3%), Day 21 (48.2%) and Day 28 (50.3%) consistent with increased demineralisation with extended exposure to demineralising conditions.

3.3.6 Correlation of thermogravimetric analysis with Raman Spectroscopy and μXRF

With data obtained for the mineral detected at each timepoint by Raman spectroscopy (Figure 3.7) and XRF (Figure 3.8), determination of the correlation of these two detection methods with remaining mass of incombustible mineral remaining as per TGA analysis (Figure 3.9), would provide important information on their utility in the quantification of mineral. Quantifying the correlation between the detection methods and the mass remaining was done by calculating the goodness of fit between the mass remaining and the mineral detected, this can be seen in Figure 3.10. These results show that the Raman spectroscopy method of detecting phosphate (Intensity at wavenumber 960 cm^{-1}) correlates poorly with the total mass remaining ($R^2 = 0.53$) (Figure 3.10.i). Calcium x ray fluorescence signal, however, provides a much more reliable indicator of total mass remaining, correlating well ($R^2 = 0.90$) (Figure 3.10.ii). An R^2 of 0.53 indicates that 47% of the variability in the Raman spectroscopy data cannot be explained by the total mass remaining, illustrating that mineral remaining is not tightly linked to Raman signal, and other variables are having a significant effect on the Raman signals detected. This methodology of Raman spectroscopy is therefore unlikely to be a robust indicator of mineral remaining, as the sensitivity of the Raman signal to mass remaining is poor.

Comparison of the Raman intensity with XRF detection of calcium signal (Figure 3.10.iii), produces an R^2 of 0.58. This suggests the two techniques do not correlate well, and that detection of phosphate by Raman spectroscopy, and calcium signal by XRF, are not closely linked, when using the methodologies employed here.

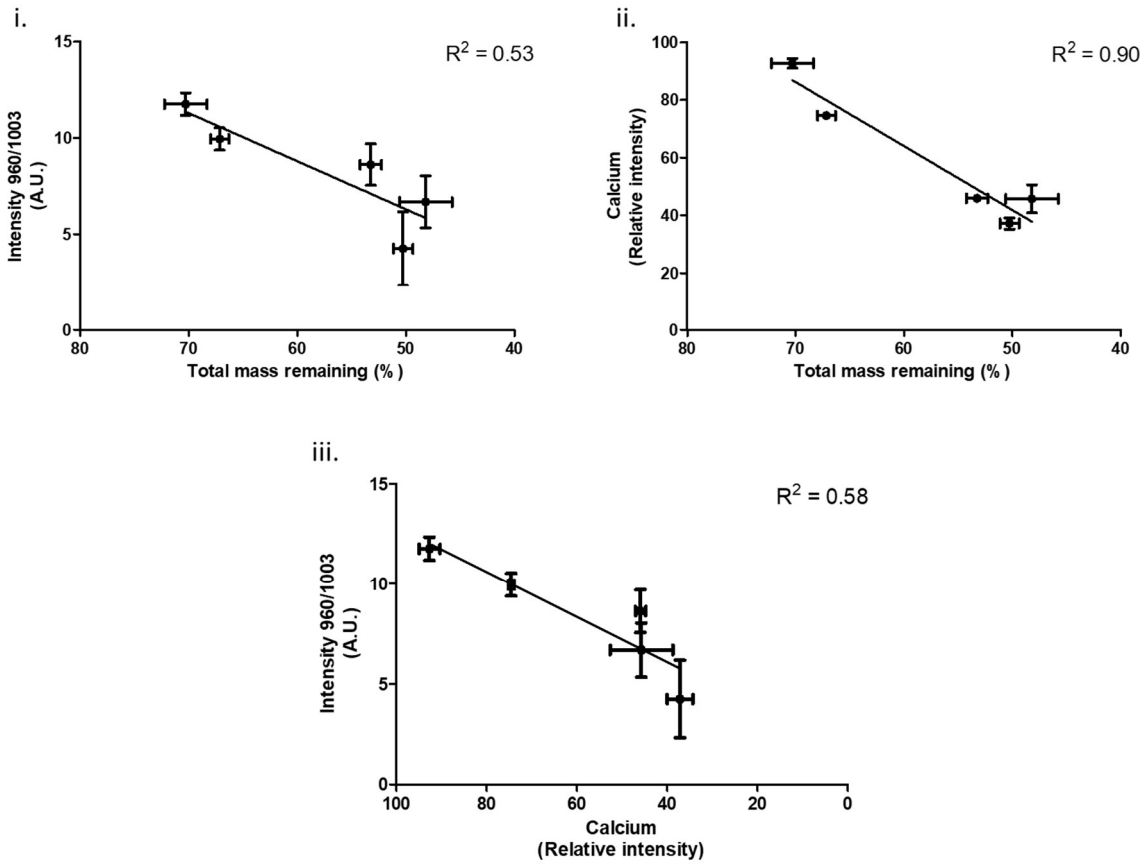

Figure 3.10: Correlation between mass remaining after demineralisation and mineral detected using Raman spectroscopy or µXRF. Mass remaining once organic matter has been combusted in demineralised sheep bone samples (x axis) plotted against mineral component detection using (i) Raman spectroscopy and (ii) µXRF on y axis. Whilst mineral detected by both Raman spectroscopy and µXRF appear to correlate somewhat with findings from TGA, the reduced variability in the XRF readings offers an increased goodness of fit, whereas the large variability in the Raman intensities indicates a poor fit. Results in iii. show a poor correlation between Raman signal and XRF signal, suggesting that the XRF signal is a poor predictor of Raman signal.

3.4 Discussion

Validating μXRF and Raman spectroscopy as new methods of assessing biological samples for mineral quantification required trial and error processes. Initial attempts at this (Figure 3.3) involved small sections of donated human bone, however it soon became clear that these samples were too small, lacking uniformity, and consisting mainly of trabecular bone, which, being porous and less dense, demineralised extremely quickly. Two samples, demineralised for 2 and 14 days, which were initially the smallest samples, appeared to have a faster rate of demineralisation, likely due to increased penetration of the sample. Phosphate P-O bond stretching at 960 cm^{-1} looked to be a useful barometer of demineralisation, to be expected considering the calcium phosphate compound hydroxyapatite makes up 70% of mature bone. Carbonate stretching peaks at 1064 cm^{-1} looked to have much less utility, with low starting intensity and rapid removal during demineralisation.

These results were not intended to be a validation of the demineralisation process however, but to investigate the ability of Raman spectroscopy to determine mineral levels within powdered samples. Ashing these samples left mineral weights that correlated very well with the Raman spectra obtained from Figure 3.5 (R^2 of 0.956) (Figure 3.6), however, this was taken from single bone samples at each time point and needed to be repeated to obtain robust data.

To solve this, larger samples were obtained from the shaft of a sheep tibia, which were far more uniform in shape, and consisted almost entirely of dense, cortical bone. Characterisation of these samples with Raman (Figure 3.7) revealed a regular decrease in phosphate intensity albeit with large variability in the later samples. One reason for this is likely to be that Raman spectroscopy requires the target samples to be within a small focal volume of the laser, offering great resolution, but difficulty handling uneven surfaces and non-homogeneous samples. Despite extensive milling, the powdered bone was not fine enough to offer a smooth surface on the micrometre scale used in Raman microscopy. This introduces a potentially confounding factor, the uneven surface prevented map scanning over large areas, necessitating smaller maps over only 10 μm^2 and likely from a single granule of powdered bone. As the samples were not totally demineralised (maximum 48.2%, Figure 3.9) at any time point, those from the later time points were more likely to have extremes of demineralisation, from highly

demineralised on the surface, to more mineralised deeper within the cortical bone. Therefore, in choosing three separate areas (and likely 3 distinct powdered bone granules) there is likely to be more disparity between these three maps, and therefore more variability. Potential solutions for this problem include; using a different powdering method to create a finer powder from the bone samples, or take a much larger number of spectra from different points, requiring much more time, or to use an autofocussing routine to scan larger areas, however, the autofocussing routine was considered unreliable on the machinery available. These issues may suggest that the sensitivity of Raman spectroscopy to poor focussing may mean it is unsuitable for interrogating objects as small as EVs, however, this may be mitigated by utilising optical tweezers focussed within the same focal volume as the Raman laser.

Conversely, μXRF is designed for larger subject matter, and does not work on such highly resolved scales as Raman spectroscopy, with a much larger focal volume, and so is unaffected by small changes in height of samples. The spectra obtained from μXRF (Figure 3.8) indicated a 50% reduction in calcium over 14 days (calcium and phosphorous rates of removal were almost identical) after which rate of demineralisation rates dropped sharply. This may have been due to the inability of demineralisation fluid to penetrate fully into the dense cortical bone and failing to remove calcium and phosphorous embedded there. Variability was significantly reduced compared to Raman at all time points, again, likely due to the reduced impact of the uneven surface on the ability of μXRF to obtain spectra, allowing a larger area of the sample to be scanned. Additionally, the speed at which μXRF collects spectral information allowed the collection of up to 15,000-point spectra, across an area spanning 2 mm^2, reducing the impact of heterogeneity in the samples.

The mineral mass remaining estimated by TGA (Figure 3.10) correlate closely with results obtained by μXRF (R^2 = 0.90) but poorly compared with Raman (R^2 = 0.53), suggesting that μXRF may be more suitable for large scale mineral quantification as performed here, but the variability displayed by Raman spectroscopy indicates inaccuracy.

Variability (standard error) is significant in the Raman readings, and is likely to impact the sensitivity and reliability of these methods, whilst standard error is much reduced

in the XRF data. A likely source of this error may be due to the number of measurements taken with each method, XRF is a highly automated process, in which approximately 22,500 readings are taken across a 3 mm^2 sample size, however, using equipment available, it was not possible to automate the Raman spectroscopy methodology, and only 25 readings were performed across a 25 μm^2 location. The method of bone powdering (freezer mill) produces a fine powder, however, at the magnification used in Raman spectroscopy, significant topography changes are still seen. This resulted in imperfect focussing of the Raman laser on the sample being interrogated, potentially increasing anomalous results. Raman spectroscopy, due to its nature, is more susceptible to imperfect sample focus, as material not within the focal volume of the laser will be subject to significantly reduced energy, affecting the energies emitted by chemical bonds within.

It is possible that additional measurements may reduce variability, and increase accuracy. One unusual result from this method is the assessment that demineralising for 21 days removed more non-organic material than did 28 days, however, this difference was not significant (Mann Whitney test p=0.7).

The correlation between XRF signal and Raman signal produces an R^2 of 0.58 (Figure 3.10.iii. This figure suggests that the variability in the Raman signal is poorly correlated with XRF signal. This may be because the preparation method undertaken with these bone samples is more compatible with XRF detection, which works at larger scales (millimeter sized samples), than with Raman, which works at much smaller scales (typically micrometer sized). It is important to use techniques suited to the samples available, XRF appears robust when used on larger samples, but will be unsuitable for use directly on nanoparticles such as EVs, or samples in liquid suspension. Raman spectroscopy was unfortunately unsuited for use on samples prepared in this manner. It may however prove useful on samples with significantly less topographical variation, or large-scale heterogeneity on the macro scale as these samples prepared with freezer milling. Analysis of relatively flat 2D mineralising cell cultures may be more suitable for Raman spectroscopy, and is an interesting route of future experimentation.

Ultimately, XRF and Raman spectroscopy are analytical techniques useful in investigating the composition of materials, but they are based on differing principles, and provide different types of information. Raman spectroscopy measures the vibrational fingerprints of the mineral crystals and other molecules present in the powdered bone samples, whilst XRF measures the x rays produced by excited atoms. Therefore, Raman spectroscopy obtains information on the structure and composition of mineral within these samples, whereas XRF is sensitive to the elemental composition within the sample. These two techniques have strengths and weaknesses and together can be useful tools, providing complementary information regarding the composition of bone mineral, and other compounds. For example, XRF has a unique ability to assist in assessing the stoichiometry of bone but is unable to detect to the presence of elements with an atomic number of 6 or less, due to the structure of elemental clouds. Raman spectroscopy is shown to be capable of detecting molecules such as carbonate, which makes up a significant fraction of bone mineral. In this chapter, we have demonstrated how these two methods may be used to detect calcium and phosphate ion levels, as well as phosphate and carbonate molecules in bone mineral. With further refinement, increased sample numbers and/or automated methods, these two methods may provide important information on the progress of early mineralisation in cell cultures. Performing both techniques on defined areas in the same sample may allow the comparison of results, and help further understand how mineralisation occurs.

3.5 Conclusion

Micro XRF has shown to have a strong correlation with remaining mineral when compared with TGA, whereas Raman spectroscopy appears less well correlated, but can show more refined chemical information on the compounds present. These results are likely to be impacted by the limitations of this study, specifically the far smaller focal point of Raman microscopes affecting the ability to scan large areas of sample, increasing the impact of non-homogenous samples. This limitation may be less impactful when assessing samples on the nano scale, such as EVs.

Chapter 4 : The characterisation of extracellular vesicle impact on mineralisation

4.1 Introduction

Since their discovery in 1967 [9], extracellular vesicles (EVs) have been linked to mineralisation, with the suggestion that matrix vesicles [10] acted as the nucleating agents of mineralisation within cartilage. Understanding the mechanisms by which these observations *in vivo* can be imitated *in vitro* allows more controlled investigations into the processes involved. Subsequent translation of discoveries back into *in vivo* models potentially allows us to unlock new therapeutic avenues for bone-related diseases and injuries.

The ability of osteoblast and mesenchymal stem cell derived EVs to drive osteoblast differentiation and subsequent mineralisation has been witnessed, both *in vitro* and *in vivo* [163]. Here, supplementation of EVs into cell culture drove osteoblast differentiation, whereas addition into rat calvarial defects stimulated increased bone deposition, further supporting the involvement of EVs in the mineralisation process. Exactly which properties or characteristics of EVs are most important in these processes is unclear. Calcium and phosphate species that have been found in some EV like molecules [95] have been hypothesised as nucleation points for new mineral, but exactly which calcium phosphate species are present is unknown, and as different species can positively or negatively affect mineralisation processes [101,102], better characterisation of these molecules becomes essential.

One approach to provide greater insight into the mineralisation process is the use of XRF imaging, utilising the high-resolution techniques developed previously in this thesis. Using these methods, we can quantitively compare the elemental composition of mineral deposited by osteoblasts, including calcium and phosphate ratio of mineralising cultures.

When combined with EV supplementation, we can uncover increased information on the rate and composition of mineral deposition, and the effects of EVs upon this. In this chapter, we report the characterisation of extracellular vesicle impact on the

process of cell mineralisation *in vitro*, utilising the XRF methods we have developed so far in this thesis.

4.2 Methodology

4.2.1 MC3T3 cell culture

MC3T3 murine pre-osteoblasts were purchased from American Type Culture Collection (ATCC, UK). Growth culture media consisted of minimal essential medium (α-MEM; Sigma-Aldrich, UK), 10% fetal bovine serum (FBS), 1% penicillin/streptomycin (Sigma-Aldrich, UK) and L-glutamine (Sigma-Aldrich, UK). MC3T3s were cultured at scale in T175 culture flasks (Nunc, UK) in 15 mL media, which was collected and refreshed three times weekly. Once cells had reached approximately 70% confluency, the media used was changed. Control cells continued to be grown in growth culture medium described above, whilst osteogenic medium (described below) was used for the mineralising cells. Cells were then grown in the relevant media for a total of 21 days. Cell number totalled approx. $3x10^6$ when this period ended as cells became confluent. At each media change, the media removed was pooled and stored at 4 °C, resulting in a total of 90 mL conditioned media per flask at the end of the 21 days. Typically, 6 flasks per condition (mineralising and non-mineralising) were grown simultaneously.

Osteogenic medium comprised of growth culture media supplemented with 10 mM β-glycerophosphate (Sigma-Aldrich, UK) and 50 µg/ml L-ascorbic acid (Sigma-Aldrich, UK). Culture medium utilised for EV isolation was depleted of FBS-derived EVs by ultracentrifugation at 120,000 g for 70 min prior to use.

4.2.2 Cell culture – EV studies

EV studies were carried out by adding EV suspension to mineralising media to a concentration of 10 µg protein/mL EVs to create EV treated media, as per previous studies 13. EV treated media was used as per mineralising media, replacing spent media 3x weekly. EV production was not possible at large scale, therefore it was not possible to produce sufficient EVs to perform more than 3 repeats, for 14 days of co-culture experiments, as well as quantification and characterisation experiments.

4.2.3 EV isolation - Ultracentrifugation

EVs were isolated from conditioned medium via centrifugation at 2000× g for 20 min to remove cellular debris, supernatant was then spun at 10,000× g for 30 min to remove further unwanted particles, supernatant was again removed and then spun at 120,000× g for 70 min to pellet EVs. Supernatant was then removed, the pellet washed in sterile PBS and re-centrifuged at 120,000× g for 70 min, the resultant pellet was re-suspended in 200 µL PBS. All ultracentrifugation steps were performed utilising the Sorvall WX Ultra Series Ultracentrifuge (Thermo Scientific, Paisley, UK) and a Fiberlite, F50L-8×39 fixed angle rotor (Piramoon Technologies Inc., Santa Clara, CA, USA).

4.2.4 EV counting – Zetaview NTA

Nanoparticle tracking analysis was performed on EV samples to determine particle size and concentration using a ZetaView® instrument (Particle Metrix, Germany). EV samples were diluted 1:100 in PBS and injected into the ZetaView®, where 4 × 40 s videos were obtained of particles in motion. Particle size and concentration was determined with the ZetaView® software.

4.2.5 EV counting – Nanodrop

Quantification via Nanodrop (Nanodrop 2000 Spectrophotometer, Thermo Fisher Scientific, UK) involved placing 5 µL onto the instrument cradle, and assessing protein absorbance at 280 nm.

4.2.6 Bicinchoninic acid assay (BCA)

Total EV protein concentration was determined using the Pierce BCA protein assay kit as per manufacturer's instructions (Thermo Scientific, UK). BCA detection relies upon the Biuret reaction, wherein copper ions are reduced in the presence of protein in an alkaline medium. A bicinchonic acid solution reacts with Cu^{+1} ions to produce a colometric response which can be quantified using absorbance at 590 nm, using a Biotek Synergy HT microplate reader (Biotek Instruments Inc., USA).

4.2.7 Micro-XRF

Maps of elemental composition across various sample types were acquired using a Tornado M4 micro-XRF (µXRF) system (Bruker Nano, Germany) fitted with a Rhodium micro focus X-Ray tube and a polycapillary lens, with the X-ray tube set to 50 kV

voltage and 200 µA current. The chamber pressure was lowered to 20 mbar to maximise sensitivity of signal. The system was programmed to acquire a map across the sample by rastering the microfocus beam over the slide with a pixel size of 20 µm and a time per pixel of 10 ms. An XRF spectrum was collected at each pixel and elemental maps generated progressively in real time, creating an image where pixel intensity represented X-Ray detector pulses per electron volt (eV) at each measurement point on the sample. Intensities were normalised to rhodium peaks to allow comparison between samples.

4.2.8 Production of liposomes

Liposomes composed of phosphatidylcholine and cholesterol in a 70/30 molar ratio were prepared using the thin film hydration method. Lipids at desired molar ratio were dissolved in chloroform in a 25 mL round bottom flask. They were then dried in a rotary evaporator (Rotary evaporator RV 10 auto V-C, IKA, Germany) for 2 hours under vacuum (100 mbar) and mixing (170 rpm). All the procedure was performed above the critical phase transition temperature of the lipids. Lipids were rehydrated with 0.9% NaCl solution and mixed for a further 2 hours using the rotary evaporator. The resulting suspension was then sonicated for 30 mins prior to be extruded 21 times through a 100 nm filter to create monodispersed liposomes (Avanti Mini Extruder, Avanti Polar Lipids, USA). Size determination using DLS was performed following the liposome production to control the quality of the product.

4.2.9 Statistics

All statistical analysis was performed using GraphPad Prism version 5.03 for Windows, GraphPad Software, San Diego California USA, www.graphpad.com.

4.3 Results

To begin investigations into the impact of EVs upon mineralisation, it was first necessary to produce experimentally relevant EV numbers. EV conditioned media was collected from MC3T3 cells cultured for a period of two weeks in growth media or growth media supplemented with mineralisation induction compounds. Subsequently, EVs were isolated from this conditioned media using sequential ultracentrifugation, as described in the methodology section. Pierce bicinchoninic acid assay (BCA) testing for protein levels in the EV isolate (a common method of EV quantification [164]) showed (Figure 4.1) that mineralising cells produced EVs at higher concentrations than the non-mineralising cells (Student's T Test p=0.0018). This suggests that there is a correlation between mineralising activity and the presence of the EVs.

4.3.1 Mineralising MC3T3 cells produce more EVs that non mineralising cells

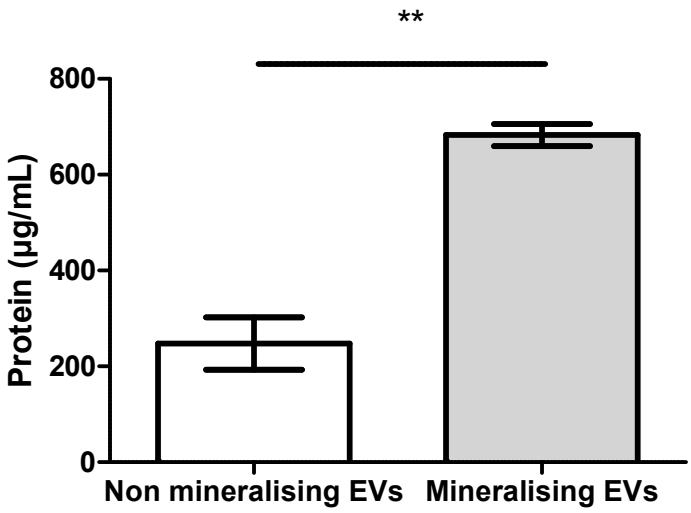

Figure 4.1: EV count by protein from non-mineralising and mineralising cells. MC3T3 cells were cultured for a period of three weeks and EVs extracted. Quantification of EV number using protein detection by Pierce bicinchoninic acid assay (BCA) indicates mineralising cells produced greater numbers of EVs than non-mineralising cells (Student's T Test p=0.0018). ** indicates $p \leq 0.01$.

4.3.2 EV number varies across mineralisation states

As previously discussed, EV characteristics can be affected by a multitude of conditions, here, we investigated changes that occur in EV production between different time points of mineralisation, using several methods of EV quantification. NTA analysis uses light scattering to quantify microparticles in suspension, and as such, quantifies EVs and any attendant contamination without discerning between the two, leading to overestimation. Non-parametric testing on the NTA data (Figure 4.2.i) indicated a significantly increased particle concentration at Day 7 when compared to Day 14 and 21 (Mann Whitney test $p<0.01$). Pierce BCA and Nanodrop methods (Figure 4.2.ii) both estimate protein concentration, and therefore number of EVs, but using different methods. BCA utilises the reduction of copper ions by protein and subsequent colour change (biuret reaction) to quantify EVs, whereas Nanodrop quantification utilises spectrophotometry, absorbance at 280 nm indicating protein content of a sample. Unfortunately, both methods are also subject to overestimation due to protein contaminants that co-separate with EVs. Both methods of protein detection showed a trend of lower protein in Day 21. Non-parametric testing indicates a significant reduction in protein detected by BCA at day 21 when compared to day 14 (Mann Whitney test $p=0.0286$), no other significant differences were discovered. Due to lack of access to necessary equipment, nanoparticle tracking analysis (NTA) was only performed on a single biological sample, with 5 technical repeats. Pierce BCA and Nanodrop data consists of n=3 biological repeats.

Using the average estimate of particle count across 7, 14, and 21 day samples (Figure 4.2.i) coupled with the average protein count across days 7, 14, 21 (figure 4.2.ii), it is possible to estimate maximum potential phosphorous ions being delivered by EV supplementation of media. The EV conditioned media supplied to cells contained EV suspension at a final concentration of 10 µg/mL protein. The mean protein concentration of EV samples detected using BCA was used, as this was the method typically used to normalise EV suspensions throughout further experiments. The mean protein count of the samples collected at days 7, 14 and 21, 1.03 (±0.147) mg/mL (Figure 4.2.ii) was divided by the mean particle number per mL detected by NTA (Figure 4.2.i), 6.81 (±0.584) $x10^{11}$, to provide an average protein per particle, 1.53 (±0.282) nanograms (Figure 4.2.iii). This number was used as an approximate estimate

of average protein per EV. A dilution of the EV samples was performed to result in a final concentration of 10 μg/mL EV related protein in EV conditioned media, which, equates to 6.55 $x10^6$ EVs per mL. When the figures for maximum possible delivery of phosphate ions from table 1.2 are used, then the maximum amount of EV derived phosphate ions delivered per mL of EV conditioned media is 1.70 $x10^{14}$. The number of phosphate ions delivered by mineralising media contained per mL of the 10 mM β glycerophosphate solution is 6.022 $x10^{18}$, a figure 35,000 times higher than that of the EV suspension added, therefore, adding the EV suspension has an effect of increasing the phosphate ion concentration by 0.0028%, a relatively small amount.

i. NTA particle number quantification

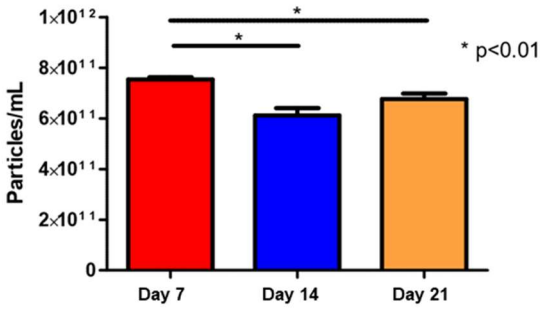

ii. Protein quantification

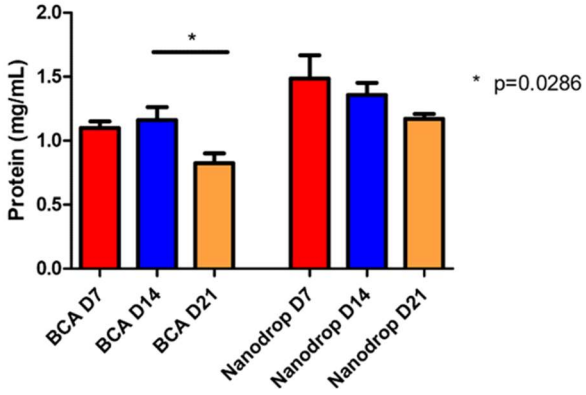

iii.

	Mean across all days
NTA EV count (particle/mL)	6.81 (±0.584) x10^{11}
BCA Protein (mg/mL)	1.03 (±0.147)
Protein per EV (pg)	1.53 (±0.282)
Number of EVs per mL in a solution containing 10 µg/mL protein (average of days 7, 14, 21 EV count using NTA)	6.55 x10^{6}
Maximum number of phosphate ions per EV (Table 1.2)	2.59 x10^{7}
Maximum number of phosphate ions/mL in EV conditioned media (10 µg protein/mL EV suspension added)	1.70 x10^{14}
Number of phosphate ions/mL in a 10 mM β glycerophosphate solution	6.022 x10^{18}

Figure 4.2: Quantification of EV number using different methods. Quantification of EV number was measured using (i) nanoparticle tracking analysis (NTA) (n=1 biological sample, 5 technical repeats), (ii) Pierce bicinchoninic acid assay (BCA) (n=3), and Nanodrop spectrophotometry (n=3). NTA quantification found significantly greater EV production at day 7 compared to all other time points (Mann Whitney test $p<0.01$). BCA found day 14 to produce the greatest number, with a significant drop at day 21 (Mann Whitney test $p=0.0286$). Nanodrop assessment found the greatest production at day 7, however, this number was not significantly greater than the other two time points, with greater variation overall when compared to the other methods. (iii) Calculates the maximum number of phosphate ions per mL delivered by EVs in EV conditioned media, for comparison against phosphate ions delivered by mineralising media. Utilising the mean particle count/mL using NTA, across all time points (7, 14, 21 days), and the mean protein (mg/mL) using BCA across all time points, coupled with estimates made in Table 1.2 for maximum phosphate ion capacity of an average sized EV, these calculations illustrate that the addition of EVs to mineralising media has an extremely small impact (0.0028% increase) upon the concentration of phosphate ions present in mineralising media. The reason for using BCA protein counts was due to this method being considered the gold standard for EV quantification, due to its ease and repeatability [164]. * indicates $p \leq 0.01$.

4.3.3 Incubation of vesicles with MC3T3s results in increased mineralisation

Before characterising the EVs, it was necessary to ensure they were capable of increasing mineralisation in target cells. Cells were cultured for 21 days in mineralising media, and 14 days in the presence of 10 µg/mL EV suspension, as detailed in the methodology section. At multiple timepoints, the bottoms of the cell culture plates were removed, fixed, and scanned on the Bruker µXRF, as per methodology section in this chapter. Visible light images of these cell culture sections can be seen on the left of Figure 4.3. Unfortunately, due to the significant amount of EVs required for the EV supplemented media, replacing media three times weekly, three repeats, for 7 and 14 days, it was not possible to perform the experiment over 21 days for EV supplemented cells. However, when MC3T3 cells were incubated in mineralising media only for 14 days, mineralisation was not visible, it was therefore decided to progress the mineralisation media only cells to 21 days, at which point mineralisation was witnessed. This progression permitted the comparison of advanced mineralisation between conditions, which is detailed below.

Visually, culture samples taken from EV cocultured cells appeared to have much greater mineral deposition, with much more uniform spread, when compared to cell cultures that were grown for the same timeframe in osteogenic media only (Visible light, Figure 4.3). This observation was supported by the XRF data in Figure 4.3 and Figure 4.4, which show elemental maps of the samples and graphical quantification respectively. Chemical analysis of the cultures shows the deposition of calcium and phosphate did not occur significantly until day 18 in mineralising cultures without added EVs (Paired t test $p=0.007$ and $p=0.004$ for Ca and P respectively). Calcium and phosphate deposition occurred much earlier for EV+ cell cultures, significantly increased at day 7 when compared to day 7 cells grown without EVs (Mann Whitney $p=0.036$ for both Ca & P).

Interestingly, there is an increase in sulphur presence correlating with time across all cultures, this may be an indicator of an increase in ECM deposition, as sulphated glycosaminoglycans are a key component in ECM [165] and contain sulphur bonds. The increase in sulphur deposition appears independent from calcium and phosphorous, and may be worthy of future investigation. Investigating whether ECM quantity is

correlated with sulphur signal, perhaps by quantification of collagen, would then provide the opportunity to investigate why the sulphur signal is decoupled from calcium and phosphate. This data may suggest that just the presence of ECM deposited by early-stage cell cultures (0-14 days) is not capable of instigating mineralisation. It may be lacking a key component that is essential in the mineralisation process. If this component can be identified, perhaps by proteomic analysis of early and late stage ECM, it may be validated by addition of liposomes carrying this specific cargo to early stage ECM, if it subsequently leads to early mineralisation. In the presence of EVs, sulphur deposition appears to be significantly accelerated, with day 7 EV positive cultures depositing significantly more sulphur than day 7 EV negative cultures (Mann Whitney $p=0.036$). These findings may indicate that EVs carry molecules that assist in the 'maturing' of ECM.

Calcium : phosphate ratio is low in mineralising cells without EVs until the later stages (day 18 and 21). In mature mineralised cultures, (day 21 without EVs and day 14 with EVs) Ca:P ratio is significantly lower in the presence of EVs (Mann Whitney $p=0.036$), than without EVs. This may suggest that the mineral deposited in the presence of EVs is stoichiometrically different to that deposited by cells in the absence of EVs. This possibility may link with the visual differences apparent with the mineral deposition witnessed in Figure 4.3, whereby mineralisation in the presence of additional EVs appears uniform, whereas mineralisation in the absence of additional EVs appears less uniform and more localised nodules.

4.3.4 XRF chemical analysis of mineralised cells

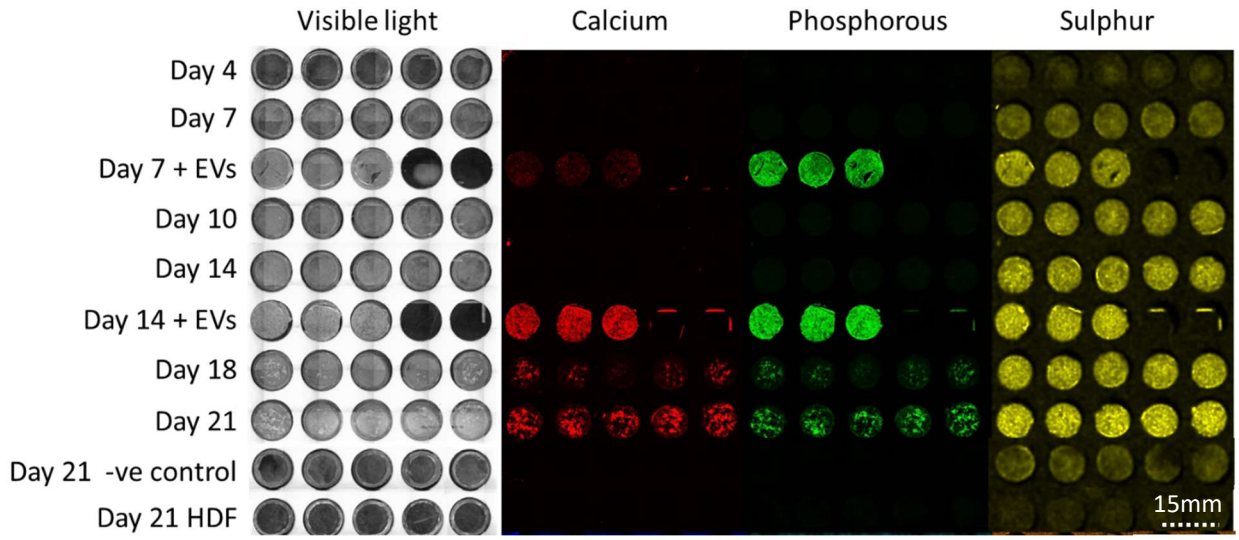

Figure 4.3: Visible and elemental maps of MC3T3 cells grown in osteogenic and EV added media. MC3T3 cells grown over various time points in osteogenic (n=5) or 10 µg/mL EV supplemented (+ EVs, n=3) media. -ve control cells grown in non-osteogenic media. HDF = human dermal fibroblasts grown in osteogenic media, a non-mineralising control cell line. The cloudy appearance in visible light of later cultures is a sign of extensive extracellular matrix and mineral deposition. Cells grown in the presence of EVs deposited calcium, phosphate and sulphur faster than those without.

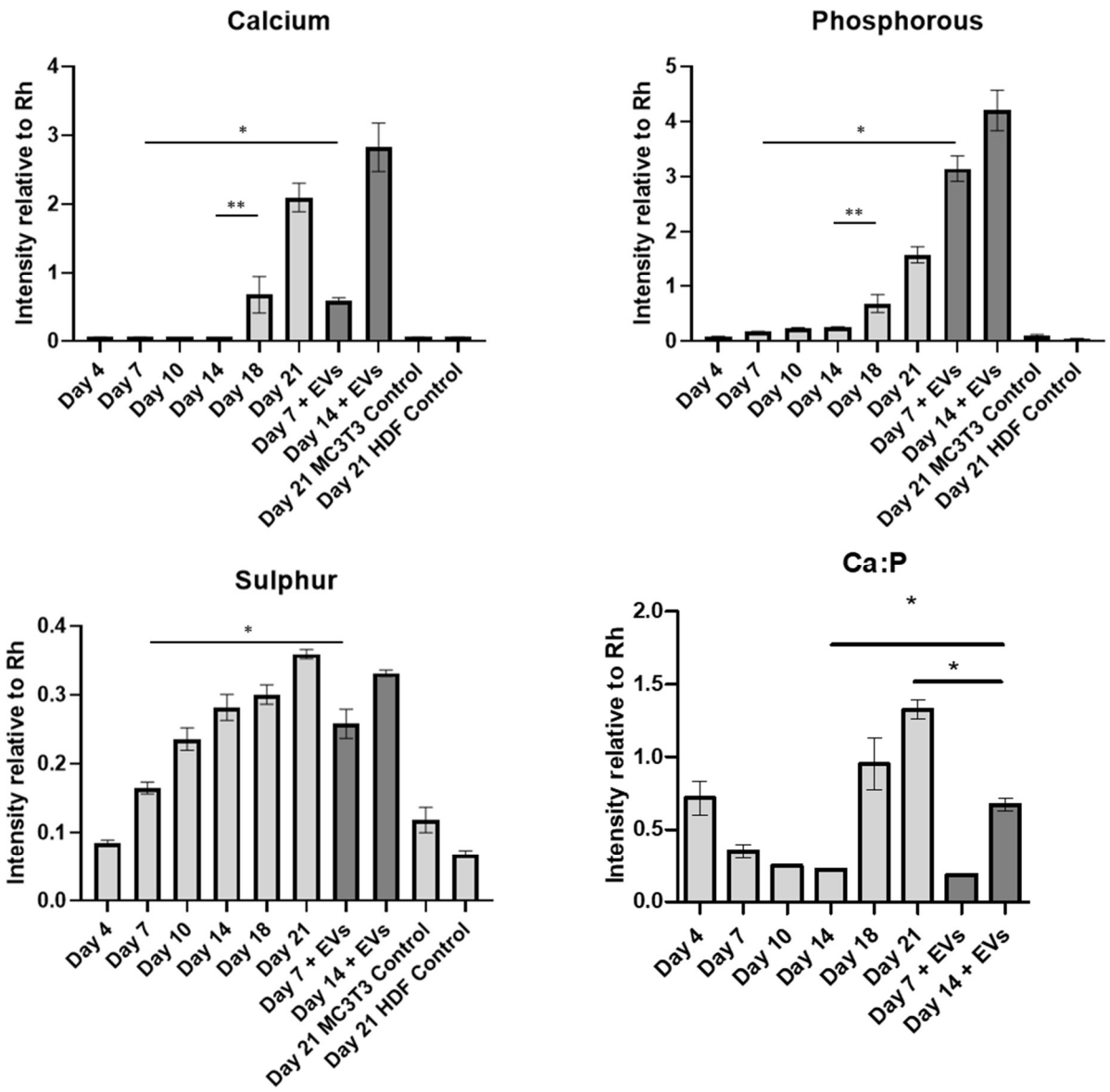

Figure 4.4: Comparative quantification of elemental presence across samples. Total replicates: n=5 for EV -ve cultures and n=3 for EV +ve cultures. XRF chemical analysis of the cultures shows co-deposition of calcium and phosphate occurs significantly at day 18 in osteogenic media without added EVs (Paired t test p=0.007 and p=0.004 for Ca and P respectively). Osteogenic media containing EVs encouraged faster calcium and phosphate deposition at 7 days compared to media without (Mann Whitney p=0.036 for both Ca & P). Both controls (MC3T3 in growth media, and HDF in osteogenic media) show an absence of calcium and phosphorous deposition. ECM (Sulphur as proxy for extracellular matrix protein) deposition increases regularly across mineralising cultures, suggesting increased ECM protein does not result in increased mineralisation. In the presence of EVs, sulphur deposition is significantly accelerated in cultures at day 14 (Mann Whitney p=0.0357). Calcium:phosphate ratio is low in mineralising cells without EVs until the final stages (day 18 and 21). Calcium : phosphate ratio is low in mineralising cultures with EVs present at day 7 but increased at day 14, however, the Ca:P ratio in mature mineral seen at day 14 in the EV +ve cultures is not as high as the mature mineral seen at day 28 in the EV -ve cultures (Mann Whitney p=0.0357). ** indicates $p \leq 0.01$. * indicates $p \leq 0.05$.

4.4 Discussion

This chapter discusses various facets of mineralising osteoblast extracellular vesicles and their characteristics. Our first results from BCA measurement show a statistically significant increase in the number of EVs obtained from mineralising osteoblast EVs when compared to non-mineralising, quiescent osteoblast EVs. Previous work by Guntur *et al*. [166] has shown an increase in oxidative phosphorylation and glycolysis for differentiating/mineralising osteoblasts when compared to quiescent osteoblasts. The increase in these energy generating pathways are hallmarks of an increase in metabolic rate, which has been linked to increased EV production [167] and may explain the change seen here in EV production.

Interestingly, the mineralising cells in the Guntur study changed preference from the more energetically efficient oxidative phosphorylation method of energy generation to the less efficient, but reduced oxidative stress, of the glycolysis pathway between 14 and 21 days of differentiation, a finding also supported by Misra *et al*. [168]. This change in method of energy production produced energy at a slower rate, and thus a slower metabolic rate, which may be a possible explanation for the lower EV production levels seen at day 21 in Figure 4.2.ii. seen by both protein-based EV quantification methods.

Investigations into methods of EV quantification detailed in Figure 4.2 found differing results based upon the method of measurement used. Particle counting (NTA), (figure 4.2.i) found significantly greater particles at day 7, which was not supported by the protein based quantification methods of BCA and Nanodrop (Figure 4.2.ii).

The ISEV guidelines [164] are designed to suggest much needed standardisation to EV investigations, however, they do not mention the use of Nanodrop as an EV protein quantification method, but do, however, recommend BCA. The two methods were compared in Figure 4.2.ii, to see if the simpler and more rapid Nanodrop method would correlate well with the gold standard of BCA. These protein-based methods did not show a correlation, with the only significant finding being that BCA showed significantly less at day 21 than at other time points, unsupported by Nanodrop. This lack of correlation between these methods suggests that they cannot be used interchangeably.

Mineral deposition observed in Figure 4.3 and analysed in Figure 4.4 shows an absence of calcium and limited phosphorous deposition until after day 14 in mineralisation media only cell cultures. Whether this is due to a phenotypic or translational switch in the osteoblast cells, maturity of the ECM, and cause or effect of the previously mentioned energy source changes is unclear and requires further investigation. EV supplementation appears to have a significant effect upon mineral deposition, rapidly accelerating the process, as significant calcium and phosphorous appears present at the earlier stage of 14 days in EV supplemented cultures, whereas it appears absent in day 14 cultures without added EVs. The mineral deposition present in the EV supplemented cultures appears more uniform in comparison to the more nodular appearance of non-EV supplemented cultures.

If the theory of EVs acting as nucleation sites for mineralisation is correct, seeding large numbers of nucleating particles, EVs, to cultures may provide a huge number of nucleation sites, and therefore a more uniform mineral formation. In the non-EV supplemented cultures, these nucleating particles would need to be produced by the osteoblasts themselves, dependent upon their maturity (differentiation and cell cycle status). This natural variation in a cell population, and the importance of EVs in cell-cell cross talk may lead to localised areas of mineralisation, as seen in the nodular formation of mineral in the non-EV supplemented cultures. The changes in phosphate deposition cannot be explained by the EV phosphate alone, using the numbers calculated in Table 1.2, and Figure 4.2.iii, the EV borne phosphate could only account for 0.002% of the total phosphate delivered by the mineralising media, due to the significant effect of the addition of 10 mM glycerophosphate. The significant increase in mineralisation speed may therefore be attributed to other properties of the EVs, although, this does not take into account the species of phosphate being delivered by EVs, for example, one form may be more bioavailable than another.

A method of investigating this may be to tag the supplemental EVs with a nanoparticle that is highly visible to XRF. Doing this in conjunction with earlier visualisation, and a vastly reduced EV number, to identify newly formed mineral nodules before they become indistinguishable from each other, may provide further useful information. If mineral nodule formation appears to correlate with the location of these tagged EVs, then this may support the theory of EVs as mineral nucleation sites.

4.5 Conclusion

These results do not show a correlation between NTA and BCA quantification, whilst Nanodrop does not appear to be a reliable quantification tool for extracellular vesicle protein. Extracellular vesicle supplementation into mineralising media appears to have a significant positive impact upon the mineralisation of osteoblast cells. This effect is unlikely to be as a result of potential phosphate carried by the EVs, as it makes up a small proportion of total phosphate available. Further work is needed to establish whether EVs are acting as nucleation sites during mineralisation.

Chapter 5 : Improvements to current EV characterisation methods

5.1 Introduction

Standard light microscopy is not capable of the resolutions required to visualise EVs, the wavelengths of visible light (380-740 nm) are larger than a significant proportion of the EV population (30-2000 nm) preventing effective imaging. To be able to effectively image such small objects, a shorter wavelength is required, and so an electron beam is far better suited to the task. Transmission electron microscopy (TEM) is widely used in the field of EV research, to provide confirmation that the material being investigated has the expected morphology. Images obtained by TEM are also a useful tool to qualitatively identify purity, concentrations and relative amounts of debris, an issue that may affect subsequent attempts to characterise an EV population.

Significant advances in understanding the biogenesis, composition, and functions of extracellular vesicles have been made in recent decades. However, the characterization and isolation of these highly heterogeneous structures remain a significant challenge. TEM has been a valuable tool in the investigation of extracellular vesicles, providing information on their structure and morphology, however, this information still remains imperfect. For example, a large majority of EV images to date tend to show cup shaped morphologies [167] however, this is believed to be an artifact of the TEM fixation process. The dehydration necessary to prepare EVs for TEM, is believed to result in spherical EVs to a cup shaped morphology. Therefore, the current methodologies for imaging extracellular vesicles using transmission electron microscopy have room for improvement, particularly in terms of realistic morphologies.

The significant heterogeneity of EVs makes individual molecule characterisation very desirable, however, their nano size makes this challenging with most conventional analysis methods. Resolving this inherent complexity will help future research understand the factors that underpin EVs as biological drivers of tissue regeneration, opening up their potential for use in regenerative therapies and further understanding of disease states.

Raman spectroscopy alone is not sensitive enough to observe individual EVs reliably, as focal volumes on Raman lasers tends to be in the micrometre size. Recent work from Penders, *et al*. [169], automated optical tweezer techniques to isolate individual EVs, allowing collection of individual particle data. Optical tweezers were first demonstrated in 1986 [170] and rely upon the principle of radiation pressure, and the momentum carried by photons of light in an optical tweezer trapping laser. The trapping laser of an optical tweezer set up is tightly focussed through a microscope objective to produce an appropriately sized focal point. Extracellular vesicles have a refractive index that tends to be greater than the surrounding medium (PBS in this case), and therefore act as a lens upon the photons of the trapping laser, diffracting the photon and altering its direction. This diffraction of the photon causes an alteration of its path (Figure 5.1), therefore changing its momentum, and the equal and opposite reaction to this energy change is a force upon the EV. As the focal point of a trapping laser contains the highest density of photons, most photons will be imparting a force upon the EV towards this point, moving the EV towards, and once reached, trapping it at this focal point. When coupled with a Raman laser focussed upon the same focal point, this allows simultaneous trapping and molecular characterisation of single EVs. Characterising singular EVs, whilst challenging, may enable the identification of subsets within EV populations. This desirable goal may make it possible to observe changes in the relative proportion of these subsets, as opposed to changes across the population as a whole. Resolving changes in populations down to this level may unlock interesting information that can be incorporated into future biomaterials, for example, identifying EV subsets that are present during increased or decreased mineralisation, may prove useful in designing future therapeutics. The significant heterogeneity of EV populations may require a prohibitively large dataset, to successfully draw conclusions on subsets with statistical confidence.

Heterogeneity of EVs is not limited to the chemical cargo they contain, as discussed in Chapter 1 of this thesis, EVs have been shown to carry a wide variety of molecules, varying significantly in protein load, lipid makeup and RNA content. This heterogeneity has been shown to vary greatly depending on parent cell type [124], culture conditions [127], and even individual cell polarity [120]. Attempts to catalogue the molecular variety of

EVs are underway, with the International Society for Extracellular Vesicles encouraging [164] the use of online databases, such as Vesiclepedia (http://www.microvesicles.org) and ExoCarta (http://www.exocarta.org) to store experimental details and molecular datasets.

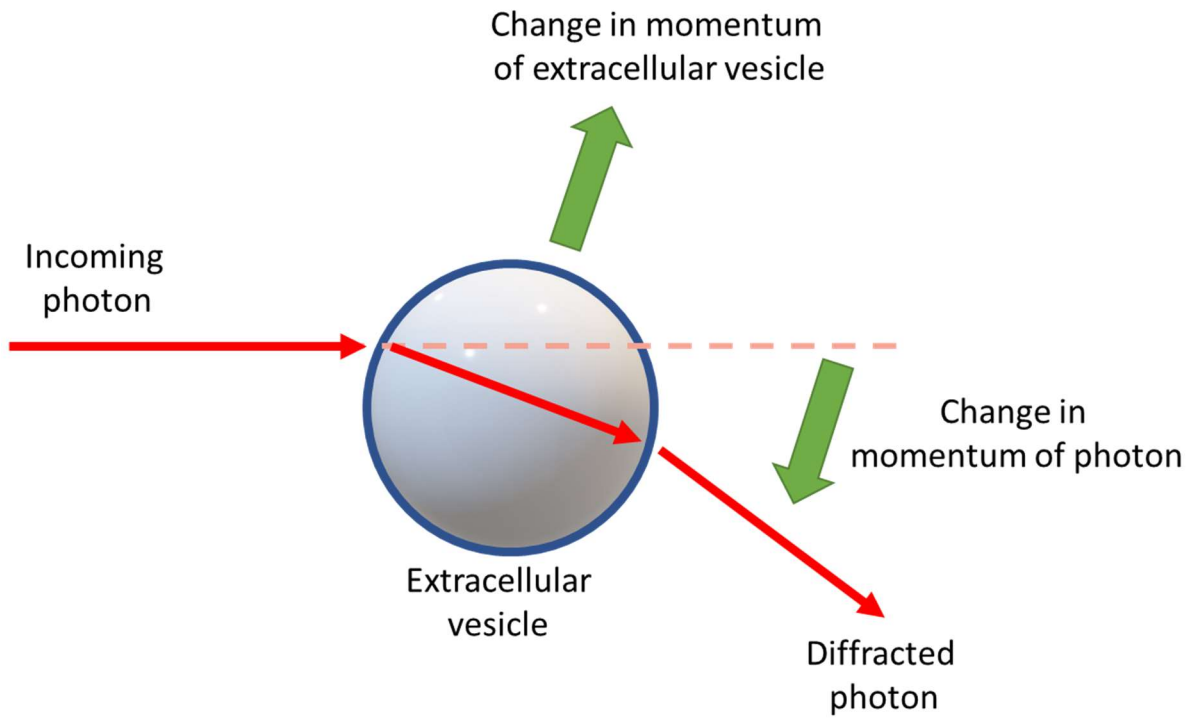

Figure 5.1: Simplified representation of optical tweezer principle. As photons from an optical trapping laser interact with the different refractive index possessed by an extracellular vesicle, the photons are diffracted away from their original path, causing a change in momentum. This momentum change has an equal and opposite force which acts upon the extracellular vesicle, causing the EV to move towards the focal point of the trapping laser. [170]

This chapter aims to present an enhanced methodology for the transmission electron microscopy imaging of extracellular vesicles, addressing the limitations of existing approaches and offering a more robust and efficient protocol. The proposed enhancements will focus on optimizing sample preparation to maintain a more representative morphology, as well as labelling techniques to identify the objects seen as EVs. In addition, we employ the methods of Raman spectroscopy and optical tweezer technology to attempt to form a functional method of individual EV Raman characterisation.

5.2 Methodology

5.2.1 Cell culture

MC3T3 murine pre-osteoblasts were purchased from American Type Culture Collection (ATCC, UK). Growth culture media consisted of minimal essential medium (α-MEM; Sigma-Aldrich, UK), 10% fetal bovine serum (FBS), 1% penicillin/streptomycin (Sigma-Aldrich, UK) and L-glutamine (Sigma-Aldrich, UK). MC3T3s were cultured at scale in T175 culture flasks (Nunc, UK) in 15 mL media, which was collected and refreshed three times weekly. Once cells had reached approximately 70% confluency, the media used was changed. Control cells continued to be grown in growth culture medium described above, whilst osteogenic medium (described below) was used for the mineralising cells. Cells were then grown in the relevant media for a total of 21 days. Cell number totalled approx. $3x10^6$ when this period ended as cells became confluent. At each media change, the media removed was pooled and stored at 4 °C, resulting in a total of 90mL conditioned media per flask at the end of the 21 days. Typically, 6 flasks per condition (mineralising and non-mineralising) were grown simultaneously.

Osteogenic medium comprised of growth culture media supplemented with 10 mM β-glycerophosphate (Sigma-Aldrich, UK) and 50 µg/ml L-ascorbic acid (Sigma-Aldrich, UK). Culture medium utilised for EV isolation was depleted of FBS-derived EVs by ultracentrifugation at 120,000 g for 70 min prior to use.

5.2.2 EV isolation - Ultracentrifugation

EVs were isolated from conditioned medium via centrifugation at 2000× g for 20 min to remove cellular debris, supernatant was then spun at 10,000× g for 30 min to remove further unwanted particles, supernatant was again removed and then spun at 120,000× g for 70 min to pellet EVs. Supernatant was then removed, the pellet washed in sterile PBS and re-centrifuged at 120,000× g for 70 min, the resultant pellet was re-suspended in 200 µL PBS. All ultracentrifugation steps were performed utilising the Sorvall WX Ultra Series Ultracentrifuge (Thermo Scientific, Paisley, UK) and a Fiberlite, F50L-8×39 fixed angle rotor (Piramoon Technologies Inc., Santa Clara, CA, USA).

5.2.3 EV isolation – Size exclusion chromatography

EVs were isolated from conditioned medium via centrifugation at 2000× g for 20 min to remove cell debris and apoptotic bodies. EV containing supernatant was

concentrated with 100 kDA molecular weight cut-off Amicon spin filters (Merck Millipore). Concentrated conditioned media was loaded onto qEVoriginal / 70 nm SEC Columns (Izon Science, New Zealand) and isolated using the qEV automated fraction collector (Izon Science, New Zealand). The EV-containing fractions were pooled after elution and stored in 10µL aliquots at -80 °C.

5.2.4 Production of liposomes

Liposomes composed of phosphatidylcholine and cholesterol in a 70/30 molar ratio were prepared using the thin film hydration method. Lipids at desired molar ratio were dissolved in chloroform in a 25mL round bottom flask. They were then dried in a rotary evaporator (Rotary evaporator RV 10 auto V-C, IKA, Germany) for 2h under vacuum (100 mbar) and mixing (170 rpm). All the procedure was performed above the critical phase transition temperature of the lipids. Lipids were rehydrated with 0.9% NaCl solution and mixed for a further 2h using the rotary evaporator. The resulting suspension was then sonicated for 30mins prior to be extruded 21 times through a 100 nm filter to create monodispersed liposomes (Avanti Mini Extruder, Avanti Polar Lipids, USA). Size determination using DLS was performed following the liposome production to control the quality of the product.

5.2.5 Transmission Electron Microscopy

Formvar coated copper TEM grids (300 mesh) (Sigma-Aldrich, UK) were optionally incubated for 10 mins on 50µL drops of wheat germ agglutinin (1:300 in H_2O) or polylysine (1%, 1 mg/mL) to enhance EV attachment, and washed 5 times in distilled water, and once in 1x PBS. Following this, grids were incubated in a humidity chamber for 15 minutes with 5 µL EV suspension, and washed twice in 1x PBS. Optionally, for labelling, grids were blocked for 10 minutes with 5 µL 1% fish skin gelatin (FSG) in PBS, then incubated for 10 minutes with rabbit anti human CD63, diluted 1:5 in 1% FSG in PBS, then washed 5x in PBS. This was followed by incubation with protein A bound to 10 nm gold diluted 1:50 in 1% FSG, then washed 5 times in PBS, and 5 times, rapidly, in water. Next, 4% uranyl acetate was mixed 1:10 with 2% w/v methylcellulose and grids were incubated for 2 minutes, removed with a wire loop and dried with blotting paper followed by air drying for 5 minutes. Grids were then imaged at 200 kV.

5.2.6 Optical trapping & Raman spectroscopy – EV samples

Optical trapping and Raman spectroscopy was carried out on inVia Renishaw Qontor Confocal Raman microscope (Renishaw plc., UK) with Meopta LMA-1 laser microscope adapter (Meopta, Czechia). Trapping was attempted using a 1064 nm laser using Cobalt software, through a 100x immersion objective, at a power of 300 mW. Raman spectra were obtained using a 785 nm laser in the main fingerprint region of 700-1700 cm^{-1} centred around 1200 cm^{-1}, at 100% power for 1 second, with 10 accumulations per point, and a mean obtained, to improve signal:noise ratio.

EV suspension droplets were deposited onto an aluminium coated slide, and brought into contact with the objective. The 1064 nm trapping laser and the 785 nm Raman laser were manually focussed onto a single location on the aluminium substrate, then the platform lowered to bring the focal volumes within the EV suspension. Multiple spectra were taken from different locations from a single drop of EV suspension at 10 µg/mL protein as characterised by BCA. Background signal was removed, intensities normalized, mean obtained, data was then normalised against phenylalanine, a common amino acid found in protein. Peak intensities and wavenumbers were identified using the data cursor in the WiRE software (Renishaw plc, UK).

5.2.7 Statistics

All statistical analysis was performed using GraphPad Prism version 5.03 for Windows, GraphPad Software, San Diego California USA, www.graphpad.com.

5.3 Results

5.3.1 Improvements to current methodologies of EV TEM

Cell culture media was collected from MC3T3 cells after 14 days of mineralisation, and EVs isolated as per methodology section. The most common method used in EV imaging, simple methylcellulose embedding and uranyl acetate staining of the sample, was the first method attempted. This produced objects ranging from 305 – 718 nm, however these objects were not readily identifiable as EVs from our samples. The lack of EV like objects were thought to be due to the low concentration in the EV sample (Figure 5.2i), but also potentially due to a failure of EVs to bind adequately to the formvar coated TEM grids. To overcome this, grids were pre-coated in wheat germ agglutinin, known to bind N-acetylglucosamine, a sugar residue found in post translational modification of proteins, and likely present on the surface of EVs [171] (Figure 5.2ii). This produced more familiar EV shaped objects, with a mean size of 173 ± 14 nm (n=10). In addition, some grids were coated in polylysine, a positively charged polymer commonly used in tissue culture to encourage adherence due to interaction with negatively charged lipid bilayers, a feature found in EVs (Figure 5.2iii) mean size 263.4 nm ± 45.34 (n=13). Both methods resulted in EV like structures binding to the carbon grid, however, varying levels of cellular debris was also present.

To positively identify the structures as EVs it is necessary to label them with markers unique to EVs. The surface protein CD63 has been shown to be expressed on the surface of exosomes [67], a subset of EVs, and an attempt to label this protein was made on these samples. Incubation of polylysine and EV coated grids with a murine anti-Human CD63 antibody, followed by secondary labelling with protein A gold (PAG) bound with 10 nm gold produced images indicating significant EV binding alongside EV labelling (Figure 5.2iv). Whilst some binding to smaller vesicles was seen (blue arrows), some binding of PAG to debris was also witnessed (red arrows). There was some difference in the mean sizing of EV-like structures (119.4 nm ± 17.43, n=66), and the EV like structures that were bound by PAG (67.0 nm ± 5.4, n=19) (Table 5.1).

This methodology was replicated in our laboratories at the University of Birmingham, including control steps such as PBS only formvar grids (Figure 4.8i), and liposome only grids (Figure 5.3ii). The PBS control grids displayed crystalline structures as well as globular structures (mean size 34.9 nm ± 1.9, n=96), the latter was a common sight

throughout the majority of the TEM work, suggesting that these debris may not be EV derived, but simply present in the components of preparing the grids, including but not limited to, poly-L-lysine, 1x PBS, 1% fish skin gelatin, anti CD63 antibody, protein A gold, 4% uranyl acetate and 2% w/v methylcellulose. Testing each of these components individually would be a time consuming but necessary next step to creating more effective TEM images.

As can be seen in Figure 5.2iv, the EV isolations obtained in the early stages of this project show evidence of significant debris and aggregation. It is unclear whether this is due to the method of preparation for TEM, or artifacts from this method of isolation. Attempting to characterise EVs at this level of purity will seriously hamper the reliability of any results obtained, distinguishing between EVs and debris, or aggregated EVs will be impossible.

Two methods of isolating EVs were assessed in these preparations, ultracentrifugation method (Figure 5.3iv) and an alternative, size exclusion chromatography (SEC) (Figure 5.3v). Our findings suggest that the size of EVs obtained from the two methods were very similar, 36.0 nm ± 1.9 (n=92) for SEC preparations, and 32.9 nm ± 1.9 (n=56) for UC preparations, a non-statistically significant difference (Table 5.2). In addition, a subjective assessment of the images indicate that UC EVs appear to be more electron dense than those isolated via SEC. Unfortunately, these indications come from a small number of preparations, additional preparations must be made to confirm or deny these theories, as well as assess and impact upon size, number of EVs.

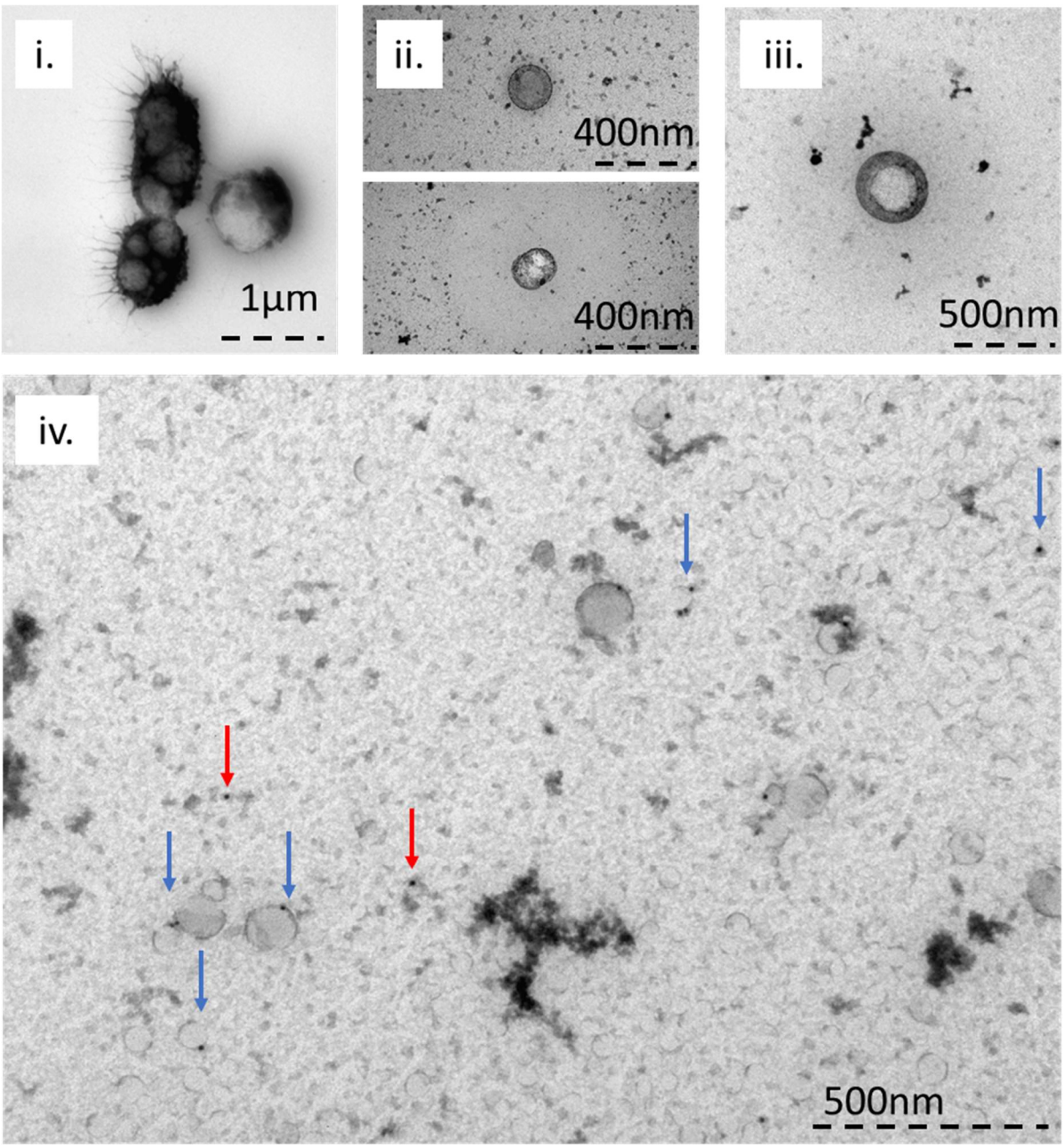

Figure 5.2: TEM technique development at EMBO Ceske Budjovice. (i) Simple negative staining on a formvar coated carbon grid imaged EV sized objects lacking in definition, and at very low concentration. Mean size 467.0 nm ± 127.3 n=3. (ii) Wheat germ antigen (WGA) used to encourage EV adhesion with some success, significant anomalous debris present. Adhesion appeared to be low, with very few EVs present on the grid. Mean size = 173 ± 14 nm (n=10). (iii) Poly L lysine was also assessed for the ability to increase EV adherence, again resulting in clearly defined spherical objects, sized 263.4 nm ± 45.34 (n=13), additional debris was also present, however this debris was visibly distinct from EV like objects, tending to be globular. Again, EV adhesion was low. (iv) Grids coated with poly L lysine, incubated with EVs, then labelled with anti CD63 antibodies, followed by protein A gold 10nm labelling of said antibodies, this showed an abundance of EV sized objects, with some excellent gold nanoparticle labelling. Mean size of all EV like objects = 119.4 nm ± 17.43 (n=66). Mean size of all EV like objects bound to a 10 nm gold particle = 67.0 nm ± 5.4 (n=19).

Table 5.1: Sizes obtained from TEM images obtained at EMBO Ceske Budjovice. Negative staining imaged the largest EV like objects, but also the fewest. The EV like objects that were tagged with protein A gold were smaller than any other form of imaging.

	Negative staining	Wheat Germ Antigen adhered	Poly L Lysine adhered	Poly L Lysine and protein A gold	Only EVs tagged with protein A gold
Mean	467.0	172.7	263.4	119.4	67.00
Std. Error	127.3	13.64	45.34	17.43	5.385
n=	3	10	13	66	19

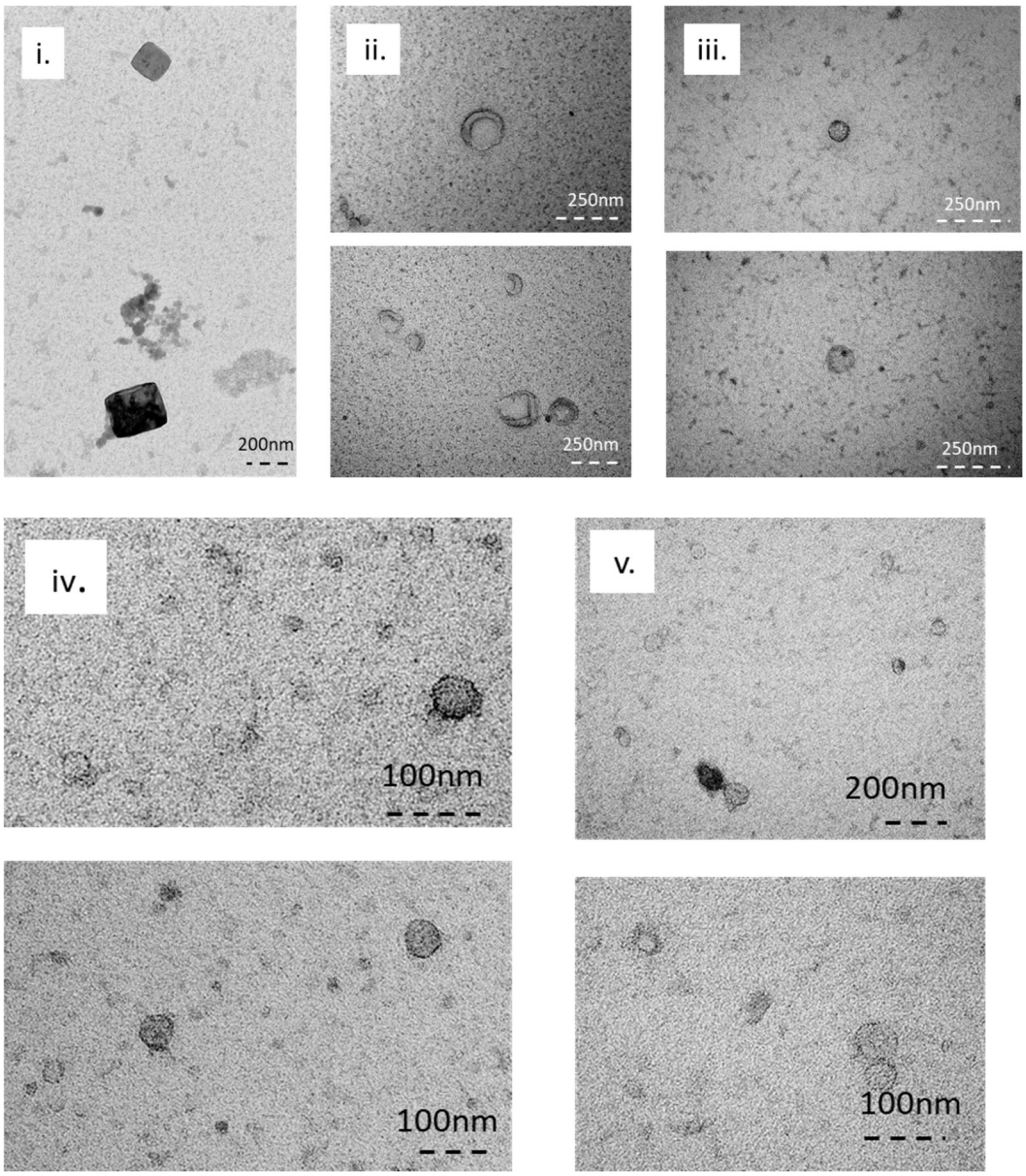

Figure 5.3: Technique application at the University of Birmingham. (i) Negative Control grid – PBS – Globular debris can be seen similar to debris in previous TEM images. Debris mean size 131.7 nm ± 12.8 (n=96). (ii) Liposome imaging – very few liposomes attached, those present appeared cup shaped. Reduced debris present. Liposome mean size 118.3 nm ± 9.8 (n=50).
(iii) Mineralising MC3T3 EVs – also very low concentration, with low background debris. Mean EV size 34.9 nm ± 1.9 (n=39). (iv) Human UC EVs – background debris increasingly present, additionally, EVs appear darker and more electron dense. Mean size 32.9 nm ± 1.9 (n=56). (v) Human SEC EVs – reduced electron density compared to (iv). Mean size 36.0 nm ± 1.2 (n=92).

Table 5.2: TEM object sizing at University of Birmingham. Debris present in negative control images was 131.7 ±12.8 nm, similar to reported EV sizing. MC3T3 and human EVs appeared to have similar sizes, but concentration in the SEC isolated population appears much greater.

	Negative control (PBS)	**Liposomes**	**Mineralising MC3T3 EVs**	**Human UC isolated EVs**	**Human SEC isolated EVs**
Mean	131.7	118.3	34.9	32.9	36.0
Std. Error	12.8	9.8	1.9	1.9	1.2
n=	96	50	39	56	92

5.3.2 Initial attempts to analyse EVs using optical trapping and Raman spectroscopy

Difference in EV composition is likely to impact their subsequent actions upon target tissues. Identifying any chemical differences in composition may be the first step in understanding these actions, and subsequently mimicking them in future treatments. If we are to utilise the significant impact that mineralising EVs have upon osteoblasts as seen in Figures 4.3 and 4.4, then highly resolved characterisation of EVs is required. Using Raman spectroscopy, we have attempted to identify the bonds present in EVs via their unique molecular fingerprint.

Mineralising osteoblast EVs often appear electron dense in TEM images [97] suggesting the presence of heavier nuclei. A likely source of these heavier nuclei may be phosphate and/or calcium, as they have been found present in EV like structures within multivesicular bodies within osteoblasts [81]. The presence of phosphate and calcium ions in EVs may have a direct impact upon their ability to induce mineralisation. This may be through providing the raw materials necessary for the formation of ACP, or due to the inhibitory or stimulatory effects nucleoside phosphates (ATP, ADP and AMP) have on various biological activities, affecting platelet aggregation [119], mineralisation and TNAP activity [152]. Identifying the molecular species present in EVs, and their relative ratios may be vital in understanding the activity of EVs in mineralisation, and therapeutical use.

Raman spectroscopy is an effective method of determining molecules present in samples by detecting the vibrational energies present in covalent bonds within the sample and has been previously used to distinguish between adenoside phosphates [153]. The work below illustrates our attempts to use Raman spectroscopy to interrogate EVs, using optical tweezers. This concept, previously demonstrated by Penders, *et al*. [169], traps individual EVs to obtain a profile of EV populations, for both non-mineralising and mineralising EVs. In turn, this should permit identification of components of mineralising vesicles that are key to their ability to enhance mineralisation.

Table 5.3: Likely Raman spectral bands that correspond to EVs. Raman signatures corresponding to protein, phosphates, carbonates, lipids, and nucleic acids, found in various literature sources.

Location of common peak (wavenumber cm^{-1})	Likely corresponding material	References
889-90	Protein bands	Movasaghi, Rehman, & Rehman, 2007 [172]
962-3	PO_4 symmetric stretching vibration	Cuscó *et al.*, 1998 De Aza *et al.*, 1997 [157,158] Kim *et al.,* 2002 [173]
	Phosphate symmetric stretching vibration of calcium hydroxyapatite	Silveira, *et al.*, 2002 [159]
1054-90	C-O and C-N stretching of proteins C-C vibrations of lipids and carbohydrates PO_2 − stretching of nucleic acids	Gualerzi *et al.*, 2017 [174]
	Carbonate symmetric stretching vibration of calcium carbonate apatite	Silveira, *et al.*, 2002 [159]
1130-1131	Various membrane lipids	Czamara *et al*., 2015 [175]
	C-C skeletal stretch transconformation. Phospholipid structural changes, Acyl chains, Palmitic acid, Fatty acid	Movasaghi, Rehman, & Rehman, 2007 [172]

Early attempts to optically trap individual EVs proved unsuccessful, with spectra appearing noisy and non-specific (Figure 5.4). It was possible to identify a peak at 1442 cm^{-1} which corresponds with CH_2/CH_3 scissoring in lipid molecules, but evidence for mineral bonds at 963 cm^{-1} (PO_4^{3-}) and 1072 cm^{-1} (CO_3^{2-}) was not present.

To understand why these results were unsatisfactory, it was decided to confirm that EVs can be effectively trapped using this system.

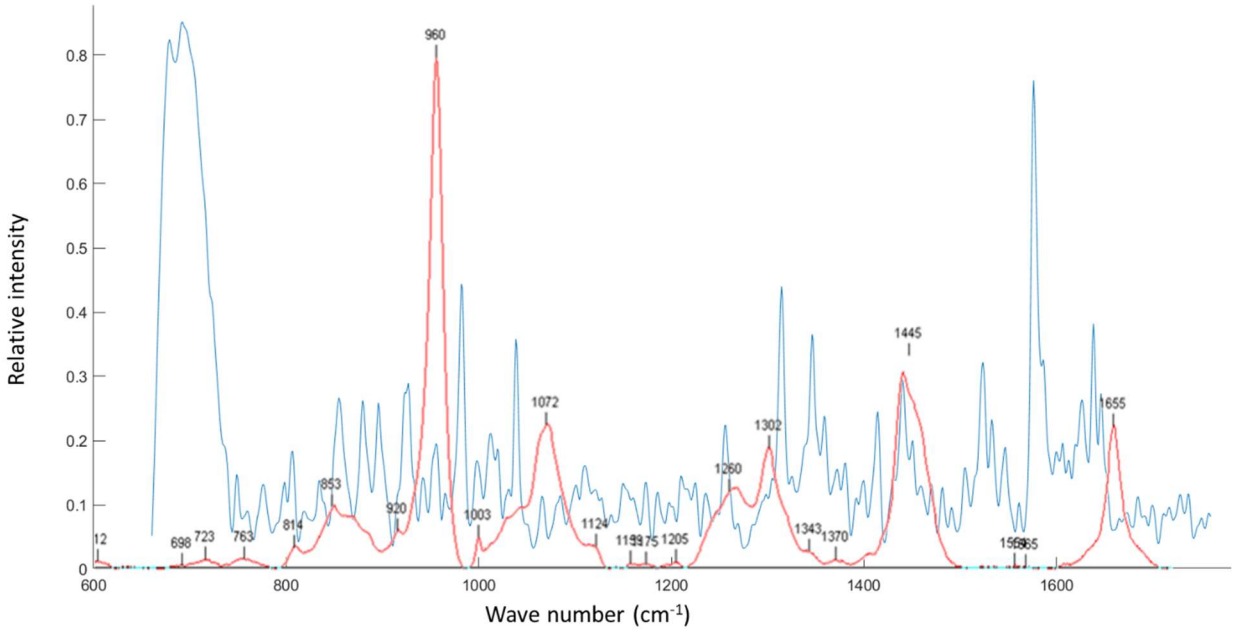

Figure 5.4: Raman spectra from initial attempts to optically trap EVs. It was thought that optically trapping individual (or small numbers) of EVs would provide greater definition to any changes in composition. The next step was to assess these MC3T3 EVs using a trapping laser, and simultaneously interrogating them with a Raman laser. Results from this (blue line) showed very little correlation with Raman of bone tissue (red line) apart from 1445 cm^{-1} which correspond to CH functional groups, commonly detected in lipids.

5.3.3 Troubleshooting optical trapping of EVs

To assess effectiveness of optical trapping EVs, phosphatidylcholine and cholesterol artificial liposomes were constructed (see methods). The liposomes were nanospheres constructed from a 30% cholesterol and 70% PC lipid bilayer offering a target object of similar size and profile to EVs. These spheres should display predictable Raman signatures [26] for cholesterol and phosphatidylcholine (see Table 5.4), two molecules believed to be present in EV membranes. Resulting data (Figure 5.5) showed no significant differences at wavenumbers expected corresponding to the mineral ions that should have been within the liposomes (960 – PO_4^{3-}, 1072 – CO_3^{2-}), nor lipid peaks for phosphatidylcholine or cholesterol (Table 5.4) indicating that the trapping methodology undertaken was not effective in trapping these control vesicles, and consequently, likely inappropriate for trapping EVs.

One hypothesis for the failure to detect Raman spectra whilst attempting to trap artificial liposomes (Figure 5.5), is that the trapping laser and the Raman laser were not focussed at the same focal volume. An experiment was designed to determine whether poor focus was to blame. The trapping laser would be focussed mid sample of a drop of suspended liposomes, and spectra taken, to determine if it was possible to trap and focus on liposomes. The focal point would then be moved downwards through the sample, to the surface of the aluminium foil slide, and spectral readings taken again. This should have the effect of gathering liposomes at the centre of the trapping laser, producing a strong spectral reading of multiple liposomes. These readings were repeated with the trapping laser switched off, to provide control spectra where no liposomes should be held in the focal point of the Raman laser. Results seen in Figure 5.6 show nearly identical spectra in all conditions, all of which show no lipid specific spectral peaks, (Table 5.4) indicating that this technique was not effective at trapping liposomes, and thus would not likely work with extracellular vesicles. Due to time constraints, this line of experimentation was halted.

Table 5.4: Lipid Raman assignments. Raman assignments corresponding to the various bonds found in phosphatidylcholine and cholesterol lipids. Data adapted from Czamara *et al.*, 2015 [175]

Phosphatidylcholine Raman band	Assignment
719	Choline stretching (symmetric)
876	Choline stretching (asymmetric)
1089	C-C stretching
1096	P-O stretching
1125	C-C stretching
1267	=CH deformation
1300	CH_2 twisting
1442	CH_2/CH_3 Scissoring
1657	C=C stretching
1737	C=O stretching

Cholesterol Raman band	Assignment
424	Bending CH_2 in ring
548	Bending CH_2 in ring
701	Deformation of ring
1087	C-C stretching
1130	C-C stretching
1178	C-C stretching
1442	CH_2/CH_3 Scissoring
1672	C=C stretching

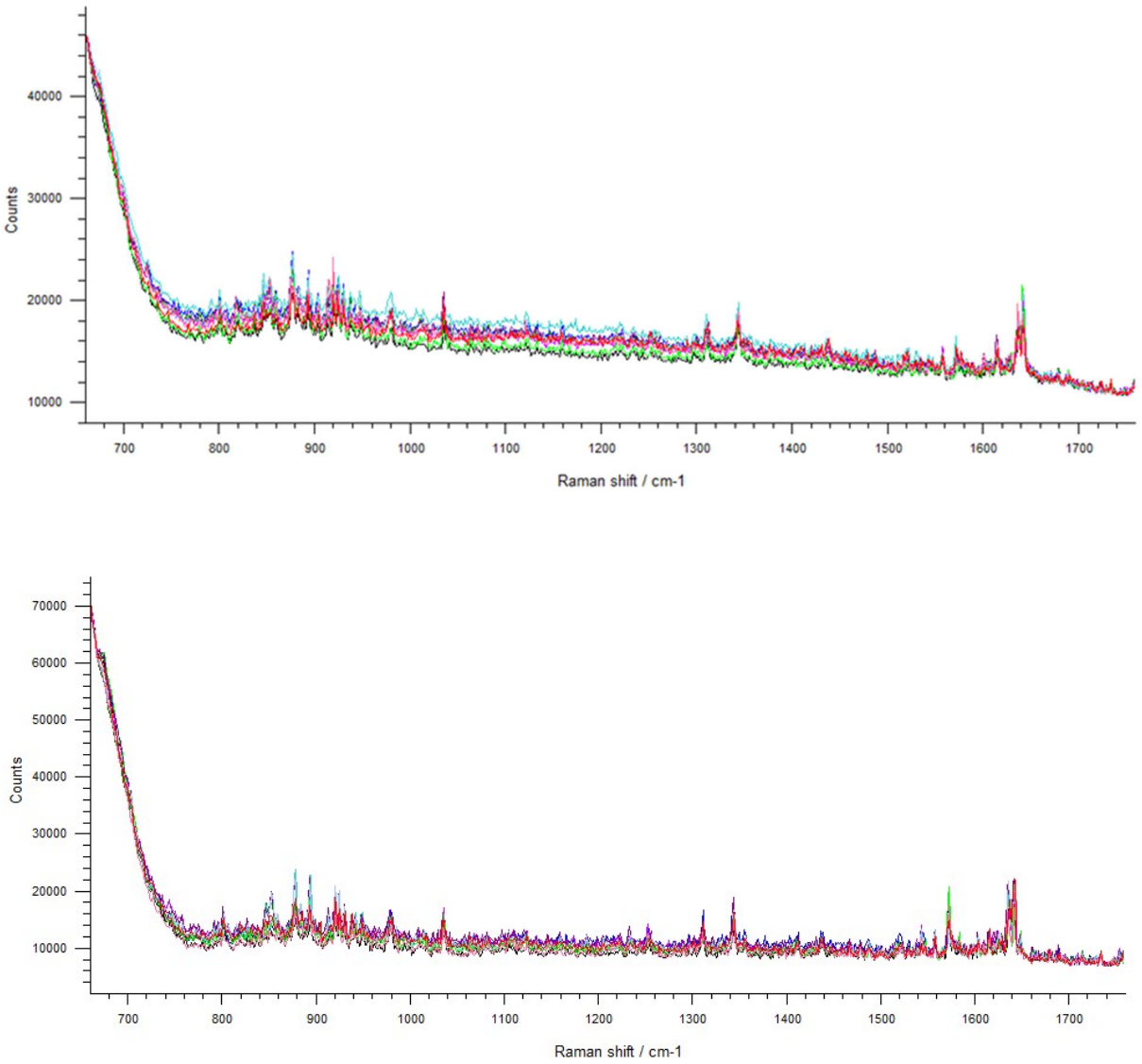

Figure 5.5: Empty liposomes and liposomes containing 1 mM Ca^{2+} and 1 mM HPO_4^{2-} trapped using optical tweezers. Effectiveness of detection of mineral compounds was assessed by comparing spectra from trapped empty liposomes, and liposomes formed in the presence of 1 mM Ca^{2+} and 1 mM HPO_4^{2-}, multiple Raman spectra were taken but there were no significant differences between the two spectra, and in particular, no significant increase in intensity at the wavenumbers expected (960 – PO_4^{3-}, 1072 – CO_3^{2-}).

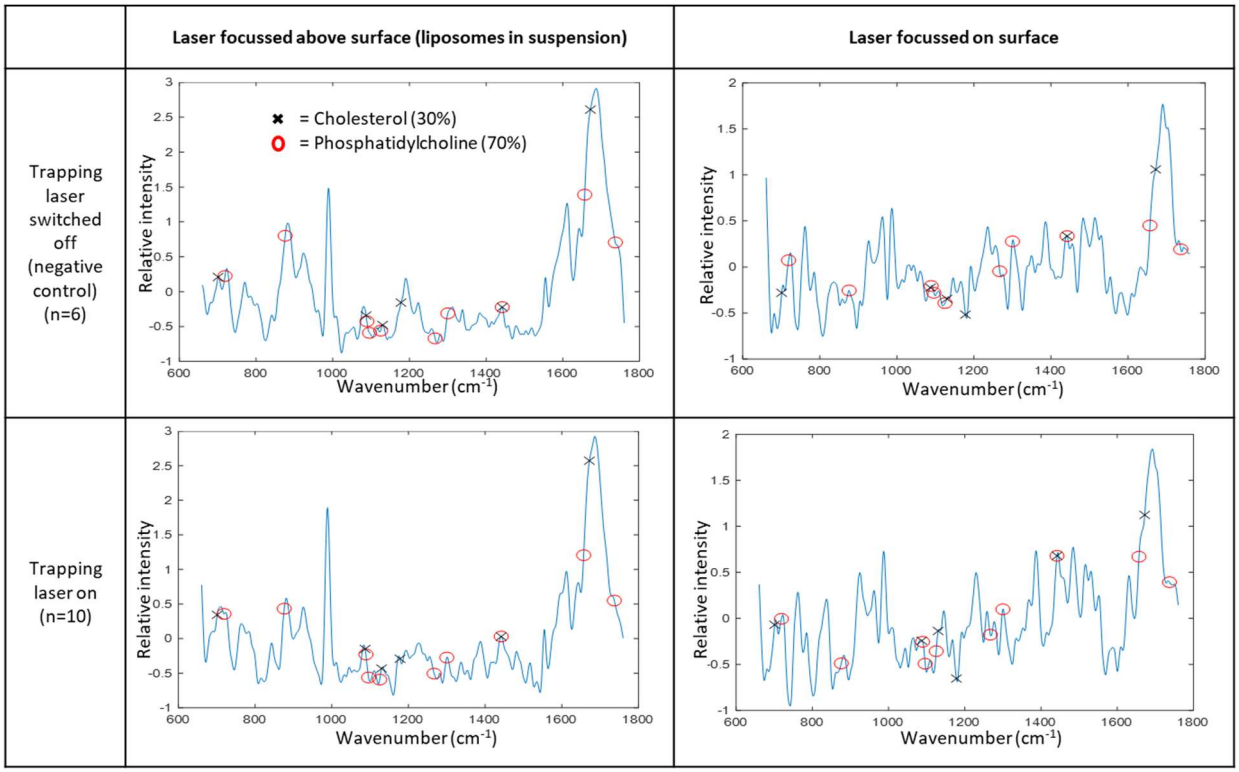

Figure 5.6: Attempts to troubleshoot optical tweezers with liposomes. The previous data (Figure 4.10) suggested that either the trapping laser was not functioning as intended, or that the liposomes were not enclosing the calcium and phosphate. To test the trapping laser, spectra taken with the laser on and off were compared, as well as focussed on a surface at the bottom of the liquid sample. Raman spectra obtained with the laser switched on or off produced extremely similar spectra, suggesting that the trapping laser was having no effect.

5.4 Discussion

Development of the TEM imaging methodology brought a previously absent tool to our laboratory. Whilst the technique is still imperfect, with a need to increase EV concentration in the images and the need to reduce foreign debris, the ability to use protein A gold nanoparticles targeting CD63, considered an EV marker, is valuable for confirming the presence and morphology of EVs (Figure 5.2).

The finding that our PAG labelled EVs tended to be smaller on average from structures assumed to be EVs in our other techniques (Table 5.1) highlights an interesting feature. CD63 is typically found with the late endosomal-lysosomal compartment within cells [176] , linking it with the exosomal release pathway via multivesicular bodies, this would explain the binding to smaller EVs, as exosomes are typically between 30-100 nm in size.

The technique developed in this manuscript had a further facet, the cup shaped nature of the imaged liposomes when compared to the human and murine EVs. The methylcellulose step in this technique is designed to create a structure to support the EVs during the TEM process, preventing collapse during the drying process and permitting them to retain their presumed in vivo spherical shape (Figure 5.2). It is possible that this methycellulose supporting structure is more effective in the presence of the proteins and sugars commonly found on the surface of EVs, than the relatively homogenous surface of liposomes.

Whilst the binding of PAG to EV like objects is promising, the presence of debris that binds CD63 poses many problems. Potential reasons for this binding are wide ranging and may include insufficient blocking prior to antibody incubation, non-specific binding, or the presence of CD63 within the debris (from cell or exosome degradation). The presence of this debris will interfere with automated attempts to characterise collected EV populations, which may not be specific enough to differentiate between cell debris and intact EVs. Further work should be undertaken to determine the source of the debris, whether it is from the TEM grid preparation components (poly-L-lysine, PBS, fish skin gelatin, anti CD63 antibody, protein A gold, uranyl acetate or methylcellulose), or artefacts in the EV sample from the isolation process. The

presence of somewhat similar globular debris in the PBS images offers some hope that this debris may be component, not sample related.

Figure 5.3iv & v appear to suggest some differences in absorbance of electron beam between EVs, with potentially darker spheres apparent in the UC sample, suggesting the presence of heavier elements such as calcium or phosphorous. As both samples were isolated from the same source, this suggests the isolation method may influence EV contents or may be selecting differing populations. Ultracentrifugation is the most common method of EV separation from conditioned media [177] and involves spinning EV conditioned media sequentially at significantly high G forces (see methods and materials section). This method includes significantly higher forces than SEC, and may cause disruption, aggregation, and destruction of EVs, as well as proportionally high sample loss [178,179]. Unfortunately, the observations we suggest here come from a small number of preparations, this number must be increased, and subjective criteria decided regarding electron density and debris to elucidate these issues, as well as assess and impact upon size, number of EVs.

Our attempts to characterise individual EVs using Raman spectroscopy and molecular tweezers was ultimately unsuccessful, likely due to a lack of resolution in the ability to fine tune the focus of the Raman laser to that of the trapping laser. An inability to trap EVs on the surface of the sample slide as illustrated in Figure 5.6 suggests that the equipment available was not effective in directing EVs as desired. Further work in this area may benefit from the use of positively charged gold-silver nanostar nanoparticles SERS [180], which can significantly boost the Raman signal from nanoparticles and would be extremely useful. The presence of lipid related peaks in the liposome Raman spectra conflict with the idea that mismatched focal volumes are to blame for the EV Raman failure. This may be explained by the concentration of liposomes in this sample, as this was orders of magnitude greater than the EV solution, due to the ease of production of liposomes when compared to the production and separation of EVs.

5.5 Conclusion

Utilisation of XRF offers unique insights into the impact of EVs on the mineralisation process, rapidly increasing the deposition of mineral in a more homogenous layer across the culture. Raman spectroscopy of EVs was challenging when combined with molecular tweezers, however the effectiveness of the process when used on liposome controls offers some promise that these issues can be overcome. The development of high-quality electron microscopy techniques and labelling is a significant positive for the further investigation of EVs in this laboratory.

Chapter 6 : Discussion and further work

6.1 General Overview

Human bone is a complex, adaptive living tissue, tightly controlled in its manufacture and serving many functions in health. Dysfunction in the formation of bone, whether through injury, aging or disease can lead to severely impacted quality of life, and in severe cases, death. The extraordinary strength of bone comes from a highly regulated, hierarchical construction process that is still poorly understood, and not yet effectively replicated *in vivo*. Improving the current knowledge around this early mineralisation of bone is vital to reduce the impact of bone related issues in increasingly aged populations globally.

It is believed that osteoblast derived extracellular vesicles play an important part in the formation and mineralisation of bone *in vivo*, but this role is presently unclear. Extracellular vesicles are composed of lipid bilayers, and contain a highly heterogenous mix of proteins, nucleic acids, and other molecules, both within and upon the surface, and show promising therapeutic potential. In addition to allowing intracellular communication, EVs are thought to act as nucleation sites for mineralisation, it is likely that some of the molecular contents of osteoblast EVs play an important role in the mineralisation process, discussed in depth in Chapter 1. Clarifying the molecular cargo of osteoblast EVs may provide insight into their roles in mineralisation, and therefore offer new therapeutic insights.

In Chapter 2 we utilise the existing method of X ray fluorescence in a novel way to probe the changes in mineral composition occurring in the early stages of mineralisation of *in vitro* cell culture. Beginning with a validation of XRF as a quantitative measure, it showed a strong correlation between the elemental calcium to phosphate ratio and the XRF signal ratio of the two elements ($R^2 = 0.984$) (Figure 2.2). This method was then utilised to characterise the calcium and phosphate presence in MC3T3 mineralisation, across multiple timepoints in a 21-day period. These results (Figure 2.4) showed a very low calcium signal in the culture, until day 17 whereby it increased greatly, whereas phosphorous was present in small amounts in early stages, increasing greatly as mineralisation progressed. Interestingly, this

conflicts with the gold standard method of calcium quantification, alizarin red, which detected steadily increasing calcium content as the culture matured (Figure 2.3). Analysis of the calcium : phosphate signal ratio of the mature mineralised cells (day 21) suggested an elemental ratio comparable to pure monocalcium phosphate monohydrate, which has an elemental ratio of 1 calcium to 2 phosphate ions. This ratio is far short of the mineral which typically makes up a large proportion of bone, hydroxyapatite, which has an elemental ratio of 5 calcium ions to 3 phosphate ions. This may suggest that mineralisation is a progression through various calcium phosphate phases, initially being calcium deficient, until the latter stages of mineralisation. It must be taken into consideration that these ratios are obtained from the whole culture, whilst mineralisation does not display a uniform spread of mineral, instead occurring in localised nodules of high calcium and phosphate concentrations. We therefore proceeded to investigate the calcium phosphate ratio across the width of one of these mineralised nodules and observed that these areas had an increased Ca:P ratio. The highest observation suggests an elemental composition of 1 calcium ion to 1 phosphorous ion, similar to calcium pyrophosphate or brushite, this was found on the edge of a mineral nodule, likely the location of new mineral formation. These data alone are not sufficient to conclude that mineralisation is occurring through intermediate calcium phosphate species. Another reason may be that HA is present but phosphate from additional sources such as ATP from rapidly metabolising cells is reducing the apparent elemental ratio.

In Chapter 3 we investigated the utility of Raman spectroscopy to determine the presence of phosphate and carbonate in demineralised bone sections, with the aim of using Raman to detect these compounds in extracellular vesicles. Data indicated that both signals were affected by demineralisation, with phosphate signal correlating well with the amount of non-organic residue left behind after combustion of the organic component of the bone (R^2 = 0.956). Comparison of non-organic residue left behind after thermogravimetric analysis, with the two methods discussed, Raman spectroscopy and XRF, suggests that XRF correlates very closely with TGA, and Raman, less so. The reduced correlation observed with Raman was likely due to the methods employed in the experiments, which produced a heterogeneous bone sample for analysis, not well suited for the high resolution, low throughput method of Raman

spectroscopy available here. These drawbacks would not be present when observing cell culture mineralisation or EV characterisation and would likely suit Raman spectroscopy better. Both methods are likely to be useful in the investigation of early mineralisation if used in conjunction, as whilst XRF is useful in quantifying the presence of calcium and phosphate ions, Raman can detect more refined information on the compounds present.

These methodologies were brought together in Chapter 4 to characterise EVs and their impact on mineralisation. Firstly, quantification of EV production was assessed, with increased EV production observed in mineralising cells, as well as increased extracellular matrix deposition. EV production was reduced at day 21, potentially linked to the glycolysis pathway and subsequent reduction in oxidative stress reported by Misra *et al.*[168]. Supplementation of EVs into cell culture media resulted in rapid mineralisation when compared to non-supplemented cultures, and a more uniform spread of mineral, potentially supporting the theory that they act as nucleation sites in mineralisation.

Characterisation of EVs by novel TEM techniques in Chapter 5 revealed differences in EV characteristics dependent upon the method of mineralisation, with ultracentrifugation appearing to provide more electron dense EVs. Additionally, we describe an effective method of identifying and visualising exosomes using gold nanoparticles. We also identify issues faced with unwanted debris in EV isolation methods, potentially exacerbated by the extreme forces necessary in ultracentrifugation.

Finally, attempts to individually characterise mineralising EVs using optical tweezers coupled with Raman spectroscopy was ultimately unsuccessful, with the identification of the inability to couple the focal beam of the tweezers with that of the Raman laser being the likely source of frustration.

6.2 Further work

Whilst this thesis represents a significant body of work, it provides several interesting avenues for future work, here we detail a few of these options.

The conflicting results between alizarin red, which indicate calcium is present in early stages of mineralisation, and XRF which showed otherwise, is worthy of further investigation. As mentioned in Chapter 2, alizarin red can also signal the presence of other metallic ions, XRF can detect these elements, if they are present in significant amounts, they may play a previously unexpected role in intermediate phases in early mineralisation. Fortunately, the XRF methodology designed in this thesis offers a simple solution to investigating these alternative elements. The collection of XRF spectra gathers data on the presence of elements across the periodic table in each measurement, therefore it would be relatively simple to reinterpret spectral data for the presence of magnesium, manganese, iron etc. If evidence of their presence is discovered, then would yield an interesting insight, hitherto unseen, into the processes involved in early-stage mineralisation.

Further investigation of the calcium : phosphate status across individual mineralising nodules is another interesting avenue of research. By looking at single nodules, we are likely to see mineral in different stages of formation. The centre of a nodule is likely to be the nucleating centre of mineral formation, and therefore, the most mature stage. Comparison with mineral on the edge of a nodule, which is likely to be the most recently formed mineral, may inform about how mineral formation progresses from amorphous stages to developed HA phase. The observations detailed in this thesis illustrated increased Ca:P ratio at the edges of mineral nodules, likely to be areas of early/ongoing mineral deposition, and potentially locations of amorphous phosphate species, which may explain high Ca:P ratios. Further, repeat investigation should reveal precise stoichiometry of these areas, which may offer further clues to the progression of CaP species through early mineralisation.

Significant amounts of elemental composition data are obtained during XRF scans, containing data across hundreds of elements. Utilising computer science techniques, including principal component analysis of these spectral data cubes may identify significant differences linked with mineral maturity. Utilising the full spectra, rather

than focussing only on calcium and phosphate, may bring to light significant changes in other elemental ratios, and may shed light on the previously mentioned conflict with Alizarin red. If increased iron levels are detected at newly formed mineral, or cells bordering mineralised nodules, this may explain why results obtained by alizarin red disagreed with XRF, as it is this iron that alizarin red is detecting, as opposed to calcium.

Coupling XRF with Raman investigation of mineralising cell cultures may offer unique insights into the species present. Localised comparison of XRF elemental mapping with Raman detection of carbonate and phosphate bonds may enable us to pair changes in phosphate and carbonate concentrations with elemental ion changes, providing an improved picture of the mineral species present in progressive mineralisation. Preliminary investigations into this were carried out, however, the materials typically used in cell culture (polystyrene plastic plates or glass cover slips) were not compatible with both measurement methods, with glass providing significant background calcium during XRF, and polystyrene producing significant interference during Raman spectroscopy. Alternative cell culture surfaces would be needed, such as quartz, to allow effective quantitative comparison.

The attempts at optical trapping in this thesis were ultimately unable to obtain spectra from individual vesicles. To increase the chances of success in future, any further work must be performed using a more highly resolved trapping laser, with a smaller focal volume. Work performed by Penders *et al.* [169] has shown that high throughput analysis is possible, with adequate equipment. To improve on the results obtained using that method, it may be possible to increase the signal obtained from EVs in solution, using surface enhanced Raman spectroscopy. This method increases the strength of Raman signals, utilising positively charged gold-silver nanostar nanoparticles [180], or 3D nanostructures [181]. This may negate the inherent difficulties encountered by the low concentration of osteoblast EVs obtained in standard EV separation techniques, permitting stronger signals to be obtained from each successful interrogation.

The XRF data observed in Chapter 4.3.4 illustrates the significantly different mineral deposition characteristics of MC3T3 cells which are supplemented with EVs. In the discussion of that chapter, it is hypothesised that the supplemented EVs may be acting

as mineralisation accelerants, acting as nucleation centres for mineral formation. A method of investigating this may be to tag the supplemental EVs with a nanoparticle, such as the gold nanoparticles used in the TEM work (Chapter 5.2.5) that is highly visible to XRF, marking locations where EVs have adhered to the ECM. Additionally, it is hypothesised that the uniform appearance of Ca and P distribution is due to the high EV particle number supplementation, permitting the formation of mineral across the sample, simultaneously, unlike the non-EV supplemented cultures. If these cultures are supplemented with tagged EVs, at a much lower concentration than 10 µg/mL then interrogated by XRF earlier in the mineralisation process, it may be possible to observe early nodule formation. The objective would be to witness nodule formation earlier in the process, before the culture becomes uniformly covered by CaP mineral, and if these nodules are identified, the location, or absence of a tagging nanoparticle. If mineral nodule formation appears to correlate with the location of these tagged EVs, then this may support the theory of EVs as mineral nucleation sites.

The vesicles utilised in this study were obtained using sequential ultracentrifugation to separate EVs from culture media obtained from 2D cultured cells. These 2D culture methods are primarily used due to ease of use, decades of existing literature, and experimental refinement. As discussed previously, these techniques are not representative of physiological conditions. The growth surface on one side of the cell being a rigid, impenetrable surface, and the other side, an open, fluid environment, with no adhesion possible. Compared to *in vivo* growth of osteoblasts, within a 3D extracellular matrix with vastly increased cellular adhesion points, 2D culture presents a highly artificial model, albeit one that has produced decades of important research data. Modern manufacturing techniques, such as 3D printing [182,183], has made 3D culture methods more accessible. Research has shown that EVs obtained from these systems display a significantly closer RNA phenotype to EVs obtained from live animals (96% similarity) when compared to those obtained from 2D systems (80% similarity) [184]. Confirmation of the mineralising potential of EVs taken from more physiologically relevant 3D culture systems is an important step in the development of EV derived therapeutics, to ensure that the potential witnessed in 2D derived EVs is not an artifact of the production process. Comparison of the *in vitro* effects of 2D vs 3D culture EVs on mineralisation, perhaps using the XRF and Raman spectroscopy methodologies

developed in this thesis, would provide insight valuable to future EV research. The two production methodologies, 3D being more physiologically relevant, but potentially more expensive, technically demanding and less robustly researched than 2D production, will have benefits and drawbacks that need to be assessed.

Alongside this, the methodologies used for EV collection in this thesis proved time consuming and insufficient, even for the small-scale investigation of effect upon mineralising cells, detailed in Chapter 4. If EVs are to be robustly investigated in significant number, and used in treatment therapies, methods of scaling up EV production must be investigated. The International Society for Extracellular Vesicles produced a report entitled "Large-scale production of extracellular vesicles: report on the "massivEVs" ISEV workshop" which discusses in detail the challenges that are being faced. Cell culture in large bioreactor systems holds promise as a solution[185], often utilising 3D culture and continuous flow systems. The widespread employment of a 'gold standard' methodology of large-scale EV production appears a long way off however. It will require significant investigation into the influence of particular methods upon reproducibility and efficacy of the resultant EV population.

We have demonstrated the ability to automate image analysis and quantification of mineralisation characteristics, described in Chapter 2.3.5. These methods permit the automated quantification of nodule number and area, using images obtained by XRF. A non-subjective method of measuring these properties, that can be utilised in a high throughput and automated manner, is an important baseline for development of a gold standard in mineralisation characterisation. The establishment of a standardised method of collecting these data allows statistical comparison of the effects of therapeutic treatments or disease states across institutions and increases potential data set size. These methods may also be useful for comparison of the efficacy of EVs produced in differing systems, as previously discussed, as this will produce a high volume of data, which will need to be compared across multiple data sets.

6.3 Overall summary

The aim of this work was to investigate new techniques for characterisation of the early stages of biological mineralisation. We have successfully demonstrated the application of the existing technology of x ray fluorescence to early-stage mineralising cell cultures, uncovering interesting information regarding the elemental composition of mineral deposited early in the process, which appears to differ when compared to mature bone. Development of novel imaging and labelling techniques for the nano sized EVs is an improvement on current negative staining techniques, permitting clearer images. Attempts to utilise optical tweezers in combination with Raman spectroscopy were met with limited success, highlighting the difficulty of obtaining single molecule information from osteoblast derived EVs, but some success with liposomes suggests these obstacles can be overcome. Future work combining the techniques developed in this thesis may provide important information on the process of early mineralisation.

Reference list / Bibliography

1. Fonseca, H., Moreira-Gonçalves, D., Coriolano, H.-J. A. & Duarte, J. A. Bone quality: the determinants of bone strength and fragility. *Sports Med* **44**, 37–53 (2014).

2. MatWeb Material Property Data. Flexural Strength Testing of Plastics. *Flexural Strength Testing of Plastics* https://www.matweb.com/reference/flexuralstrength.aspx (2023).

3. Marini, J. C. *et al.* Osteogenesis imperfecta. *Nat Rev Dis Primers* **3**, 17052 (2017).

4. Saito, T., Arsenault, A. L., Yamauchi, M., Kuboki, Y. & Crenshaw, M. A. Mineral induction by immobilized phosphoproteins. *Bone* **21**, 305–311 (1997).

5. Gower, L. & Elias, J. Colloid assembly and transformation (CAT): The relationship of PILP to biomineralization. *J Struct Biol X* **6**, 100059 (2022).

6. Anderson, H. C. Electron microscopic studies of induced cartilage development and calcification. *J Cell Biol* **35**, 81–101 (1967).

7. Peress, N. S., Anderson, H. C. & Sajdera, S. W. The lipids of matrix vesicles from bovine fetal epiphyseal cartilage. *Calcif Tissue Res* **14**, 275–281 (1974).

8. Genge, B. R., Wu, L. N. Y. & Wuthier, R. E. Identification of phospholipid-dependent calcium-binding proteins as constituents of matrix vesicles. *Journal of Biological Chemistry* **264**, 10917–10921 (1989).

9. Wolf, P. The nature and significance of platelet products in human plasma. *Br J Haematol* **13**, 269–288 (1967).

10. Bonucci, E. Fine structure of early cartilage calcification. *Journal of Ultrasructure Research* **20**, 33–50 (1967).

11. Yáñez-Mó, M. *et al.* Biological properties of extracellular vesicles and their physiological functions. *J Extracell Vesicles* **4**, 27066 (2015).

12. Hampson, D. Facial injury: A review of biomechanical studies and test procedures for facial injury assessment. *J Biomech* **28**, 1–7 (1995).

13. Copp, D. H. & Shim, S. S. The homeostatic function of bone as a mineral reservoir. *Oral Surgery, Oral Medicine, Oral Pathology* **16**, 738–744 (1963).

14. Shimada, T. *et al. Cloning and Characterization of FGF23 as a Causative Factor of Tumor-Induced Osteomalacia*. vol. 98 www.pnas.orgcgidoi10.1073pnas.101545198 (2001).

15. Capulli, M., Paone, R. & Rucci, N. Osteoblast and osteocyte: Games without frontiers. *Arch Biochem Biophys* **561**, 3–12 (2014).

16. Baron, R., Neff, L., Van, P. T., Nefussi, J. R. & Vignery, A. Kinetic and cytochemical identification of osteoclast precursors and their differentiation into multinucleated osteoclasts. *Am J Pathol* **122**, 363 (1986).

17. Yasuda, H. *et al.* Osteoclast differentiation factor is a ligand for osteoprotegerin/osteoclastogenesis-inhibitory factor and is identical to TRANCE/RANKL. *Proc Natl Acad Sci U S A* **95**, 3597–3602 (1998).

18. Li, Y.-P., Chen, W., Liang, Y., Li, E. & Stashenko, P. Atp6i-deficient mice exhibit severe osteopetrosis due to loss of osteoclast-mediated extracellular acidification. *Nat Genet* **23**, 447–451 (1999).

19. Florencio-Silva, R., Sasso, G. R. da S., Sasso-Cerri, E., Simões, M. J. & Cerri, P. S. Biology of Bone Tissue: Structure, Function, and Factors That Influence Bone Cells. *Biomed Res Int* **2015**, 421746 (2015).

20. Palumbo, C., Palazzini, S. & Marotti, G. Morphological study of intercellular junctions during osteocyte differentiation. *Bone* **11**, 401–406 (1990).

21. Civitelli, R. Cell-cell communication in the osteoblast/osteocyte lineage. *Arch Biochem Biophys* **473**, 188–192 (2008).

22. Bailey, A. J. Molecular mechanisms of ageing in connective tissues. *Mech Ageing Dev* **122**, 735–755 (2001).

23. Tencer, A. F. & Johnson, K. D. Biomechanics in Orthopedic Trauma: Bone Fracture and Fixation. in (1994).

24. Kronenberg, H. M. Developmental regulation of the growth plate. *Nature* **423**, 332–336 (2003).

25. Percival, C. J. & Richtsmeier, J. T. Angiogenesis and intramembranous osteogenesis. *Developmental Dynamics* vol. 242 909–922 Preprint at https://doi.org/10.1002/dvdy.23992 (2013).

26. Hughes, E. A. B., Robinson, T. E., Bassett, D. B., Cox, S. C. & Grover, L. M. Critical and diverse roles of phosphates in human bone formation. *J Mater Chem B* **7**, 7460–7470 (2019).

27. Eanes, E. D., Gillessen, I. H. & Posnor, A. S. Intermediate States in the Precipitation of Hydroxyapatite. *Nature* **208**, 365–367 (1965).

28. Hall, J. E. (John E. *Guyton and Hall Textbook of Medical Physiology / John E. Hall. Textbook of medical physiology* (Philadelphia, PA : Elsevier, 2016, 2016).

29. Onuma, K. & Ito, A. Cluster Growth Model for Hydroxyapatite. *Chemistry of Materials* 3346–3351 (1998) doi:10.1021/cm980062c.

30. Landis, W. J., Song, M. J., Leith, A., McEwen, L. & McEwen, B. F. Mineral and organic matrix interaction in normally calcifying tendon visualized in three dimensions by high-voltage electron microscopic tomography and graphic image reconstruction. *J Struct Biol* **110**, 39–54 (1993).

31. Gupta, H. S. *et al.* Cooperative deformation of mineral and collagen in bone at the nanoscale. *Proc Natl Acad Sci U S A* **103**, 17741–17746 (2006).

32. Stammeier, J. A., Purgstaller, B., Hippler, D., Mavromatis, V. & Dietzel, M. In-situ Raman spectroscopy of amorphous calcium phosphate to crystalline hydroxyapatite transformation. *MethodsX* **5**, 1241–1250 (2018).

33. Lotsari, A., Rajasekharan, A. K., Halvarsson, M. & Andersson, M. Transformation of amorphous calcium phosphate to bone-like apatite. *Nat Commun* **9**, (2018).

34. Suzuki, O., Kamakura, S. & Anada, T. Conversion of octacalcium phosphate into hydroxyapatite and bone regeneration. in *Key Engineering Materials* vols 361-363 II 993–996 (Trans Tech Publications Ltd, 2008).

35. Johnsson, M. S.-A. & Nancollas, G. H. The role of brushite and octacalcium phosphate in apatite formation. *Critical Reviews in Oral Biology & Medicine* **3**, 61–82 (1992).

36. Xin, R., Leng, Y. & Wang, N. HRTEM Study of the Mineral Phases in Human Cortical Bone. *Adv Eng Mater* **12**, B552–B557 (2010).

37. Crane, N. J., Popescu, V., Morris, M. D., Steenhuis, P. & Ignelzi, M. A. Raman spectroscopic evidence for octacalcium phosphate and other transient mineral species deposited during intramembranous mineralization. *Bone* **39**, 434–442 (2006).

38. Faibish, D., Ott, S. M. & Boskey, A. L. *Mineral Changes in Osteoporosis A Review*.

39. Wegst, U. G. K., Bai, H., Saiz, E., Tomsia, A. P. & Ritchie, R. O. Bioinspired structural materials. *Nat Mater* **14**, 23–36 (2015).

40. Jee, S. S., Thula, T. T. & Gower, L. B. Development of bone-like composites via the polymer-induced liquid-precursor (PILP) process. Part 1: Influence of polymer molecular weight. *Acta Biomater* **6**, 3676–3686 (2010).

41. Bentov, S., Weil, S., Glazer, L., Sagi, A. & Berman, A. Stabilization of amorphous calcium carbonate by phosphate rich organic matrix proteins and by single phosphoamino acids. *J Struct Biol* **171**, 207–215 (2010).

42. Price, P. A., Toroian, D. & Lim, J. E. Mineralization by inhibitor exclusion: the calcification of collagen with fetuin. *J Biol Chem* **284**, 17092–17101 (2009).

43. Gower, L. B. & Odom, D. J. Deposition of calcium carbonate films by a polymer-induced liquid-precursor (PILP) process. *J Cryst Growth* **210**, 719–734 (2000).

44. Xu, Y. *et al.* Microscopic structure of the polymer-induced liquid precursor for calcium carbonate. *Nat Commun* **9**, 1–12 (2018).

45. Thula, T. T. *et al.* Mimicking the Nanostructure of Bone: Comparison of Polymeric Process-Directing Agents. *Polymers* vol. 3 10–35 Preprint at https://doi.org/10.3390/polym3010010 (2011).

46. Zou, Z. *et al.* Additives influence the phase behavior of calcium carbonate solution by a cooperative ion-association process. *J Mater Chem B* **6**, 449–457 (2018).

47. Deshpande, A. S. & Beniash, E. Bio-inspired Synthesis of Mineralized Collagen Fibrils. *Cryst Growth Des* **8**, 3084–3090 (2008).

48. Song, Q. *et al.* Contribution of biomimetic collagen-ligand interaction to intrafibrillar mineralization. *Sci Adv* **5**, 1–12 (2019).

49. Qi, Y. *et al.* Effects of Molecular Weight and Concentration of Poly(Acrylic Acid) on Biomimetic Mineralization of Collagen. *ACS Biomater Sci Eng* **4**, 2758–2766 (2018).

50. Birdi-Chouhan, G. *et al.* Soluble silicon patterns and templates: Calcium phosphate nanocrystal deposition in collagen type 1. *RSC Adv* **6**, 99809–99815 (2016).

51. Gajjeraman, S., Narayanan, K., Hao, J., Qin, C. & George, A. Matrix macromolecules in hard tissues control the nucleation and hierarchical assembly of hydroxyapatite. *J Biol Chem* **282**, 1193–1204 (2007).

52. Rodriguez, D. E. *et al.* Multifunctional role of osteopontin in directing intrafibrillar mineralization of collagen and activation of osteoclasts. *Acta Biomater* **10**, 494–507 (2014).

53. Saxena, N. *et al.* Comparison of Synthetic vs. Biogenic Polymeric Process-Directing Agents for Intrafibrillar Mineralization of Collagen. *Polymers (Basel)* **14**, (2022).

54. Wang, Z. *et al.* Toward the Understanding of Small Protein-Mediated Collagen Intrafibrillar Mineralization. *ACS Biomater Sci Eng* **6**, 4247–4255 (2020).

55. Bassett, D. C., Grover, L. M., Müller, F. A., McKee, M. D. & Barralet, J. E. Serum protein controlled nanoparticle synthesis. *Adv Funct Mater* **21**, 2968–2977 (2011).

56. He, G. & George, A. Dentin matrix protein 1 immobilized on type I collagen fibrils facilitates apatite deposition in vitro. *J Biol Chem* **279**, 11649–11656 (2004).

57. Chen, Y., Bal, B. S. & Gorski, J. P. Calcium and collagen binding properties of osteopontin, bone sialoprotein, and bone acidic glycoprotein-75 from bone. *J Biol Chem* **267**, 24871–24878 (1992).

58. Sfeir, C., Campbell, P., Jadlowiec, J. A. & Kumta, P. Method of inducing biomineralization method of inducing bone regeneration and methods related thereof. (2007).

59. Kaplan, DL., Huang, J., Wong, CPF., Naik, R. & George, A. Fibrous protein fusions and use thereof in the formation of advanced organic/inorganic composite materials. (2008).

60. Goldberg, H. A., Hunter, G. K. & Tye, C. E. Bone sialoprotein collagen-binding peptides. (2009).

61. Wang, Y. *et al.* Synergistic intrafibrillar/extrafibrillar mineralization of collagen scaffolds based on a biomimetic strategy to promote the regeneration of bone defects. *Int J Nanomedicine* **11**, 2053–2067 (2016).

62. Wang, Y. *et al.* Using biomimetically mineralized collagen membranes with different surface stiffness to guide regeneration of bone defects. *J Tissue Eng Regen Med* **12**, 1545–1555 (2018).

63. Genge, B. R., Wu, L. N. Y. & Wuthier, R. E. Mineralization of annexin-5-containing lipid-calcium-phosphate complexes: modulation by varying lipid composition and incubation with cartilage collagens. *J Biol Chem* **283**, 9737–9748 (2008).

64. Raposo, G. & Stoorvogel, W. Extracellular vesicles: Exosomes, microvesicles, and friends. *Journal of Cell Biology* **200**, 373–383 (2013).

65. Zeringer, E. *et al.* Methods for the extraction and RNA profiling of exosomes. *World J Methodol* **3**, 11–18 (2013).

66. Enderle, D. *et al.* Characterization of RNA from exosomes and other extracellular vesicles isolated by a novel spin column-based method. *PLoS One* **10**, e0136133 (2015).

67. Théry, C. *et al.* Exosomes: composition, biogenesis and function. *Nat Rev Immunol* **2**, 569–579 (2002).

68. Valadi, H. *et al.* Exosome-mediated transfer of mRNAs and microRNAs is a novel mechanism of genetic exchange between cells. *Nat Cell Biol* **9**, 654–659 (2007).

69. Skog, J. *et al.* Glioblastoma microvesicles transport RNA and proteins that promote tumour growth and provide diagnostic biomarkers. *Nat Cell Biol* **10**, 1470–1476 (2008).

70. Holme, P. A. *et al.* Shear-induced platelet activation and platelet microparticle formation at blood flow conditions as in arteries with a severe stenosis. *Arterioscler Thromb Vasc Biol* **17**, 646–653 (1997).

71. Perkumas, K. M., Hoffman, E. A., McKay, B. S., Allingham, R. R. & Stamer, W. D. Myocilin-associated exosomes in human ocular samples. *Exp Eye Res* **84**, 209–212 (2007).

72. Poliakov, A., Spilman, M., Dokland, T., Amling, C. L. & Mobley, J. A. Structural heterogeneity and protein composition of exosome-like vesicles (prostasomes) in human semen. *Prostate* **69**, 159–167 (2009).

73. Zhou, Y. *et al.* Exosomes released by human umbilical cord mesenchymal stem cells protect against cisplatin-induced renal oxidative stress and apoptosis in vivo and in vitro. *Stem Cell Res Ther* **4**, 34 (2013).

74. de Jong, O. G., van Balkom, B. W. M., Schiffelers, R. M., Bouten, C. V. C. & Verhaar, M. C. Extracellular vesicles: potential roles in regenerative medicine. *Front Immunol* **5**, 608 (2014).

75. Banfai, K., Garai, K., Ernszt, D., Pongracz, J. E. & Kvell, K. Transgenic Exosomes for Thymus Regeneration . *Frontiers in Immunology* vol. 10 862 Preprint at https://www.frontiersin.org/article/10.3389/fimmu.2019.00862 (2019).

76. Abreu, S. C., Weiss, D. J. & Rocco, P. R. M. Extracellular vesicles derived from mesenchymal stromal cells: a therapeutic option in respiratory diseases? *Stem Cell Res Ther* **7**, 53 (2016).

77. Chaubey, S. *et al.* Early gestational mesenchymal stem cell secretome attenuates experimental bronchopulmonary dysplasia in part via exosome-associated factor TSG-6. *Stem Cell Res Ther* **9**, 173 (2018).

78. Sánchez-Alonso, S., Alcaraz-Serna, A., Sánchez-Madrid, F. & Alfranca, A. Extracellular Vesicle-Mediated Immune Regulation of Tissue Remodeling and Angiogenesis After Myocardial Infarction . *Frontiers in Immunology* vol. 9 2799 Preprint at https://www.frontiersin.org/article/10.3389/fimmu.2018.02799 (2018).

79. Golub, E. E. Role of matrix vesicles in biomineralization. *Biochimica et Biophysica Acta (BBA)* **1790**, 1592–1598 (2009).

80. Kawecki, T. J. & Ebert, D. Conceptual issues in local adaptation. *Ecol Lett* **7**, 1225–1241 (2004).

81. Iwayama, T. *et al.* Osteoblastic lysosome plays a central role in mineralization. *Sci Adv* **5**, eaax0672 (2019).

82. Greening, D. W., Xu, R., Gopal, S. K., Rai, A. & Simpson, R. J. Proteomic insights into extracellular vesicle biology–defining exosomes and shed microvesicles. *Expert Rev Proteomics* **14**, 69–95 (2017).

83. Logozzi, M. *et al.* High levels of exosomes expressing CD63 and caveolin-1 in plasma of melanoma patients. *PLoS One* **4**, e5219 (2009).

84. Welker, M. W. *et al.* Soluble serum CD81 is elevated in patients with chronic hepatitis c and correlates with alanine aminotransferase serum activity. *PLoS One* **7**, e30796 (2012).

85. Rosenson, R. S. Lipid lowering therapy as an important adjunct to stroke prevention in coronary heart disease patients. *Drugs of Today* **37**, 731–738 (2001).

86. Kalluri, R. & Lebleu, V. S. Discovery of double-stranded genomic DNA in circulating exosomes. *Cold Spring Harb Symp Quant Biol* **81**, 275–280 (2016).

87. Xu, R., Greening, D. W., Rai, A., Ji, H. & Simpson, R. J. Highly-purified exosomes and shed microvesicles isolated from the human colon cancer cell line LIM1863 by sequential centrifugal ultrafiltration are biochemically and functionally distinct. *Methods* **87**, 11–25 (2015).

88. Minciacchi, V. R., Freeman, M. R. & di Vizio, D. Extracellular Vesicles in Cancer: Exosomes, Microvesicles and the Emerging Role of Large Oncosomes. *Semin Cell Dev Biol* **40**, 41–51 (2015).

89. Mariño, G. & Kroemer, G. Mechanisms of apoptotic phosphatidylserine exposure. *Cell Res* **23**, 1247–1248 (2013).

90. Zaborowski, M. P., Balaj, L., Breakefield, X. O. & Lai, C. P. Extracellular Vesicles: Composition, Biological Relevance, and Methods of Study. *Bioscience* **65**, 783–797 (2015).

91. Cai, J., Yang, J. & Jones, D. P. Mitochondrial control of apoptosis: The role of cytochrome c. *Biochim Biophys Acta Bioenerg* **1366**, 139–149 (1998).

92. Crescitelli, R. *et al.* Distinct RNA profiles in subpopulations of extracellular vesicles: Apoptotic bodies, microvesicles and exosomes. *J Extracell Vesicles* **2**, (2013).

93. Jiang, L. *et al.* Determining the contents and cell origins of apoptotic bodies by flow cytometry. *Sci Rep* **7**, 14444 (2017).

94. Cui, L., Houston, D. A., Farquharson, C. & MacRae, V. E. Characterisation of matrix vesicles in skeletal and soft tissue mineralisation. *Bone* **87**, 147–158 (2016).

95. Boonrungsiman, S. *et al.* The role of intracellular calcium phosphate in osteoblast-mediated bone apatite formation. *Proceedings of the National Academy of Sciences* **109**, 14170–14175 (2012).

96. Mahamid, J. *et al.* Mapping amorphous calcium phosphate transformation into crystalline mineral from the cell to the bone in zebrafish fin rays. *Proceedings of the National Academy of Sciences* **107**, 6316–6321 (2010).

97. Davies, O. G. *et al.* Annexin-enriched osteoblast-derived vesicles act as an extracellular site of mineral nucleation within developing stem cell cultures. *Sci Rep* **7**, 12639 (2017).

98. Buzás, E. I., Tóth, E. Á., Sódar, B. W. & Szabó-Taylor, K. É. Molecular interactions at the surface of extracellular vesicles. *Semin Immunopathol* **40**, 453–464 (2018).

99. Lee, S.-Y. & Müller, C. E. Nucleotide pyrophosphatase/phosphodiesterase 1 (NPP1) and its inhibitors. *Medchemcomm* **8**, 823–840 (2017).

100. FLEISCH, H. & NEUMAN, W. [The role of phosphatase and polyphosphates in calcification of collagen]. *Helv Physiol Pharmacol Acta* **19**, C17-8 (1961).

101. Fleisch, H. & Bisaz, S. Mechanism of calcification: inhibitory role of pyrophosphate. *Nature* **195**, 911 (1962).

102. Murshed, M. & McKee, M. D. Molecular determinants of extracellular matrix mineralization in bone and blood vessels. *Curr Opin Nephrol Hypertens* **19**, 359–365 (2010).

103. Liedtke, D., Hofmann, C., Jakob, F., Klopocki, E. & Graser, S. Tissue-nonspecific alkaline phosphatase— a gatekeeper of physiological conditions in health and a modulator of biological environments in disease. *Biomolecules* vol. 10 1–28 Preprint at https://doi.org/10.3390/biom10121648 (2020).

104. Davies, O. G. *et al.* Osteoblast-Derived Vesicle Protein Content Is Temporally Regulated During Osteogenesis: Implications for Regenerative Therapies . *Frontiers in Bioengineering and Biotechnology* vol. 7 92 Preprint at https://www.frontiersin.org/article/10.3389/fbioe.2019.00092 (2019).

105. Depalle, B. *et al.* Osteopontin regulates type I collagen fibril formation in bone tissue. *Acta Biomater* (2020) doi:10.1016/j.actbio.2020.04.040.

106. Jiang, C., Zurick, K., Qin, C. & Bernards, M. T. Probing the influence of SIBLING proteins on collagen-I fibrillogenesis and denaturation. *Connect Tissue Res* **59**, 274–286 (2018).

107. Anderson, H. C. Molecular biology of matrix vesicles. *Clin Orthop Relat Res* 266–280 (1995).

108. Deng, L. *et al.* Osteoblast-derived microvesicles: A novel mechanism for communication between osteoblasts and osteoclasts. *Bone* **79**, 37–42 (2015).

109. Sun, W. *et al.* Osteoclast-derived microRNA-containing exosomes selectively inhibit osteoblast activity. *Cell Discov* **2**, 16015 (2016).

110. Hutcheson, J. D. *et al.* Genesis and growth of extracellular-vesicle-derived microcalcification in atherosclerotic plaques. *Nat Mater* **15**, 335–343 (2016).

111. Strandh, J. & Norlén, H. Distribution per Volume Bone Tissue of Calcium, Phosphorus and Nitrogen from Individuals of Varying Ages as Compared with Distribution per Unit Weight. *Acta Orthop Scand* **35**, 257–263 (1965).

112. National Center for Biotechnology Information. Phosphate. *PubChem Database* https://pubchem.ncbi.nlm.nih.gov/compound/phosphate (2019).

113. Wang, X. *et al.* Hybrid composites of mesenchymal stem cell sheets, hydroxyapatite, and platelet-rich fibrin granules for bone regeneration in a rabbit calvarial critical-size defect model. *Exp Ther Med* **13**, 1891–1899 (2017).

114. Cenni, E. *et al.* Background and rationale of platelet gel in orthopaedic surgery. *Musculoskelet Surg* **94**, 1–8 (2010).

115. Müller, W. E. G., Tolba, E., Schröder, H. C. & Wang, X. Polyphosphate: A Morphogenetically Active Implant Material Serving as Metabolic Fuel for Bone Regeneration. *Macromol Biosci* **15**, 1182–1197 (2015).

116. Ruiz, F. A., Lea, C. R., Oldfield, E. & Docampo, R. Human platelet dense granules contain polyphosphate and are similar to acidocalcisomes of bacteria and unicellular eukaryotes. *J Biol Chem* **279**, 44250–44257 (2004).

117. Oury, C., Toth-Zsamboki, E., Vermylen, J. & Hoylaerts, M. F. The platelet ATP and ADP receptors. *Curr Pharm Des* **12**, 859–875 (2006).

118. Morrissey, J. H. Polyphosphate: a link between platelets, coagulation and inflammation. *Int J Hematol* **95**, 346–352 (2012).

119. Macfarlane, D. E. & Mills, D. C. The effects of ATP on platelets: evidence against the central role of released ADP in primary aggregation. *Blood* **46**, 309–320 (1975).

120. Tauro, B. J. *et al.* Two distinct populations of exosomes are released from LIM1863 colon carcinoma cell-derived organoids. *Mol Cell Proteomics* **12**, 587–598 (2013).

121. Keerthikumar, S. *et al.* Proteogenomic analysis reveals exosomes are more oncogenic than ectosomes. *Oncotarget* **6**, 15375–15396 (2015).

122. Vagner, T. *et al.* Protein Composition Reflects Extracellular Vesicle Heterogeneity. *Proteomics* **19**, e1800167 (2019).

123. Zhang, H. *et al.* Identification of distinct nanoparticles and subsets of extracellular vesicles by asymmetric flow field-flow fractionation. *Nat Cell Biol* **20**, 332–343 (2018).

124. Haraszti, R. A. *et al.* High-resolution proteomic and lipidomic analysis of exosomes and microvesicles from different cell sources. *J Extracell Vesicles* **5**, 32570 (2016).

125. Chen, Q., Takada, R., Noda, C., Kobayashi, S. & Takada, S. Different populations of Wnt-containing vesicles are individually released from polarized epithelial cells. *Sci Rep* **6**, 35562 (2016).

126. Chin, A. R., Yan, W., Cao, M., Liu, X. & Wang, S. E. Polarized Secretion of Extracellular Vesicles by Mammary Epithelia. *J Mammary Gland Biol Neoplasia* **23**, 165–176 (2018).

127. Rocha, S. *et al.* 3D Cellular Architecture Affects MicroRNA and Protein Cargo of Extracellular Vesicles. *Adv Sci (Weinh)* **6**, 1800948 (2019).

128. Thippabhotla, S., Zhong, C. & He, M. 3D cell culture stimulates the secretion of in vivo like extracellular vesicles. *Sci Rep* **9**, 13012 (2019).

129. Tabata, Y. Biomaterial technology for tissue engineering applications. *Journal of the Royal Society Interface* vol. 6 Preprint at https://doi.org/10.1098/rsif.2008.0448.focus (2009).

130. Patel, D. B., Santoro, M., Born, L. J., Fisher, J. P. & Jay, S. M. Towards rationally designed biomanufacturing of therapeutic extracellular vesicles: impact of the bioproduction microenvironment. *Biotechnol Adv* **36**, 2051–2059 (2018).

131. Man, K. *et al.* Development of a Bone-Mimetic 3D Printed Ti6Al4V Scaffold to Enhance Osteoblast-Derived Extracellular Vesicles' Therapeutic Efficacy for Bone Regeneration. *Front Bioeng Biotechnol* **9**, (2021).

132. Azkargorta, M. *et al.* Human Serum Extracellular Vesicle Proteomic Profile Depends on the Enrichment Method Employed. *Int J Mol Sci* **22**, (2021).

133. Shuler, K. T. *et al.* Muscle Stem Cell-Derived Extracellular Vesicles Reverse Hydrogen Peroxide-Induced Mitochondrial Dysfunction in Mouse Myotubes. *Cells* **9**, (2020).

134. Mitchell, R. *et al.* Secretome of adipose-derived mesenchymal stem cells promotes skeletal muscle regeneration through synergistic action of extracellular vesicle cargo and soluble proteins. *Stem Cell Res Ther* **10**, 116 (2019).

135. ThermoFisher Scientific. XRF technology in the field. *ThermoFisher Scientific* 31 (2021).

136. de Jong, W. F. La Substance Minérale Dans les Os. *Recueil des Travaux Chimiques des Pays-Bas* **45**, 445–448 (1926).

137. Lievremont, M., Potus, J. & Guillou, B. Use of alizarin red S for histochemical staining of Ca2+ in the mouse; some parameters of the chemical reaction in vitro. *Acta Anat (Basel)* **114**, 268–280 (1982).

138. Kim, E. *et al.* In vivo multi-parametric manganese-enhanced MRI for detecting amyloid plaques in rodent models of Alzheimer's disease. *Sci Rep* **11**, 12419 (2021).

139. Fu, F., Gao, Z., Gao, L. & Li, D. Effective Adsorption of Anionic Dye, Alizarin Red S, from Aqueous Solutions on Activated Clay Modified by Iron Oxide. *Ind Eng Chem Res* **50**, 9712–9717 (2011).

140. Alizarin Red. https://www.agarscientific.com/alizarin-red.

141. Skrtic, D., Antonucci, J. M. & Eanes, E. D. Amorphous calcium phosphate-based bioactive polymeric composites for mineralized tissue regeneration. *J Res Natl Inst Stand Technol* **108**, 167–182 (2003).

142. BROWN, W. E., SMITH, J. P., LEHR, J. R. & FRAZIER, A. W. Octacalcium Phosphate and Hydroxyapatite: Crystallographic and Chemical Relations between Octacalcium Phosphate and Hydroxyapatite. *Nature* **196**, 1050–1055 (1962).

143. Bannerman, A., Williams, R., C. Cox, S. & Grover, L. *Visualising Phase Change in a Brushite-Based Calcium Phosphate Ceramic*. *Scientific Reports* vol. 6 (2016).

144. Tung, M. S., Chow, L. C. & Brown, W. E. Basic Biological Sciences Hydrolysis of Dicalcium Phosphate Dihydrate in the Presence or Absence of Calcium Fluoride. *J Dent Res* **64**, 2–5 (1985).

145. Perez, L., Shyu, L. J. & Nancollas, G. H. The phase transformation of calcium phosphate dihydrate into octacalcium phosphate in aqueous suspensions. *Colloids and Surfaces* **38**, 295–304 (1989).

146. Temizel, N., Girisken, G. & Tas, A. C. Accelerated transformation of brushite to octacalcium phosphate in new biomineralization media between 36.5°C and 80°C. *Materials Science and Engineering: C* **31**, 1136–1143 (2011).

147. Nelson, D. G. A. & McLean, J. D. High-resolution electron microscopy of octacalcium phosphate and its hydrolysis products. *Calcif Tissue Int* **36**, 219–232 (1984).

148. Ito, N., Kamitakahara, M., Murakami, S., Watanabe, N. & Ioku, K. *Hydrothermal Synthesis and Characterization of Hydroxyapatite from Octacalcium Phosphate*.

149. Simon, P. *et al.* First evidence of octacalcium phosphate@osteocalcin nanocomplex as skeletal bone component directing collagen triple–helix nanofibril mineralization. *Sci Rep* **8**, 13696 (2018).

150. Vyalikh, A., Elschner, C., Schulz, M., Mai, R. & Scheler, U. Early Stages of Biomineral Formation—A Solid-State NMR Investigation of the Mandibles of Minipigs. *Magnetochemistry* **3**, 39 (2017).

151. Kü hlbrandt, W. *et al.* 3D visualization of mitochondrial solid-phase calcium stores in whole cells. doi:10.7554/eLife.29929.001.

152. Orriss, I. R., Key, M. L., Hajjawi, M. O. R. & Arnett, T. R. Extracellular ATP Released by Osteoblasts Is A Key Local Inhibitor of Bone Mineralisation. *PLoS One* **8**, e69057 (2013).

153. Rimai, L., Cole, T., Parsons, J. L., Hickmott, J. T. & Carew, E. B. Studies of Raman Spectra of Water Solutions of Adenosine Tri-, Di-, and Monophosphate and Some Related Compounds. *Biophys J* **9**, 320–329 (1969).

154. RAMAN, C. V & KRISHNAN, K. S. A New Type of Secondary Radiation. *Nature* **121**, 501–502 (1928).

155. Edwards, H. G. M. *Modern Raman Spectroscopy—a Practical Approach.Ewen Smith and Geoffrey Dent. John Wiley and Sons Ltd, Chichester, 2005. Pp. 210. ISBN 0 471 49668 5 (Cloth, Hb); 0 471 49794 0 (Pbk)*. *Journal of Raman Spectroscopy* vol. 36 (2005).

156. Greenbaum, A. *et al.* Bone CLARITY: Clearing, imaging, and computational analysis of osteoprogenitors within intact bone marrow. *Sci Transl Med* **9**, eaah6518 (2017).

157. Cuscó, R. *et al.* Differentiation between hydroxyapatite and β-tricalcium phosphate by means of μ-Raman spectroscopy. *J Eur Ceram Soc* **18**, 1301–1305 (1998).

158. De Aza, P. N. *et al.* Vibrational Properties of Calcium Phosphate Compounds. 1. Raman Spectrum of β-Tricalcium Phosphate. *Chemistry of Materials* **9**, 912–915 (1997).

159. Silveira, L. *et al.* Correlation between near-infrared Raman spectroscopy and the histopathological analysis of atherosclerosis in human coronary arteries. *Lasers Surg Med* **30**, 290–297 (2002).

160. Frost, R. L., Scholz, R., López, A. & Theiss, F. L. Vibrational spectroscopic study of the natural layered double hydroxide manasseite now defined as hydrotalcite-2H-Mg6Al2(OH)16[CO3]·4H2O. *Spectrochim Acta A Mol Biomol Spectrosc* **118**, 187–191 (2014).

161. Nguyen, T. T. *et al.* Characterization of Type I and IV Collagens by Raman Microspectroscopy: Identification of Spectral Markers of the Dermo-Epidermal Junction. *Spectroscopy: An International Journal* **27**, 686183 (2012).

162. Mkukuma, L. D. *et al.* Effect of the proportion of organic material in bone on thermal decomposition of bone mineral: An investigation of a variety of bones from different species using thermogravimetric analysis coupled to mass spectrometry, high-temperature X-ray diffraction,. *Calcif Tissue Int* **75**, 321–328 (2004).

163. Qin, Y., Wang, L., Gao, Z., Chen, G. & Zhang, C. Bone marrow stromal/stem cell-derived extracellular vesicles regulate osteoblast activity and differentiation in vitro and promote bone regeneration in vivo. *Sci Rep* **6**, 21961 (2016).

164. Thery, C. *et al.* Minimal information for studies of extracellular vesicles 2018 (MISEV2018): a position statement of the International Society for Extracellular Vesicles and update of the MISEV2014 guidelines. *J Extracell Vesicles* **7**, 1535750 (2019).

165. Merry, C., Lindahl, U. & Couchman, J. Chapter 17: Proteoglycans and Sulfated Glycosaminoglycans. in *Essentials of Glycobiology* (eds. Varki, A., Cummings, R. & Esko, J.) (Cold Spring Harbor Laboratory Press, Cold Spring Harbor (NY), 2022).

166. Guntur, A. R., Le, P. T., Farber, C. R. & Rosen, C. J. Bioenergetics During Calvarial Osteoblast Differentiation Reflect Strain Differences in Bone Mass. *Endocrinology* **155**, 1589–1595 (2014).

167. Théry, C., Amigorena, S., Raposo, G. & Clayton, A. Isolation and Characterization of Exosomes from Cell Culture Supernatants and Biological Fluids. *Curr Protoc Cell Biol* **30**, (2006).

168. Misra, B. B., Jayapalan, S., Richards, A. K., Helderman, R. C. M. & Rendina-Ruedy, E. Untargeted metabolomics in primary murine bone marrow stromal cells reveals distinct profile throughout osteoblast differentiation. *Metabolomics* **17**, 86 (2021).

169. Penders, J. *et al.* Single Particle Automated Raman Trapping Analysis. *Nat Commun* **9**, 4256 (2018).

170. Ashkin, A., Dziedzic, J. M., Bjorkholm, J. E. & Chu, S. Observation of a single-beam gradient force optical trap for dielectric particles. *Opt Lett* **11**, 288–290 (1986).

171. Williams, C. *et al.* Glycosylation of extracellular vesicles: current knowledge, tools and clinical perspectives. *J Extracell Vesicles* **7**, 1442985 (2018).

172. Movasaghi, Z., Rehman, S. & Rehman, I. U. Raman spectroscopy of biological tissues. *Appl Spectrosc Rev* **42**, 493–541 (2007).

173. Kim, J. H., Kim, S. H. C., Kim, H. K., Akaike, T. & Kim, S. H. C. Synthesis and characterization of hydroxyapatite crystals: A review study on the analytical methods. *J Biomed Mater Res* **62**, 600–612 (2002).

174. Gualerzi, A. *et al.* Raman spectroscopy uncovers biochemical tissue-related features of extracellular vesicles from mesenchymal stromal cells. *Sci Rep* **7**, 9820 (2017).

175. Czamara, K. *et al.* Raman spectroscopy of lipids: A review. *Journal of Raman Spectroscopy* **46**, 4–20 (2015).

176. Pols, M. S. & Klumperman, J. Trafficking and function of the tetraspanin CD63. *Exp Cell Res* **315**, 1584–1592 (2009).

177. Gardiner, C. *et al.* Techniques used for the isolation and characterization of extracellular vesicles: results of a worldwide survey. *J Extracell Vesicles* **5**, 32945 (2016).

178. Nordin, J. Z. *et al.* Ultrafiltration with size-exclusion liquid chromatography for high yield isolation of extracellular vesicles preserving intact biophysical and functional properties. *Nanomedicine* **11**, 879–883 (2015).

179. Tkach, M. & Théry, C. Communication by Extracellular Vesicles: Where We Are and Where We Need to Go. *Cell* **164**, 1226–1232 (2016).

180. Liu, Y. *et al.* Positively charged gold-silver nanostar enabled molecular characterization of cancer associated extracellular vesicles. *Anal Methods* **12**, 5908–5915 (2020).

181. Banbury, C., Rickard, J. J. S., Mahajan, S. & Goldberg Oppenheimer, P. Tuneable Metamaterial-like Platforms for Surface-Enhanced Raman Scattering via Three-Dimensional Block Co-polymer-Based Nanoarchitectures. *ACS Appl Mater Interfaces* **11**, 14437–14444 (2019).

182. Dogan, A. A. & Dufva, M. Customized 3D-printed stackable cell culture inserts tailored with bioactive membranes. *Sci Rep* **12**, 3694 (2022).

183. Lerman, M. J., Lembong, J., Gillen, G. & Fisher, J. P. 3D printing in cell culture systems and medical applications. *Appl Phys Rev* **5**, (2018).

184. Thippabhotla, S., Zhong, C. & He, M. 3D cell culture stimulates the secretion of in vivo like extracellular vesicles. *Sci Rep* **9**, 13012 (2019).

185. Sun, L. *et al.* A 3D culture system improves the yield of MSCs-derived extracellular vesicles and enhances their therapeutic efficacy for heart repair. *Biomedicine & Pharmacotherapy* **161**, 114557 (2023).